UCL Université catholique de Louvain

École polytechnique de Louvain (EPL)

epl

Design, modelling and prototyping of an electrodynamic thrust bearing

Dissertation presented by
Joachim VAN VERDEGHEM

for obtaining the Master's degree in
Electro-mechanical Engineering
Option: Mechatronics

Supervisor
Pr. Bruno DEHEZ

Readers
Pr. Emmanuel DE JAEGER, Dr. Virginie KLUYSKENS

Academic year 2015-2016

ABSTRACT

Magnetic bearings ensure contactless guiding of rotors through electromagnetic forces. In the absence of contact, there is no friction and thus mechanical wear, allowing to increase the lifetime of the bearings as well as largely diminishing the losses and the maintenance costs. Magnetic bearings are thus attractive and even more compelling in very high speed and vacuum applications, compared to conventional solutions such as ball or hydrostatic bearings.

Electrodynamic magnetic bearings (EDBs) are based on forces arising from currents induced by the relative rotation between the permanent magnets and the conducting parts of the bearing. As these bearings do not need a control system, they are simpler, cheaper, more compact, more energy efficient and more reliable than active bearings. Radial EDBs, that ensure the radial guiding of rotors, have already focused much research efforts, allowing to highlight critical issues as their low stiffness, and, above all, their stability properties. By contrast, the interest for the electrodynamic thrust bearings (EDTBs) is much more newer. Contrary to the radial bearings, they present the primary advantage that they are stable in the usual spin speeds range without additional external damping. However, to date, almost all the research efforts are focused on the same thrust bearing topology. As a result, this master's thesis aims at designing, modelling and prototyping a new topology of electrodynamic thrust bearing.

First, a set of new bearing topologies that have not been explored yet is introduced. Following on from this, a global model allowing to predict the axial dynamics as well as the quasi-static behaviour of electrodynamic thrust bearings is derived. It consists in a set of eight parameters and four linear state-space equations, allowing for straightforward stability analyses. Compared to existing models, it requires neither assumptions on the rotor axial kinematics nor solving for the currents. It can be applied to study a wider range of bearings, including those with an arbitrary number of phases and ferromagnetic yokes. Various bearings can thus be objectively compared and it becomes easier to determine the most suitable solution for an application. In particular, this model could be exploited in a process of optimal design of an electrodynamic thrust bearing. The originality of the designing and modelling work has actively encouraged writing an article published in the journal *Transactions on Magnetics* of the IEEE.

Third, the prototype of an eletrodynamic bearing and its test bench are developed. Through experimental measurements, the working principle of the new topology implemented in this prototype has been validated. The prototype being not fully functional, the model could not have been completely validated. However, the critical issues are highlighted and several ways to address them as well as to improve the test bench and the prototype performances are provided. As a result, a further step towards a fully passive magnetic suspension has been passed through this master's thesis.

ACKNOWLEDGMENTS

This master's thesis would not have been possible without the help of many people. Foremost, I would like to express my sincere gratitude to my supervisor, Pr. Bruno Dehez, for his engagement, his strong motivation, his valuable remarks and suggestions and the time that he dedicates to this thesis through the numerous meetings throughout this year. Not all the students have the chance to can rely on such an enthusiastic and wholehearted support from their supervisor. I would also thank him for introducing me to such a compelling subject and for giving me the opportunity to continue this master's thesis as a PhD thesis in the following years.

I am indebted to Corentin Dumont de Chassart for his availability and his great patience in answering to all my questions. I deeply appreciate our numerous discussions that allow me to improve my understanding of magnetic bearings and more generally of electromagnetism but also our less serious conversations.

I am also grateful to Dr. Virginie Kluyskens for her help, useful suggestions to the issues that I encountered and mainly for the attentive readings of the article that follows on from this master's thesis.

I would like to thank all the members of the MCTR/CEREM for their friendly welcome. In particular, I am beholden to Dr. François Baudart for his valuable advices for the conception of the PCB windings. I am also thankful to Axel Jottard for the manufacturing of several parts of the prototype and his availability for the rectifications. I would also like to thank Pr. Emmanuel De Jaeger for being a member of the jury.

Finally, I would like to express my sincere gratitude to my family for their encouragement during the whole of my education and especially to my partner who has supported me throughout the last six years and this master's thesis.

CONTENTS

Introduction **1**

1 State of the art **3**
1.1 Null-flux principle . . . 3
1.2 Thrust bearing topologies . . . 3
1.2.1 Topology 1 (1971) . . . 3
1.2.2 Topology 2 (1996) . . . 5
1.2.3 Topology 3 (2003) . . . 6
1.2.4 Topology 4 (2008) . . . 8

2 Thrust bearing topologies **10**
2.1 Topologies description . . . 10
2.2 Conditions for null-flux topology . . . 12
2.2.1 Series connection . . . 12
2.2.2 Opposition connection . . . 13
2.3 Degenerated topologies . . . 14

3 Model **15**
3.1 Interest . . . 15
3.2 Assumptions . . . 16
3.3 PM flux linkage . . . 16
3.3.1 PM magnetic flux density . . . 16
3.3.2 General form of PM flux linkage . . . 18
3.4 Governing equations . . . 20
3.4.1 Electrical equations . . . 20
3.4.2 Electromechanical equations . . . 21
3.5 Variables elimination . . . 22
3.5.1 Electrical equations . . . 22
3.5.2 Electromechanical equations . . . 23
3.6 State-space model derivation . . . 24
3.6.1 Rotor mechanical model coupling . . . 25
3.6.2 Detent force and torque . . . 25
3.6.3 Phase currents derivation . . . 26
3.6.4 Model parameters determination . . . 26
3.7 Practical case . . . 27
3.7.1 Flux linkage validation . . . 27
3.7.2 Parameters identification . . . 29
3.7.3 Quasi-static analysis . . . 29
3.7.4 Root locus analysis . . . 30
3.7.5 Dynamic analysis . . . 33

4 Experimental validation **34**
4.1 Prototype . . . 34
4.1.1 Topology . . . 34
4.1.2 Rotor . . . 35
4.1.3 Stator . . . 36
4.2 Test bench . . . 47
4.2.1 Air bearings . . . 49
4.2.2 Protective shield . . . 49
4.2.3 Sensors . . . 49
4.2.4 Drive system . . . 50
4.2.5 Loading system . . . 52
4.2.6 Mechanical stops . . . 52
4.3 Model parameters identification . . . 54
4.3.1 Coefficient K_Φ . . . 54
4.3.2 Cyclic inductance L_c . . . 55
4.3.3 Phase resistance R . . . 56
4.4 Model predictions . . . 57
4.4.1 Root locus . . . 57
4.4.2 Quasi-static analysis . . . 58
4.5 Experimental results . . . 60
4.5.1 Assumptions validation . . . 60
4.5.2 Voltages induced in the coils . . . 63
4.5.3 Voltages induced in the phases . . . 65
4.5.4 Dynamic analysis . . . 68
4.5.5 Further improvements . . . 70

Conclusion **73**

Bibliography **75**

A Model: Transformed flux vector **77**

B Root locus: Unstability spin speed **79**

C Back irons: Thickness **81**

D PCB: Radius of connection between the loops **82**

E PCB: Constant track width **83**

F PCB: Assembly **87**

G PCB: Automatic board generation **89**
G.1 Parameters . . . 89
G.2 Script file . . . 89
G.2.1 Global parameters . . . 90
G.2.2 Polygons . . . 90
G.2.3 Vias . . . 90
G.2.4 Screw holes . . . 91
G.2.5 External limits . . . 91
G.2.6 Final commands . . . 91

G.2.7 Example . . . 91

H PCB: Theoritical resistance **94**

I Wire-wound winding **96**
I.1 Type of winding . . . 96
I.2 Lap windings . . . 96
I.2.1 Parallel winding with integral pitch . . . 96
I.2.2 Parallel winding with fractional pitch . . . 98
I.3 Support . . . 99
I.3.1 Version A . . . 99
I.3.2 Version B . . . 100
I.4 Windings fabrication . . . 101

J Turbine: Maximal spin speed **103**

K Dynamics: Springs in parallel **105**
K.1 Open circuit . . . 105
K.2 Short-circuited . . . 106

L Prototype: Drawings **107**
L.1 Yoke . . . 108
L.2 First back iron . . . 109
L.3 Second back iron . . . 110
L.4 Lids . . . 111
L.5 Protective shield . . . 112
L.6 Sleeve . . . 113
L.7 Tube . . . 114
L.8 Mounting bracket . . . 115

LIST OF SYMBOLS

α	Rotor angular position with respect to the stator	[rad]
β_j	Angular position of the j-th pole of a phase winding	[rad]
δ_k	Angular position of the k-th phase winding	[rad]
$\Delta\theta_a$	Angular shift between each part of the armature subassembly	[rad]
$\Delta\theta_{PM}$	Angular shift between each part of the PMs arrangements subassembly	[rad]
ϵ	Rotor radial displacement from its nominal position	[m]
γ_l	Angular position of the l-th loop of a phase winding	[rad]
Λ	Angle between the rotor spin axis and the horizontal support of the test bench	[rad]
μ_r	Relative magnetic permeability of the ferromagnetic parts	[−]
ρ_c	Electrical resistivity of copper	[Ωm]
ϕ	Whirl angle	[rad]
Φ_k	Magnetic flux linked by the k-th phase winding due to the PMs	
Ψ_k	Total magnetic flux linked by the k-th phase winding	
$\omega = \dot{\alpha}$	Rotor spin speed with respect to the stator	[rad/s]
ω_u	Unstability rotor spin speed	[rad/s]
$\mathbf{A}$	State-space representation	[−]
$\mathbf{A}'$	State-space representation comprising the detent efforts	[−]
B	Axial magnetic flux density	[T]
C	Damping factor	[Ns/m]
$f(Z)$	Axial magnetic field dependence	[−]
F	Axial electrodynamic force	[N]
F'	Axial electromagnetic (electrodynamic and detent) force	[N]
F_e	Axial external force	[N]
$g(r)$	Radial magnetic field dependence	[−]
K_Φ	Flux coefficient	[Wb/m]
K_c	Axial stiffness due to the Eddy currents	[N/m]
K_d	Detent stiffness	[N/m]
K_f	Axial stiffness	[N/m]
K_s	Mechanical coupling stiffness	[N/m]
K_t	Torque coefficient	[Nm/m^2]
L_c	Cyclic inductance	[H]
L_{ii}	Self inductance of the i-th phase winding	[H]

L_{ij}	Mutual inductance between the i-th and j-th phase windings	[H]
M	Rotor mass	[kg]
N	Number of phases	[−]
N_l	Number of loops per phase in one layer of the PCB	[−]
$N_{l,t}$	Total number of loops per phase (including the different layers of the PCB)	[−]
p	Pole pairs number of the rotor and stator	[−]
R	Phase resistance	[Ω]
T	Axial electrodynamic torque	[Nm]
w	Width of wires for the wire-wound winding	[m]
z	Rotor axial displacement from its nominal position	[m]

$\{r, \theta, Z\}$	Cylindrical frame attached to the PMs arrangements
$\{\xi, \psi, a\}$	Cylindrical frame attached to the armature

INTRODUCTION

In the next decades, meeting the increasing world demand in energy will represent one of the fundamental issues. To this end, much research efforts have been focused on the renewable energy sources, such as wind, solar or biofuels. However, tackling this problem cannot only go through a growth in energy production. In this context, the energy efficiency of all the systems that are used daily becomes a major concern. Among these systems, rotating machineries suffer from several losses and especially in the components ensuring the guiding and the support of the moving parts with respect to the stationary parts, namely the bearings. There exists many sorts of bearings among which the mechanical, journal, hydrostatic or magnetic ones can be cited.

Magnetic bearings ensure contactless guiding of rotors through electromagnetic forces. In the absence of contact, there is no friction and thus mechanical wear, allowing to increase the lifetime of the bearings as well as largely diminishing the losses and the maintenance costs. Compared to classical bearings, such as ball ones, the only limit for the speed of magnetic bearings comes from the strength of the material of the rotor. Besides, they become essential in some applications where lubrification and contaminants are not allowed, such as in vacuum, clean rooms or medical devices. They can also be used in challenging conditions such as high temperature or applications where no dust can appear. These advantages explain the high motivation to develop and study magnetic bearings in the past years. Magnetic bearings can be classified into two categories: the active ones (AMB) and the passive ones (PMB).

Today, the AMBs represent the vast majority of magnetic bearings that are implemented in industrial applications. They are based on a ferromagnetic rotor which is attracted by electromagnets whose current is controlled to maintain the levitated object in a wanted position. The control also allows to achieve required stiffness and damping. AMBs are thus able to influence the rotor dynamics and to offer high stiffness and power densities [1]. Besides, they can be used to stabilise any degree of freedom, even all of these. However, the AMBs also suffer from several drawbacks. Indeed, the need for a control system increases the cost, the dimensions of the device but also the complexity of their implementation, as it requires electronic components and sensors [2]. Besides, as they are active, the AMBs necessitate an external power supply, which is not available in all applications.

By contrast, PMBs only rely on passive phenomena, leading to lower costs and a higher reliability. Among these bearings, the ones based on permanent magnets present a reasonable stiffness and high power efficiency [3] [4]. However, as stated in Earnshaw's theorem, it is not possible to fully levitate an object using only permanent magnets (PMs) or electromagnets supplied with DC current [5]. Therefore, at least one degree of freedom has to be stabilised with another type of bearings. Electrodynamic bearings also belong to the PMBs. They are based on the relative motion of conductors with respect to the magnetic field produced by PMs or electromagnets supplied with DC current. Hence, the flux linked

by the conductors varies over time and, as the conductors are short-circuited, a current is induced so as to generate restoring forces.

Electrodynamic bearings can be separated into two groups: the radial bearings, whose aim is to ensure the radial guiding of the moving part, and the thrust bearings, whose aim is to ensure the axial guiding of the moving part. The former have been the subject of researches for many years [6]-[9]. Critical issues, such as their low stiffness and, above all, their stability properties, have been highlighted. Without a sufficient addition of external damping, these bearings cannot be stable. To address these issues and to study their dynamic behaviour, several models have been derived in the past years [10]-[13]. The final aim is to integrate them in a complete and passive suspension. To date, there exists only one functional prototype whose performances are fairly limited [14].

By contrast, the interest for the electrodynamic thrust bearings (EDTBs) is much more newer. Contrary to the radial bearings, they present the primary advantage that they are stable in the usual spin speeds range without additional external damping [15]. Hence, these bearings can be completed with radial permanent magnets bearings in order to obtain a fully passive suspension [15] [16]. However, to date, almost all the research efforts are focused on the same thrust bearing topology that was proposed in [17].

As a result, this master's thesis aims at designing, modelling and prototyping a new topology of electrodynamic thrust bearing. It is structured as follows. In a first chapter, the null-flux principle is described. Then, a review of the technical and scientific literature allows to depict the current state of the art of the electrodynamic thrust bearing topologies.

Following on from this, the second chapter exposes a set of new thrust bearing topologies that have not been explored yet. These topologies being parametrised through two angles and one length, conditions on these latter are derived so as to ensure that each bearing topology satisfies the null-flux principle.

The third chapter is devoted to deriving a global model which allows to predict the axial dynamics as well as the quasi-static behaviour of electrodynamic thrust bearings. In a first part, the interest of the proposed model compared with existing ones is explained. Then, the assumptions made to derive the model are summarised. Following on from this, the analytical expression of the flux due to the permanent magnets and linked by the armature winding is developed. A linear state-space model is later derived and finally applied to a practical case.

The last chapter is dedicated to the experimental results. It intends to validate and benefit from the model derived in the third chapter through the prototyping of an electrodynamic thrust bearing. The prototype is based on one of the new topologies presented in the second chapter. In a first part, the thrust bearing and its test bench are described. After the identification of the parameters, taking advantage of the model, the dynamics as well as the quasi-static behaviour of the bearing are analysed. Experimental measurements performed on the prototype are later compared to the theory and model predictions. Finally, several ways to improve the behaviour of the prototype are provided.

CHAPTER 1

STATE OF THE ART

1.1 Null-flux principle

Among the different existing topologies of electrodynamic bearing, either the radial or the thrust ones, much research efforts have been focused on those which respect the null-flux principle. This principle was first introduced by J. Powell and G. Danby in the context of a ground vehicle and, later, it has been applied to rotating machineries [18]. As its name implies, it means that the flux linked by the winding is equal to zero when the levitated object is in its equilibrium position. Hence, there is no voltage induced in the coils and therefore no unnecessary currents and forces appear. It allows to reduce the Joule losses and to achieve higher energy efficiency [19]. By contrast, when this object is subjected to an excursion from its nominal position, the winding perceives a varying magnetic flux inducing a current which interacts with the magnetic field to produce a force. This current tends to oppose to the variations in the magnetic flux and, through the force, brings the rotor back in its equilibrium position. This principle can be implemented by introducing symmetry in the topologies, as shown hereinafter.

1.2 Thrust bearing topologies

This sections yields a review of the technical and scientific literature allowing to depict the current state of the art of the electrodynamic thrust bearing topologies. As these topologies are based on electrodynamic phenomena, they cannot exert any axial effort when the rotor is not in relative motion with respect to the stator. They thus require a thrust system that works at zero spin speed.

1.2.1 Topology 1 (1971)

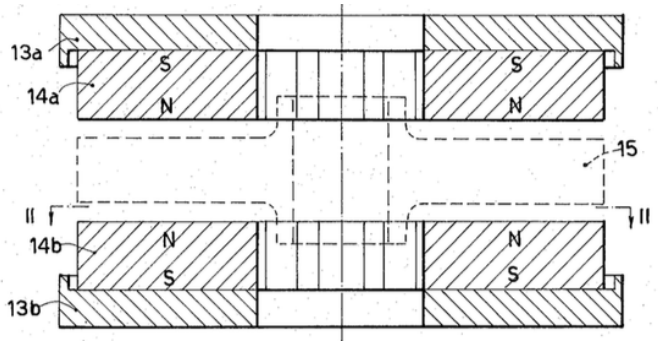

Fig. 1.1: Cross-sectional view of the first device proposed in [20].

The two first electrodynamic thrust bearing topologies that are studied here has been proposed by G. Sacerdoti, A. Catitti, and L. L. Soglia, in [20]. As shown in Fig. 1.1,

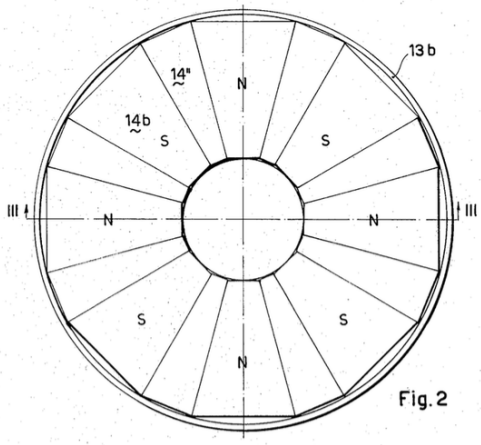

Fig. 1.2: Upside view of the PMs arrangements of the first device proposed in [20].

the first axial bearing is composed of two ferromagnetic yokes (13a) and (13b) on which permanent magnets arrangements (14a) and (14b) are respectively attached. These two PMs arrangements are identical and placed in a repulsive mode on the stator. As shown in Fig. 1.2, these permanent magnets present a trapezoidal shape and are in even number. Besides, they are polarised axially and consecutive PMs are oriented with opposed polarity. Finally, they are evenly distributed around the revolution axis of the system and placed in a starlike pattern. Between them, trapezoidal non-magnetic parts are placed. As regards the rotor, it receives a conductive disc (15) which is placed between both permanent magnets arrangements. This axial bearing is implemented in a complete passive suspension where the radial levitation is ensured by classical permament magnets bearings.

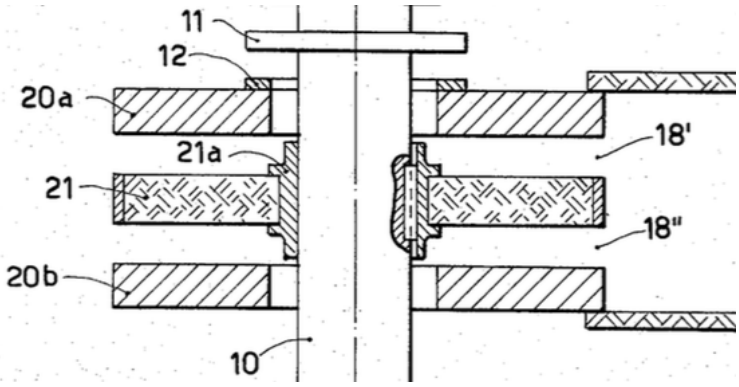

Fig. 1.3: Cross-sectional view of the second device proposed in [20].

The second axial bearing that was proposed is shown in Fig. 1.3. Compared with the first version, the PMs arrangements as well as the conductive disc are swapped. Hence, in this version, there are two conductive rings (20a) and (20b) attached to the stator and one starlike pattern of permanent magnets (21) fixed to the rotor.

The operation principle of both versions are identical. Let us then take the first version as reference. When the rotor spins, there is a relative motion between the magnetic field due to the PMs and the conductive disc, leading to the appearance in the disc of induced currents. The interaction between these currents and the PMs magnetic field results in

repulsive forces on both sides. These forces being highly dependent on the airgap between the PMs and the disc, the rotor is brought in its nominal position where the forces equalise.

1.2.2 Topology 2 (1996)

R. F. Post proposed a new topology of electrodynamic thrust bearing in [17]. As shown in Fig. 1.4, it is composed of two Halbach arrays attached to the rotor. These arrays consists in permanent magnets with a trapezoidal shape. They are placed in front of each other in repulsive mode so that the magnetic flux density at the middle of them is null, allowing to respect the null-flux principle. A planar conductor array is located between these PMs arrays and attached to the stator. It is constituted of several short-circuited coils that can comprise an inductive load. This bearing is anew implemented in a complete passive levitation. The radial one is ensured through classical PMs bearings. Besides, PMs axial bearing is also used to compensate the weight, meaning that the electrodynamic thrust bearing only aims at stabilising the axial degree of freedom and not sustaining the complete rotor.

When the rotor is in its nominal position, the coils constituting the circuit array experience no varying flux as the magnetic field produced by each PMs arrays compensate. By contrast, when the rotor leaves this position, the magnetic flux density linked by the windings is no more null and will vary with the axial position. These coils being short-circuited, a current is induced in each winding. The interaction between theses currents in the radial sections and the PMs magnetic field results in a restoring force, as stated by Lorentz force law.

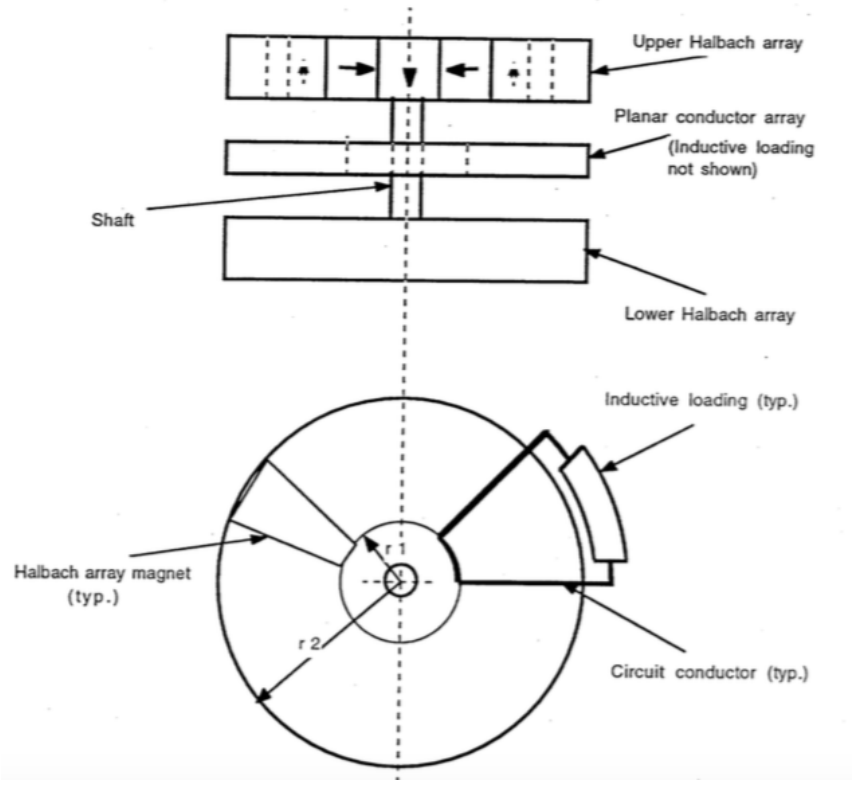

Fig. 1.4: Lateral and upside views of the device proposed in [17].

This topology has been further studied in the past few years, leading to the development of models allowing to analyse its dynamic and quasi-static behaviours. These models are derived for the specific topology presented in Fig. 1.5, which is composed of a two-phased winding located in the middle of either two Halbach arrays or two more classical arrangements with PMs polarised axially. This topology was successfully implemented and tested in a completely passive suspension [15]-[16].

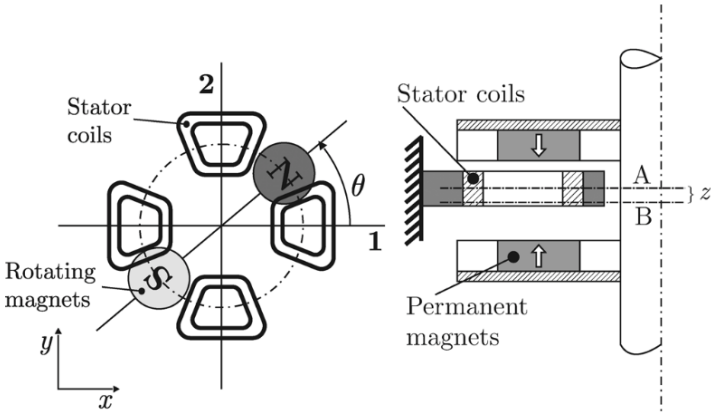

Fig. 1.5: Upside and cross-sectional views of the device proposed in [15].

1.2.3 Topology 3 (2003)

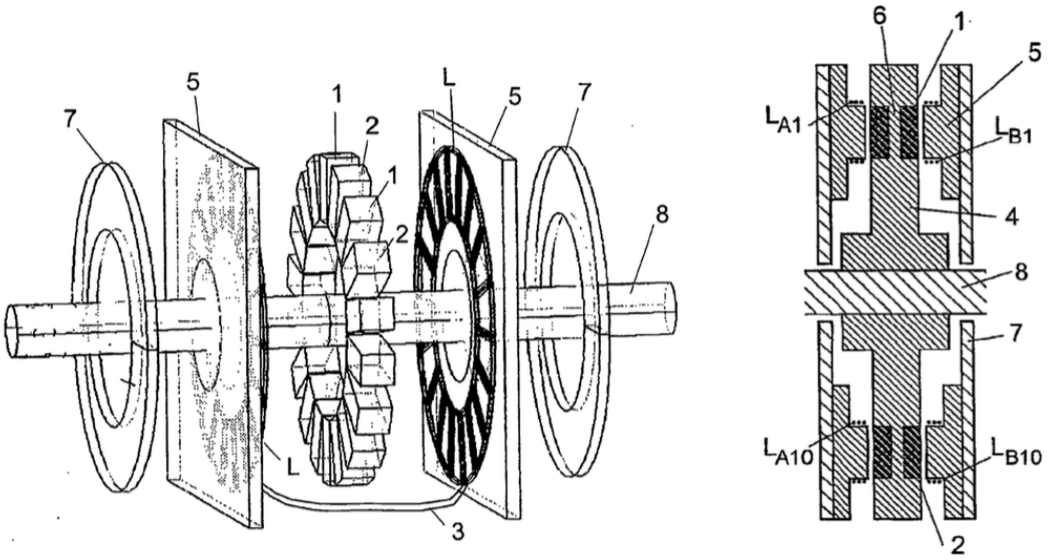

(a) Overview. (b) Cross-sectional.

Fig. 1.6: Overview and cross-sectional view of the device proposed in [21]

The third bearing topology that is analysed has been proposed by H. K. Asper in [21]. Fig. 1.6a shows an overview of this device. This EDTB is constituted of two assemblies, namely the coils and the permanent magnets, that are in relative motion each with respect to the other. Both of them can be attached either to the stator or the rotor (8). The first assembly, namely the permanent magnets arrangement (1)-(2), is squeezed between

both parts (5) constituting the second assembly, namely the coils. Again, the permanent magnets present an axial polarisation and two consecutive PMs are oriented with opposed polarity. Fig. 1.6b shows a cross-sectional view of an example of the bearing. The coils are wound on coil holders (5) which are fixed to a soft iron (7). The PMs are divided into two parts and placed on both sides in a non-magnetic material (6). They can have various shape as cuboid or prism. Besides, they present the same size as the coils.

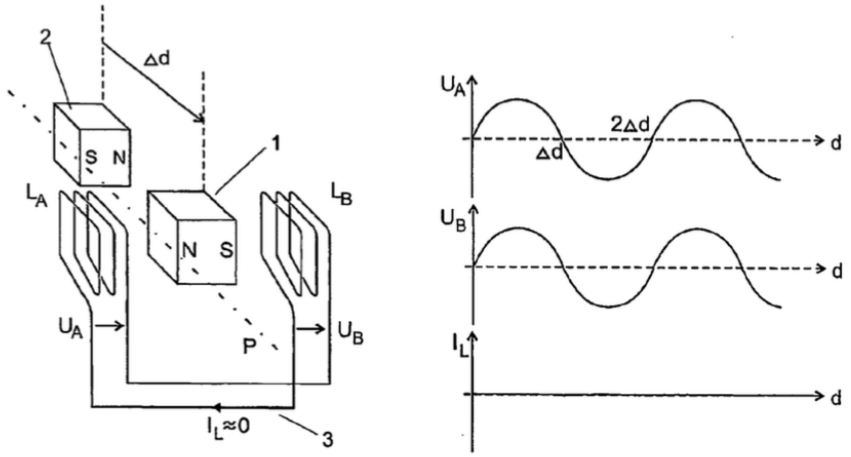

Fig. 1.7: Operation principle: in nominal position, from [21].

Fig. 1.7 shows the operation principle of this bearing when the rotor is in its nominal position. Both coils L_A and L_B constituting the complete winding link the flux due to the permanent magnets magnetic field. As the PMs are in the center, these fluxes are exactly equal and so are the induced voltages U_A and U_B. To ensure the null-flux principle, these coils are thus connected so that both fluxes and thus the induced voltages cancel each other. As a result, the current I_L flowing through the coils is zero. The method that is used to connect both coils will be named opposition connection hereinafter.

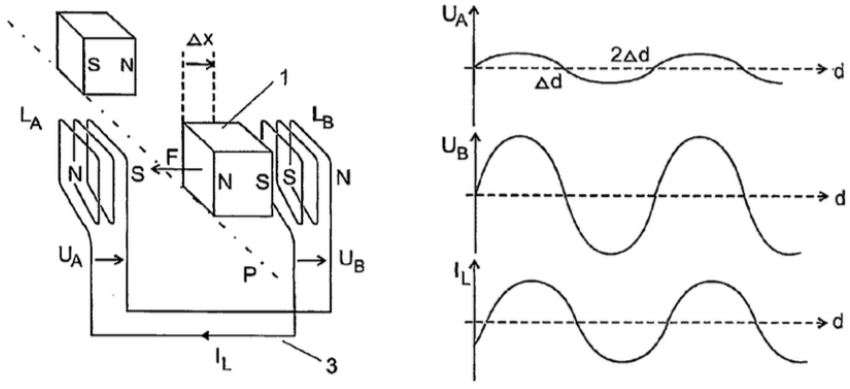

Fig. 1.8: Operation principle: outside the nominal position, from [21].

By contrast, when the rotor is no more in its nominal position, the voltage induced in both coils become different. As shown in Fig. 1.8, the permanent magnets being closer to the coil L_B than to the coil L_A, the former links a larger flux than the latter, which leads

to a higher amplitude of the voltage induced U_B compared with U_A. Then, keeping the opposition connection of these coils to ensure the null-flux principle, the resulting induced voltage in the complete electrical circuit is non-zero. Therefore, a current I_L flows through the coils and interacts with the magnetic flux density produced by the permanent magnets to generate a restoring force.

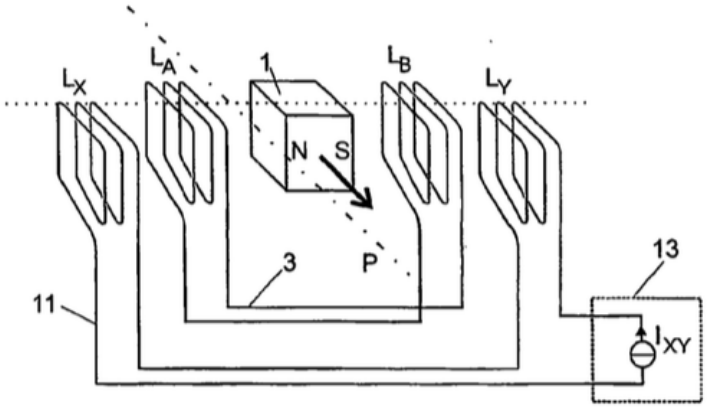

Fig. 1.9: Operation principle: drive system [21].

The patent also proposes a way to drive the complete system. The permanent magnets of the bearing are also used for this drive system, as shown in Fig. 1.9. However, new coils are added, surrounding these of the EDTB. These coils are placed such that they are shifted by a quarter period compared with the bearing ones. Besides, both parts constituting the complete winding are connected in another way, named series connexion hereinafter, leading to a non-zero flux in nominal position. This is essential to ensure the driving of the system even in this position.

1.2.4 Topology 4 (2008)

The fourth bearing topology has been proposed by J. Sandtner and H. Bleuler in [22]. As shown in Fig. 1.10, the rotor is constituted of two permanent magnets arrangements. In each of them, the polarisation of the PMs is radial and two consecutive PMs are oriented in opposition although an Halbach array could also be possible. There exists an angular shift between both PMs arrangements so that one is maximal when the other is minimal. They can be either placed on a cylindrical mandrel or in a back iron, as in the figure, depending whether the magnetic field has to radiate outwards or inwards. The stator comprises what the authors call a "distributed winding". Indeed, the winding is composed of numerous axial segments that are placed so as to form a ring. This shape is repeated on several radial layers and the segments are connected at their ends in order to build rectangular loops. This construction offers the main advantage to fill all the available space.

The flux linked by each loop is the sum of the fluxes due the both PMs arrangements. When the rotor is in its nominal position, the fluxes linked by the loops due to each PMs arrangements are equal and opposed meaning that the total flux is null. Therefore, there is no induced current and thus losses, meaning that the null-flux principle is also respected in this topology.

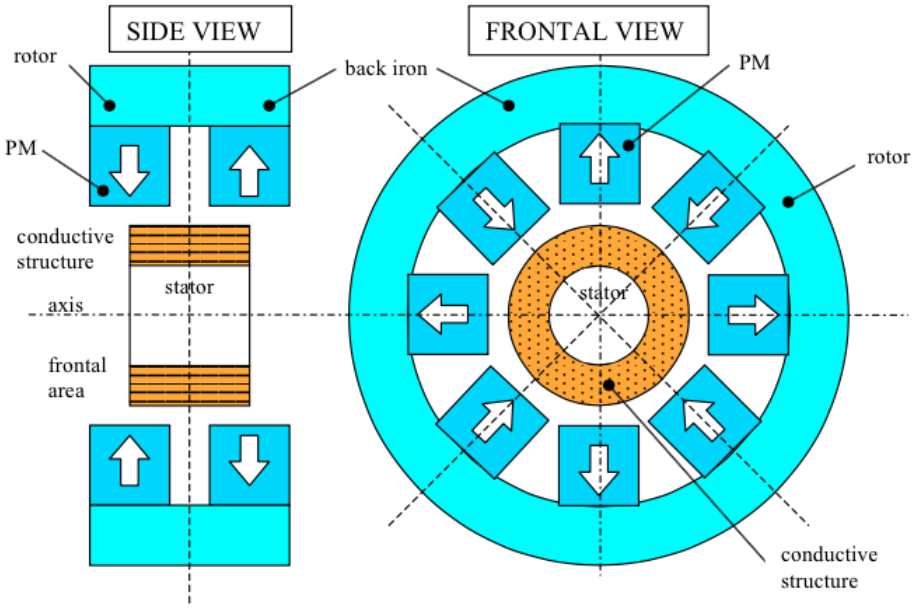

Fig. 1.10: Side and frontal view of the device proposed in [22].

By contrast, when the rotor departs from its nominal position, the fluxes linked by the loops due to both PMs arrangements are no more identical. Indeed, the surface of the loops that are in front of one PMs arrangement increases while the surface in front of the other decreases. Therefore, there exists an unbalance in the flux linked, yielding an induced current. This generates a restoring force by interaction with the PMs magnetic field. The height of the conductive part has to be smaller than the total axial length of the permanent magnets to ensure variations in the flux that is linked by the loops. Besides, the ends of the structure have to remain in a zone where the magnetic flux density presents a radial component given that this latter produces the axial restoring force by interacting with the current flowing in the loops. The winding being distributed, the restoring force is not pulsated.

Compared with previous topologies, this one works in a completely different way: here, the flux variations come from a change in the surface that links the magnetic field of each PMs arrangements while in the previous topologies, the flux variation results from a change in the magnetic field strength with the distance.

CHAPTER 2

THRUST BEARING TOPOLOGIES

On the basis of the state of the art, this chapter first exposes a set of new thrust bearing topologies that have not been explored yet. Then, these bearing topologies being parametrised through two angles and one length, conditions on these latter are derived so as to ensure that each topology satisfies the null-flux principle. Following on from this, degenerated topologies are described.

2.1 Topologies description

The new bearing topologies are constituted of two subassemblies rotating relative to each other. The first subassembly comprises two identical arrangements of permanent magnets producing, each of them, an axial magnetic field having p pole pairs. The second assembly is basically made of two coils having also p pole pairs, each predominantly magnetically linked to one permanent magnet arrangement. The two coils are connected either in series, as represented in Fig. 2.1a, or in opposition, as represented in Fig. 2.1b, so as to form a phase winding which is short-circuited.

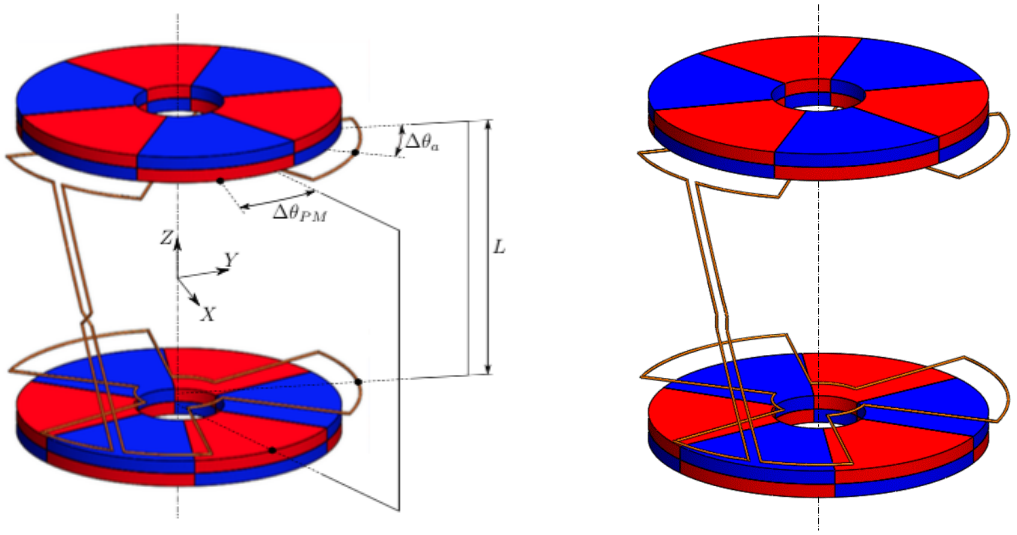

(a) Series connection of a phase winding.

(b) Opposition connection of a phase winding.

Fig. 2.1: Bearing topologies with external PMs.

In the bearing topologies presented in Figs. 2.1a and 2.1b, the permanent magnet arrangements are outside the armature winding, but they could be inside, as shown in Figs. 2.2a and 2.2b. In addition, these arrangements can be of different types, with surface-mounted, burried or inset permanent magnets, on the one hand, or respecting an Halbach array configuration, on the other hand. Permanent magnets could also be replaced by

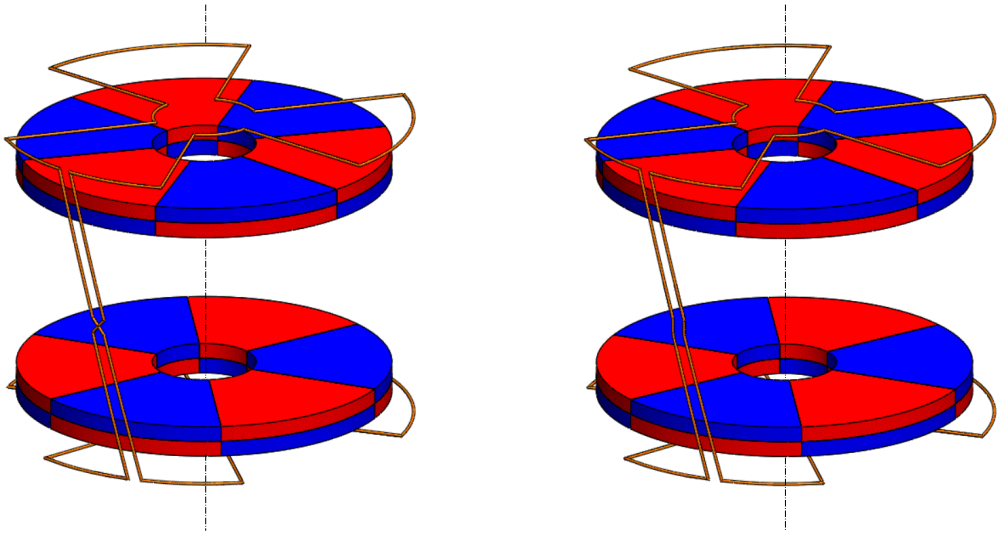

(a) Series connection of a phase winding.

(b) Opposition connection of a phase winding.

Fig. 2.2: Bearing topologies with internal PMs.

electromagnets supplied with DC currents. The angular shift between the upper and lower PMs arrangements is denoted $\Delta\theta_{PM}$.

In order to obtain a higher restoring force, but also a force independent of the angular position of the rotating subassembly, the phase winding should be duplicated N times and evenly distributed so as to form a N-phased symmetrical armature winding, the position of the k-th phase being given by:

$$\delta_k = \frac{2\pi(k-1)}{pN} + \delta_0, \tag{2.1}$$

where $k = \{1, \ldots, N\}$ and δ_0 is the first phase winding angular position. Those windings may have various geometries but are identical. Moreover, they can be placed in air, as represented, but also behind a ferromagnetic yoke or in a slotted ferromagnetic circuit. The angular shift between the upper and lower coils is denoted $\Delta\theta_a$.

Conditions on the angles $\Delta\theta_{PM}$ and $\Delta\theta_a$ are derived in the next section, depending whether the coils are connected in series or in opposition, so as to ensure that the flux linked by the armature winding is null when it is centered along the Z axis with regard to the permanent magnet arrangements, respecting thus the null-flux principle. In this way, there are no induced currents, and therefore no Joule losses in the windings as long as the rotating part is centered. By contrast, when shifted, currents are induced in the armature winding, the latter producing, by interaction with the magnetic field of the permanent magnets, an axial recentering force. The working principle of these new topologies is globally identical to that of the topology described in section 1.2.3.

Finally, for some of the conditions derived hereinafter on the angular shifts $\Delta\theta_{PM}$ and $\Delta\theta_a$, the distance L between both parts of the internal subassembly can be reduced to zero. When the internal subassembly is the armature winding, the latter reduces to one single short-circuited coil, as shown in Fig. 2.3a. This degenerated topology corresponds to

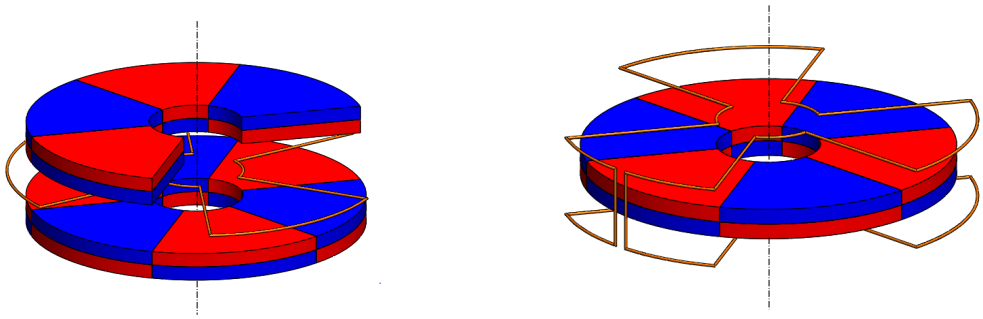

(a) External PMs and a phase winding.

(b) Single PMs arrangement and an opposition connection of a phase winding.

Fig. 2.3: Degenerated bearing topologies.

that proposed in [23]. Conversely, when the internal subassembly is the permanent magnet arrangements, these simply reduce to one, as shown in Fig. 2.3b.

2.2 Conditions for null-flux topology

The purpose of this section is to derive the conditions on $\Delta\theta_{PM}$ and $\Delta\theta_a$, depending on the series or opposition connection of the coils, that ensures that the flux linked by the armature winding is null when the rotor is centered along the Z axis with regard to the PMs arrangements. Hereinafter, the fluxes are considered to be positive when directed along the positive Z axis. Regardless of the topology and considering only the fundamental of the magnetic flux density, the flux linked by the upper coil in the nominal position (i.e. zero axial and radial displacements) is:

$$\Phi^U = \Phi^U_{PM,U}\cos(p\alpha) + \Phi^U_{PM,L}\cos(p(\alpha - \Delta\theta_{PM})), \tag{2.2}$$

where $\Phi^U_{PM,U}$ and $\Phi^U_{PM,L}$ are the amplitude of the flux linked by the upper coil due to the upper and lower PMs arrangements respectively when the EDB is in its nominal position, p is the number of pole pairs and α is the rotor angular position with respect to the stator. Similarly, the flux linked by the lower coil in the nominal position is:

$$\Phi^L = -\Phi^L_{PM,L}\cos(p(\alpha + \Delta\theta_a - \Delta\theta_{PM})) - \Phi^L_{PM,U}\cos(p(\alpha + \Delta\theta_a)), \tag{2.3}$$

where $\Phi^L_{PM,U}$ and $\Phi^L_{PM,L}$ are the amplitude of the flux linked by the lower coil due to the upper and lower PMs arrangements respectively when the EDB is in its nominal position. Moreover, the symmetry of the system leads to:

$$\begin{aligned} \Phi^U_{PM,U} &= \Phi^L_{PM,L} \\ \Phi^L_{PM,U} &= \Phi^U_{PM,L}. \end{aligned} \tag{2.4}$$

2.2.1 Series connection

Let us consider the topologies with a series connection, as illustrated in Fig. 2.1a. In this case, the total flux Φ_{tot} linked by a phase winding yields:

$$\Phi_{tot} = \Phi^U + \Phi^L. \tag{2.5}$$

Substituting (2.2), (2.3) and (2.4) into (2.5) leads to:

$$\begin{aligned}\Phi_{tot} &= \Phi^U_{PM,U}\left[\cos(p\alpha) - \cos(p(\alpha + \Delta\theta_a - \Delta\theta_{PM}))\right] \\ &\quad + \Phi^U_{PM,L}\left[\cos(p(\alpha - \Delta\theta_{PM})) - \cos(p(\alpha + \Delta\theta_a))\right] \\ &= -2\Phi^U_{PM,U}\sin\left(p\alpha + p\,\frac{\Delta\theta_a - \Delta\theta_{PM}}{2}\right) \\ &\qquad \times \sin\left(p\,\frac{\Delta\theta_{PM} - \Delta\theta_a}{2}\right) \\ &\quad + 2\Phi^U_{PM,L}\sin\left(p\alpha + p\,\frac{\Delta\theta_a - \Delta\theta_{PM}}{2}\right) \\ &\qquad \times \sin\left(p\,\frac{\Delta\theta_{PM} + \Delta\theta_a}{2}\right). \end{aligned} \tag{2.6}$$

This expression reduces to zero for all rotor angular position if the second sine of each term cancels. For the first term, it yields:

$$\Delta\theta_{PM} = \Delta\theta_a. \tag{2.7}$$

Using (2.7), the second term gives:

$$\Delta\theta_a = \frac{k\pi}{p}, \tag{2.8}$$

where $k \in \mathbb{Z}$. It should be noticed that this second condition vanishes if $\Phi^U_{PM,L}$ equals to zero, i.e. when there is a magnetic insulation between the upper PMs and the lower coil and vice versa. Magnetic insulation may, for example, come from a magnetic circuit with high permeability.

2.2.2 Opposition connection

Let us now consider the topologies with an opposition connection, as illustrated in Fig. 2.1b. The total flux Φ_{tot} linked by a phase winding gives:

$$\Phi_{tot} = \Phi^U - \Phi^L. \tag{2.9}$$

Substituting (2.2), (2.3) and (2.4) into (2.9) leads to:

$$\begin{aligned}\Phi_{tot} &= \Phi^U_{PM,U}\left[\cos(p\alpha) + \cos(p(\alpha + \Delta\theta_a - \Delta\theta_{PM}))\right] \\ &\quad + \Phi^U_{PM,L}\left[\cos(p(\alpha - \Delta\theta_{PM})) + \cos(p(\alpha + \Delta\theta_a))\right] \\ &= 2\Phi^U_{PM,U}\cos\left(p\alpha + p\,\frac{\Delta\theta_a - \Delta\theta_{PM}}{2}\right) \\ &\qquad \times \cos\left(p\,\frac{\Delta\theta_{PM} - \Delta\theta_a}{2}\right) \\ &\quad + 2\Phi^U_{PM,L}\cos\left(p\alpha + p\,\frac{\Delta\theta_a - \Delta\theta_{PM}}{2}\right) \\ &\qquad \times \cos\left(p\,\frac{\Delta\theta_{PM} + \Delta\theta_a}{2}\right). \end{aligned} \tag{2.10}$$

This expression reduces to zero for all rotor angular position if the second cosine of each term cancels. For the first term, it yields:

$$\Delta\theta_{PM} = \Delta\theta_a + \frac{\pi}{p}, \tag{2.11}$$

Using (2.11), the second term leads to:

$$\Delta\theta_a = \frac{k\pi}{p}, \tag{2.12}$$

where $k \in \mathbb{Z}$. Again, this second condition vanishes when there is a magnetic insulation between the upper PMs and the lower coil and vice versa.

2.3 Degenerated topologies

As explained in section 2.1, the distance L between both parts of the internal subassembly of the EDB can be reduced to zero, yielding degenerated topologies.

Let us first analyse the topologies with the armature winding as internal subassembly. Considering the situation with a series connection, the condition (2.8) imposes $\Delta\theta_a$ to be equal to 0 or π/p. In the former case, the phase windings reduce to single short-circuited windings and the condition (2.7) leads to $\Delta\theta_{PM} = 0$. This degenerated topology is shown in Fig. 2.3a and corresponds to the one proposed by R. F. Post in [17]. In the latter case, the winding reduces to a single short-circuited winding which links the magnetic field of all poles. Hence, even when the rotor is not in its nominal position, there are no flux variations and then no induced currents in the windings, leading to a nonfunctional bearing.

Considering now the situation with an opposition connection, the condition (2.12) also imposes $\Delta\theta_a$ to be equal to π/p or 0. In the former case, the flux linkage of both coils add and the condition (2.11) results in $\Delta\theta_{PM} = 0$. In the latter case, the flux linked by both coils compensate even when the rotor is not in its nominal position, leading to a nonfunctional bearing. Thus, a degenerated topology with the armature winding as internal subassembly has to satisfy $\Delta\theta_{PM} = 0$.

Let us then analyse the topologies with the PMs arrangements as internal assembly. From the conditions derived above, the angular shift $\Delta\theta_{PM}$ must be equal to π/p or 0. In the first case, the PMs arrangements simply reduce to one. Based on (2.7) and (2.11), the angular shift $\Delta\theta_a$ is equal to π/p or 0 respectively, depending on the series or opposition connection. Fig. 2.3b shows this latter topology. It corresponds to the topology proposed by H. K. Asper in [21]. In the second case, the magnetic fields of both PMs arrangements always compensate, resulting in a nonfunctional bearing.

CHAPTER 3

MODEL

This chapter purpose is to derive a model allowing to predict the axial dynamics as well as the quasi-static behaviour of electrodynamic thrust bearings. It is structured as follows. First, the interest of the proposed model compared with existing ones is explained. Then, the assumptions made to derive the model are summarised. Following on from this, the analytical expression of the PM flux linked by the armature winding is developed. The state-space model is later derived and finally applied to a practical case.

3.1 Interest

Initially, the development of electrodynamic thrust bearings and their integration into passive magnetic suspensions have followed a rather experimental approach [16]. Along with these experiments came up models for studying their stiffness and stability properties. However, the scopes of these models are still narrowed by restrictive assumptions. In a first model, the phase currents and the total force on the bearing rotor are obtained by neglecting the effects of the rotor axial speed on the induced forces [6]. However, assuming these quasi-static conditions precludes predicting the stability of a bearing operating in dynamic conditions. A second model requires a numerical integration of Faraday's current law and of the rotor equation of motion to calculate the Lorentz forces on the rotor [23]. Nevertheless, these integrations can be prohibitive when it comes to obtaining the stability properties of a thrust EDB in a wide range of rotor spin speeds for instance. Furthermore, EDBs with a ferromagnetic yoke attached to the winding are not in the scope of this model as Lorentz force law does not apply in this case. A third modelling approach was proposed in [15]. It consists in a linear state-space representation of the system, allowing for straightforward stability analyses. However, it is limited to windings with two phases, although considering a higher number of phases could improve the copper usage and the bearing performances.

In this context, a linear state-space representation of thrust EDBs is introduced without the previous limitations. It is obtained by applying an appropriate change of variables to the electromechanical equations governing the winding currents, the force, and the torque on the bearing rotor [24]. These electromechanical equations are then coupled to the rotor motion equation. This yields a set of linear state-space equations, allowing for straightforward stability analyses.

The model belongs to the category of global models, meaning that it is obtained on the basis of a circuit energetic approach. Therefore, it involves parameters that are not linked to a particular geometry such as the resistance and inductance of the windings, etc. These parameters have to be identified either through experimental measurements or local models, obtained by solving Maxwell's equations.

3.2 Assumptions

In order to establish the state-space model of the EDB, the following assumptions are made:

1. only axial and radial displacements are considered, i.e. the spin axes of the stator and rotor remain parallel;
2. the axial and radial displacements are supposed to be small;
3. the materials have linear magnetic properties i.e. magnetic hysteresis and saturation are neglected;
4. the inductance variations due to rotor axial and radial displacements are neglected;
5. the inductance variations due to the rotor angular position around its spin axis are neglected;
6. the proximity and skin effects in the conductors are neglected;
7. the eddy currents are neglected except in the windings;
8. only the fundamental component of the PMs arrangements magnetic field is considered;
9. the spin speed of the rotor ω is an input of the system and varies slowly compared to the axial dynamics.

The assumptions made on the inductances are verified in the absence of ferromagnetic pieces. However, the assumption 4 becomes weaker if there is a ferromagnetic circuit linked to the PMs arrangements. This is even the more true when ferromagnetic yokes are also present at the armature and even more important if the windings are placed in slotted ferromagnetic circuits. By contrast, the assumption 5 becomes weaker only when there is a ferromagnetic circuit with salliencies linked to the PMs arrangements.

3.3 PM flux linkage

3.3.1 PM magnetic flux density

The purpose of this subsection is to derive the expression of the magnetic flux density in the frame of the armature windings, whether they are at the rotor or at the stator. As stated in section 2, the thrust bearing being analysed is constituted of two subassemblies: the PMs and the armature winding. Each is assigned a frame whose (i) vertical axis Z is aligned with the symmetry axis, (ii) origin is located at half-height of both parts constituting the subassembly and (iii) X axis is aligned with the magnetic axis. More precisely, the coordinates related to the PMs arrangements and armature are $\{r, \theta, Z\}$ and $\{\xi, \psi, a\}$ respectively. As shown in Fig. 3.1, the position of the rotor in the stator frame is (ϵ, ϕ, z). According to assumption 9, the rotor spin angle around its vertical axis is $\alpha = \omega t + \alpha_0$, with α_0 the initial position and ω the spin speed.

For the sake of clarity, let us consider, to derive the following equations, the particular topology with the armature as internal subassembly, an angular shift $\Delta\theta_{PM} = 0$ between both PMs arrangements and a series connection. However, the same analysis can be

applied to the other topologies yielding an identical result. Following the condition (2.7), the angular shift $\Delta\theta_a = 0$. Furthermore, according to assumption 8, the axial component of the magnetic flux density due to the PMs arrangements is modeled as:

$$B(r, \theta, Z) = \cos(p\theta) f(Z) g(r), \tag{3.1}$$

where p is the number of pole pairs and $f(Z)$ as well as $g(r)$ depend on the PMs arrangements and on the presence of ferromagnetic parts at the armature. Besides, the function $f(Z)$ is odd as $\Delta\theta_{PM} = 0$.

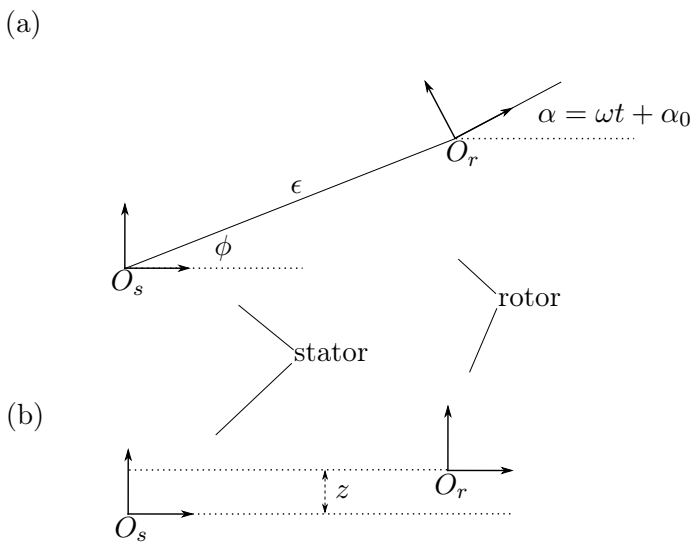

Fig. 3.1: Stator and rotor frames. (a) Upside view. (b) Lateral view.

PMs attached to the stator

Let us now study the case with the PMs attached to the stator. The coordinate transformation from the fixed frame to the rotating frame is:

$$\begin{aligned} r &= \sqrt{\epsilon^2 + \xi^2 + 2\xi\epsilon\cos(\psi + \alpha - \phi)} \\ \theta &= \tan^{-1}\left(\frac{\epsilon\sin(\phi) + \xi\sin(\psi + \alpha)}{\epsilon\cos(\phi) + \xi\cos(\psi + \alpha)}\right) \\ Z &= z + a \end{aligned} \tag{3.2}$$

Substituting (3.2) into (3.1) allows determining the magnetic flux density due to the PMs in the rotor frame:

$$\begin{aligned} B(\xi, \psi, a) = &\cos\left(p\tan^{-1}\left(\frac{\epsilon\sin(\phi) + \xi\sin(\psi + \alpha)}{\epsilon\cos(\phi) + \xi\cos(\psi + \alpha)}\right)\right) \\ &\times g\left(\sqrt{\epsilon^2 + \xi^2 + 2\xi\epsilon\cos(\psi + \alpha - \phi)}\right) \\ &\times f(z + a). \end{aligned} \tag{3.3}$$

According to assumption 2, the axial and radial displacements are small. Therefore, the first order Taylor expansion of (3.3) around the nominal position of the EDB $(\epsilon, z) = (0, 0)$

can be derived and leads to:

$$\begin{aligned} B(\xi,\psi,a) \approx & \cos(p(\psi+\alpha))g(\xi)f(a) \\ & + z\cos(p(\psi+\alpha))g(\xi)\frac{\partial f}{\partial Z}(a) \\ & + \epsilon\cos((\psi+\alpha)(p+1)-\phi)\frac{f(a)}{2}\left(\frac{\partial g}{\partial r}(\xi)-p\frac{g(\xi)}{\xi}\right) \\ & + \epsilon\cos((\psi+\alpha)(p-1)+\phi)\frac{f(a)}{2}\left(\frac{\partial g}{\partial r}(\xi)+p\frac{g(\xi)}{\xi}\right). \end{aligned} \tag{3.4}$$

PMs attached to the rotor

Let us then study the case with the PMs attached to the rotor. The coordinate transformation from the rotating frame to the fixed frame is:

$$\begin{aligned} r &= \sqrt{\xi^2+\epsilon^2-2\epsilon\xi\cos(\psi-\phi)} \\ \theta &= \tan^{-1}\left(\frac{\xi\sin(\psi-\alpha)-\epsilon\sin(\phi-\alpha)}{\xi\cos(\psi-\alpha)-\epsilon\cos(\phi-\alpha)}\right) \\ Z &= a-z \end{aligned} \tag{3.5}$$

Substituting (3.5) into (3.1) yields the magnetic flux density in the stator frame:

$$\begin{aligned} B(\xi,\psi,a) = & \cos\left(p\tan^{-1}\left(\frac{\xi\sin(\psi-\alpha)-\epsilon\sin(\phi-\alpha)}{\xi\cos(\psi-\alpha)-\epsilon\cos(\phi-\alpha)}\right)\right) \\ & \times\ g\left(\sqrt{\xi^2+\epsilon^2-2\epsilon\xi\cos(\psi-\phi)}\right) \\ & \times\ f(a-z). \end{aligned} \tag{3.6}$$

Deriving the first order Taylor expansion of (3.6) around the nominal position of the EDB $(\epsilon, z) = (0, 0)$ leads to:

$$\begin{aligned} B(\xi,\psi,a) \approx & \cos(p(\psi-\alpha))g(\xi)f(a) \\ & + z\cos(p(\psi-\alpha))g(\xi)\frac{\partial f}{\partial Z}(a) \\ & + \epsilon\cos(\psi(p+1)-p\alpha-\phi)\frac{f(a)}{2}\left(-\frac{\partial g}{\partial r}(\xi)-p\frac{g(\xi)}{\xi}\right) \\ & + \epsilon\cos(\psi(p-1)-p\alpha+\phi)\frac{f(a)}{2}\left(-\frac{\partial g}{\partial r}(\xi)+p\frac{g(\xi)}{\xi}\right). \end{aligned} \tag{3.7}$$

3.3.2 General form of PM flux linkage

Let us consider that the coils are made of loops whose surface is given by:

$$S \equiv \begin{cases} R_i \le \xi \le R_o \\ -t(\xi) \le \psi \le t(\xi) \end{cases}, \tag{3.8}$$

where $t(\xi)$ is the function describing the shape of the loop. This single loop can be replicated N_l times at the same location. The set constituted of those N_l loops is duplicated p times at positions β_j such that they are evenly distributed around the symmetry axis:

$$\beta_j = \frac{2\pi(j-1)}{p}, \tag{3.9}$$

with $j = \{1, \ldots, p\}$. Such an arrangement is placed at $a = L/2$ and constitutes a first coil. Remembering that $\Delta\theta_a = 0$, the same arrangement is also placed at $a = -L/2$, forming a second coil. Both coils are connected in series constituting one phase winding and are reproduced N times at positions δ_k, as explained in section 2, in order to form the armature.

The PM flux linked by a single loop defined by its surface S can be obtained as follows:

$$\Phi = \iint_S \mathbf{B} \cdot \mathbf{n}\, dS, \tag{3.10}$$

where $\mathbf{n}$ is the normal vector to the integration surface. As this vector is aligned with the axial component of the magnetic field, the PM flux linkage $\Phi_{w,k}$ of the k-th coil located at a position a is given by:

$$\Phi_{w,k}(a) = N_l \sum_{j=1}^{p} \int_{R_i}^{R_o} \int_{-t(\xi)+\delta_k+\beta_j}^{t(\xi)+\delta_k+\beta_j} B(\xi, \psi, a) d\psi \xi d\xi \tag{3.11}$$

Knowing that the coils of one phase are connected in series, the total flux Φ_k linked by the k-th phase winding is computed as the sum of the flux intercepted by the k-th coils located at $a = L/2$ and $a = -L/2$:

$$\Phi_k = \Phi_{w,k}(L/2) + \Phi_{w,k}(-L/2). \tag{3.12}$$

PMs attached to the stator

Using (3.4) for the case with the PMs attached to the stator, the flux linkage (3.11) becomes:

$$\begin{aligned} \Phi_{w,k}(a) \;=\; N_l \sum_{j=1}^{p} \big[& \cos(p(\alpha + \delta_k + \beta_j)) f(a) K_{s1} \\ & + z \cos(p(\alpha + \delta_k + \beta_j)) \frac{\partial f}{\partial Z}(a) K_{s2} \\ & + \epsilon \cos((p+1)(\alpha + \delta_k + \beta_j) - \phi) f(a) K_{s3} \\ & + \epsilon \cos((p-1)(\alpha + \delta_k + \beta_j) + \phi) f(a) K_{s4} \big], \end{aligned} \tag{3.13}$$

where K_{si} are constants resulting from the integrations. The function $f(Z)$ is odd and thus its first derivative is even, yielding:

$$\begin{aligned} f(L/2) + f(-L/2) &= 0 \\ \frac{\partial f}{\partial Z}(L/2) + \frac{\partial f}{\partial Z}(-L/2) &= 2 \cdot \frac{\partial f}{\partial Z}(L/2). \end{aligned} \tag{3.14}$$

Consequently, the only remaining terms in the total flux (3.12) linked by the k-th phase winding are those proportional to z. Due to the properties of the cosine, it reduces to:

$$\Phi_k = z K_\phi \cos(p(\alpha + \delta_k)), \tag{3.15}$$

where K_ϕ is a constant which depends on the geometric and magnetic parameters of the EDB. Using identical arguments, it is straightforward to proof that the second order Taylor expansion of the magnetic flux density yields the same result. Indeed, the term in ϵ^2 is proportional to $f(a)$ and is then canceled. The term in z^2 is proportional to $\partial^2 f / \partial Z^2(a)$ and the second derivative of an odd function is odd: this term is thus also canceled. Finally, the term in ϵz is proportional to $\partial f / \partial Z(a)$ but the sum over j removes it due to the fact that $\sum_{j=1}^{p} \cos(x + (p \pm 1) 2\pi(j-1)/p) = 0$. Therefore, connecting all the loops of one phase in series allows removing the effect of the eccentricity ϵ at second order.

PMs attached to the rotor

Let us follow the same method for the case where the PMs are attached to the rotor. Substituting (3.7) into (3.11) yields:

$$\begin{aligned}\Phi_{w,k}(a) = N_l \sum_{j=1}^{p} [&\cos(p(\delta_k + \beta_j - \alpha)) f(a) K_{r1} \\ &+ z \cos(p(\delta_k + \beta_j - \alpha)) \frac{\partial f}{\partial Z}(a) K_{r2} \\ &+ \epsilon \cos((p+1)(\delta_k + \beta_j) - p\alpha - \phi) f(a) K_{r3} \\ &+ \epsilon \cos((p-1)(\delta_k + \beta_j) - p\alpha + \phi) f(a) K_{r4}] ,\end{aligned} \tag{3.16}$$

where K_{ri} are constants resulting from the integrations. Based on (3.14), (3.16) and the properties of the cosine, the total flux linkage (3.12) reduces to:

$$\Phi_k = z K_\phi \cos(p(\delta_k - \alpha)), \tag{3.17}$$

where K_ϕ is a constant which depends on the geometric and magnetic parameters of the EDB. As for the case with the PMs attached to the stator, it is straightforward to proof that the second order Taylor expansion of the magnetic field yields an identical result.

Analysis

The expressions (3.15) and (3.17) of the flux linkage for both cases only differ through the sign of the rotor angular position α and therefore its direction of rotation. Hence, later in this study, both cases are reduced to the same general case described by (3.17). This expression only depends on the rotor axial displacement and angular position and not on the eccentricity. Moreover, as expected, the flux linkage is null when there is no axial displacement to respect the null-flux principle.

3.4 Governing equations

In this section, the electrical and electromechanical equations describing the dynamics of the EDB are derived.

3.4.1 Electrical equations

As stated in section 2, each of the N phase windings are short-circuited. Applying Faraday's law to the k-th phase yields:

$$u_k = 0 = R_k I_k + \frac{d\Psi_k}{dt}, \tag{3.18}$$

where R_k is the phase resistance and Ψ_k the total magnetic flux linkage. This flux can be separated into two contributions, one due to the PMs and the other due to the inductances:

$$0 = R_k I_k + \frac{d\left(\sum_{l=1}^{N} L_{kl} I_l\right)}{dt} + \frac{d\Phi_k}{dt}, \tag{3.19}$$

where L_{kl} are the phase self and mutual inductances and Φ_k is the magnetic flux linkage due to PMs. According to assumptions 4 and 5, the inductances do not depend on the rotor position and are therefore time-independent, leading to:

$$0 = R_k I_k + \sum_{l=1}^{N} L_{kl} \frac{dI_l}{dt} + \frac{d\Phi_k}{dt}. \tag{3.20}$$

This equation can be expressed in matrix form as:

$$\mathbf{0} = \mathbf{R}\mathbf{I} + \mathbf{L}\frac{d\mathbf{I}}{dt} + \frac{d\mathbf{\Phi}}{dt}. \tag{3.21}$$

As previously specified, the winding phases are identical and so are the phase resistance:

$$\mathbf{R} = R\mathbb{1}, \tag{3.22}$$

where $\mathbb{1}$ is the identity matrix. Besides, the phases are evenly distributed and their properties constant. Hence, the matrix $\mathbf{L}$ is symmetric and circulant:

$$\begin{aligned} L_{kl} &= L_{lk} \\ L_{kl} &= L_{k+i,l+i} \\ L_{1l} &= L_{1,N+2-l}, \end{aligned} \tag{3.23}$$

where $i, k, l \in \{1, \ldots, N\}$. Finally, without modifying the properties (3.23), external inductors of equal impedances can be connected in series with each phase winding. This enables to change the dynamic properties of the EDB [9].

3.4.2 Electromechanical equations

As shown in section 3.3, the flux linkage $\mathbf{\Phi}$ due to the PMs only depends on the rotor axial displacement z and angular position α. Therefore, the electrodynamic forces and torques are reduced to the axial ones:

$$F = \sum_{k=1}^{N} \frac{\partial \Phi_k}{\partial z} I_k \tag{3.24}$$

$$T = \sum_{k=1}^{N} \frac{\partial \Phi_k}{\partial \alpha} I_k, \tag{3.25}$$

Considering Φ_k and I_k as complex variables, these expressions can be rewritten in the following matrix form:

$$F = \left[\frac{\partial \mathbf{\Phi}}{\partial z}\right]^T \mathbf{I}^* \tag{3.26}$$

$$T = \left[\frac{\partial \mathbf{\Phi}}{\partial \alpha}\right]^T \mathbf{I}^*, \tag{3.27}$$

where $\mathbf{I}^*$ represents the complex conjugate of $\mathbf{I}$.

According to assumptions 4 and 5, the inductance matrix $\mathbf{L}$ is constant. Therefore, the reluctant efforts are equal to zero. Besides, detent efforts could appear due to interaction of the PMs arrangements with ferromagnetic parts located at the armature. Hereinafter, their contributions to the electromagnetic efforts are taken into account in the form of external efforts on the rotor, see section 3.6.2.

3.5 Variables elimination

The study of the present EDB has some similarities with the study of N-phased rotating field machines. As for the rotating field machines, it is possible to reduce the number of variables needed to describe the operation of EDBs through an appropriate transformation. This is done in this section, following the approach described in [24]. Let us define the variables transformation:

$$\begin{aligned} \mathbf{I} &= \mathbf{U}\mathbf{I^s} \\ \mathbf{\Phi} &= \mathbf{U}\mathbf{\Phi^s}, \end{aligned} \tag{3.28}$$

with:

$$U_{kl} = \frac{1}{\sqrt{N}} e^{-j(k-1)(l-1)\frac{2\pi}{N}}, \tag{3.29}$$

where $j = \sqrt{-1}$ and $k, l \in \{1, \ldots, N\}$.

3.5.1 Electrical equations

Substituting (3.28) into (3.21) yields:

$$\mathbf{0} = R\mathbf{U}\mathbf{I^s} + \mathbf{L}\mathbf{U}\frac{d\mathbf{I^s}}{dt} + \mathbf{U}\frac{d\mathbf{\Phi^s}}{dt}. \tag{3.30}$$

The inverse of matrix $\mathbf{U}$ is given in [24]:

$$U^{-1}_{kl} = \frac{1}{\sqrt{N}} e^{j(k-1)(l-1)\frac{2\pi}{N}} = U^*_{kl}. \tag{3.31}$$

Pre-multiplying (3.30) by $\mathbf{U^{-1}}$ leads to:

$$\mathbf{0} = R\mathbf{I^s} + \mathbf{U^{-1}}\mathbf{L}\mathbf{U}\frac{d\mathbf{I^s}}{dt} + \frac{d\mathbf{\Phi^s}}{dt}. \tag{3.32}$$

Defining $\mathbf{L^s} = \mathbf{U^{-1}}\mathbf{L}\mathbf{U}$, (3.32) becomes:

$$\mathbf{0} = R\mathbf{I^s} + \mathbf{L^s}\frac{d\mathbf{I^s}}{dt} + \frac{d\mathbf{\Phi^s}}{dt}, \tag{3.33}$$

where the N equations are decoupled due to the propertie of $\mathbf{U}$ and (3.23). The diagonal terms of $\mathbf{L^s}$ can be calculated as:

$$L^s_{ii} = \sum_{k=1}^{N} L_{1k} e^{-j(i-1)(k-1)\frac{2\pi}{N}}, \tag{3.34}$$

where $k = 1, \ldots, N$. The flux linkage $\mathbf{\Phi^s}$ can be derived relying on (3.17) and (3.28). The details are available in the appendix A and yield:

$$\mathbf{\Phi^s} = z\frac{K_\Phi\sqrt{N}}{2} \begin{bmatrix} 0 \\ \exp(jp(\alpha - \delta_0)) \\ 0 \\ \vdots \\ 0 \\ \exp(-jp(\alpha - \delta_0)) \end{bmatrix}. \tag{3.35}$$

Therefore, among the N decoupled equations in (3.33), two present a non-homogeneous term. As a result, only the two corresponding currents I_2^s and I_N^s are non-zero. Defining:

$$\mathbf{\Phi^r} = \begin{bmatrix} \Phi_2^s \\ \Phi_N^s \end{bmatrix} = z\frac{K_\Phi\sqrt{N}}{2}\begin{bmatrix} \exp(jp(\alpha-\delta_0)) \\ \exp(-jp(\alpha-\delta_0)) \end{bmatrix} \tag{3.36}$$

$$\mathbf{I^r} = \begin{bmatrix} I_2^s \\ I_N^s \end{bmatrix}, \tag{3.37}$$

the number electrical of equations is reduced from N to 2 which gives:

$$\mathbf{0} = R\mathbf{I^r} + \mathbf{L^r}\frac{d\mathbf{I^r}}{dt} + \frac{d\mathbf{\Phi^r}}{dt}. \tag{3.38}$$

The inductance of both phases are equal:

$$L_c = L_{22}^r = L_{NN}^r = \sum_{k=1}^{N} L_{1k}\cos\left((k-1)\frac{2\pi}{N}\right), \tag{3.39}$$

where L_c is the cyclic inductance of the winding. The two elements of the flux linkage (3.36) are complex conjugates. Therefore, both equations in (3.38) are complex conjugates and so are the two resulting currents. The system (3.38) reduces to:

$$\begin{cases} 0 = RI_1^r + L_c\dfrac{dI_1^r}{dt} + \dfrac{d\Phi_1^r}{dt} \\ I_1^r = I_2^{r*} \end{cases}. \tag{3.40}$$

Substituting the flux linkage Φ_1^r by its expression (3.36) into (3.40) and multiplying by $\exp(-jp(\alpha-\delta_0))$ yields:

$$\begin{aligned} 0 = R[I_1^r\exp(-jp(\alpha-\delta_0))] + L_c\Bigg[\frac{d}{dt}[I_1^r\exp(-jp(\alpha-\delta_0))] \\ + jp\dot{\alpha}[I_1^r\exp(-jp(\alpha-\delta_0))]\Bigg] + \frac{K_\Phi\sqrt{N}}{2}(\dot{z} + jp\dot{\alpha}z). \end{aligned} \tag{3.41}$$

Let us define:

$$Y = I_1^r\exp(-jp(\alpha-\delta_0)). \tag{3.42}$$

Substituting (3.42) into (3.41), this equation can be separated into real and imaginary parts as follows:

$$\begin{cases} 0 = R\cdot\Re(Y) + L_c\left[\dfrac{d\Re(Y)}{dt} - \dot{\alpha}p\Im(Y)\right] + \dfrac{K_\Phi\sqrt{N}}{2}\dot{z} \\ 0 = R\cdot\Im(Y) + L_c\left[\dfrac{d\Im(Y)}{dt} + \dot{\alpha}p\Re(Y)\right] + \dfrac{K_\Phi\sqrt{N}}{2}\dot{\alpha}pz \end{cases}. \tag{3.43}$$

3.5.2 Electromechanical equations

Force

The force can be calculated by substituting (3.28) into (3.26):

$$\begin{aligned} F &= \left[\frac{\partial(\mathbf{U\Phi^s})}{\partial z}\right]^T(\mathbf{UI^s})^* \\ &= \frac{\partial[\mathbf{\Phi^s}]^T}{\partial z}\mathbf{U}^T\mathbf{U}^*\mathbf{I^{s*}} \end{aligned} \tag{3.44}$$

Knowing that $\mathbf{U}^T = \mathbf{U}$ and $\mathbf{U}^* = \mathbf{U}^{-1}$, (3.44) becomes:

$$F = \frac{\partial[\mathbf{\Phi^s}]^T}{\partial z}\mathbf{I^{s*}} \tag{3.45}$$

As stated in (3.35), $\mathbf{\Phi^s}$ has only two non-zero components which yields:

$$F = \frac{\partial[\mathbf{\Phi^r}]^T}{\partial z}\mathbf{I^{r*}} \tag{3.46}$$

The flux linkage can be replaced by its expression (3.36). Moreover, remembering that $I_2^{r*} = I_1^r$, (3.46) becomes:

$$F = \frac{K_\Phi\sqrt{N}}{2}[I_1^{r*}\exp(jp(\alpha - \delta_0)) + I_1^r\exp(-jp(\alpha - \delta_0))]. \tag{3.47}$$

Substituting (3.42) into (3.47) yields:

$$\begin{aligned} F &= \frac{K_\Phi\sqrt{N}}{2}[Y^* + Y] \\ &= K_\Phi\sqrt{N}\cdot\Re(Y). \end{aligned} \tag{3.48}$$

Torque

The same development applied to the expression of the torque (3.27) gives:

$$T = \frac{\partial[\mathbf{\Phi^r}]^T}{\partial \alpha}\mathbf{I^{r*}} \tag{3.49}$$

Replacing the flux linkage by its expression (3.36) and taking into account that $I_2^{r*} = I_1^r$ leads to:

$$\begin{aligned} T &= jpz\frac{K_\Phi\sqrt{N}}{2}[I_1^{r*}\exp(jp(\alpha - \delta_0)) - I_1^r\exp(jp(\delta_0 - \alpha))] \\ &= jpz\frac{K_\Phi\sqrt{N}}{2}[Y^* - Y] \\ &= pzK_\Phi\sqrt{N}\cdot\Im(Y) \end{aligned} \tag{3.50}$$

3.6 State-space model derivation

Let us now derive the state-space model of the EDTB based on the previous relations. Isolating $\Re(Y)$ in (3.48) and $\Im(Y)$ in (3.50) yields:

$$\Re(Y) = F\cdot\frac{1}{K_\Phi\sqrt{N}}. \tag{3.51}$$

$$\Im(Y) = \frac{T}{z}\cdot\frac{1}{pK_\Phi\sqrt{N}} \tag{3.52}$$

Substituting those expressions into (3.43) and multiplying by $K_\Phi\sqrt{N}$ gives:

$$\begin{cases} 0 = RF + L_c\left[\dot{F} - \dot{\alpha}\left(\dfrac{T}{z}\right)\right] + \dfrac{K_\Phi^2 N}{2}\dot{z} \\ 0 = \dfrac{R}{p}\left(\dfrac{T}{z}\right) + L_c\left[\dfrac{1}{p}\left(\dfrac{\dot{T}}{z}\right) + \dot{\alpha}pF\right] + \dfrac{K_\Phi^2 N}{2}\dot{\alpha}pz \end{cases}. \tag{3.53}$$

The system of ordinary differential equations in (3.53) can be rearranged as follows:

$$\begin{cases} \dot{F} = -\dfrac{R}{L_c}F + \dot{\alpha}\left(\dfrac{T}{z}\right) - \dfrac{K_\Phi^2 N}{2L_c}\dot{z} \\ \left(\dfrac{\dot{T}}{z}\right) = -\dfrac{R}{L_c}\left(\dfrac{T}{z}\right) - \dot{\alpha}p^2 F - \dfrac{K_\Phi^2 N}{2L_c}\dot{\alpha}p^2 z \end{cases}. \tag{3.54}$$

This last system of two equations describes the complete dynamics of the EDB by linking the axial displacement, the force, the torque (position-related) and their derivatives. Based on assumption 9, the rotor angular speed $\dot{\alpha}$ is replaced by ω. Therefore, (3.54) is a linear system with constant coefficients.

3.6.1 Rotor mechanical model coupling

The system in (3.54) only describes the dynamics of the EDB and must then be coupled with a mechanical model of the rotor. The dynamics of an one degree of freedom damped rotor is governed by:

$$M\ddot{z} + C\dot{z} = F + F_e, \tag{3.55}$$

where M is the rotor mass, C the damping factor and F_e are the external axial forces acting on the rotor. Coupling (3.55) with (3.54) leads to:

$$\begin{bmatrix} \dot{F} \\ \left(\dfrac{\dot{T}}{z}\right) \\ \dot{z} \\ \ddot{z} \end{bmatrix} = \mathbf{A} \begin{bmatrix} F \\ \left(\dfrac{T}{z}\right) \\ z \\ \dot{z} \end{bmatrix} + \mathbf{B} \cdot F_e, \tag{3.56}$$

where:

$$\mathbf{A} = \begin{bmatrix} -\dfrac{R}{L_c} & \omega & 0 & -\dfrac{K_\Phi^2 N}{2L_c} \\ -\omega p^2 & -\dfrac{R}{L_c} & -\omega p^2 \dfrac{K_\Phi^2 N}{2L_c} & 0 \\ 0 & 0 & 0 & 1 \\ \dfrac{1}{M} & 0 & 0 & -\dfrac{C}{M} \end{bmatrix}, \tag{3.57}$$

$$\mathbf{B} = \frac{1}{M}\begin{bmatrix} 0 & 0 & 0 & 1 \end{bmatrix}^T. \tag{3.58}$$

3.6.2 Detent force and torque

As stated in section 3.4.2, detent efforts could appear due to the interaction of the PMs arrangements with ferromagnetic parts located at the armature. Under the small displacement assumption, the detent force can be associated with a constant negative stiffness K_d. Up to this point, it was taken into account in the external forces F_e, which can therefore be separated as follows:

$$F_e = F_e^{'} - K_d z, \tag{3.59}$$

where $F_e^{'}$ are the external axial forces without the contribution of the detent force. Therefore, the electromagnetic force $F^{'}$ is:

$$F^{'} = F - K_d z \tag{3.60}$$

Substituting (3.59) and (3.60) into (3.56), the state-space model of the EDB becomes:

$$\begin{bmatrix} \dot{F}' \\ \left(\dfrac{\dot{T}}{z}\right) \\ \dot{z} \\ \ddot{z} \end{bmatrix} = \mathbf{A}' \begin{bmatrix} F' \\ \left(\dfrac{T}{z}\right) \\ z \\ \dot{z} \end{bmatrix} + \mathbf{B} \cdot F_e', \tag{3.61}$$

where:

$$\mathbf{A}' = \mathbf{A} + K_d \begin{bmatrix} 0 & 0 & -R/L_c & -1 \\ 0 & 0 & -\omega p^2 & 0 \\ 0 & 0 & 0 & 0 \\ 0 & 0 & 0 & 0 \end{bmatrix}. \tag{3.62}$$

By contrast, the effect of a possible detent torque, which would come from the presence of salliencies located at the armature, can not be taken into account in this model as the spin speed is considered to be constant, according to assumption 9.

3.6.3 Phase currents derivation

The state-space representation (3.61) describes the axial dynamics of EDTBs without solving for the phase currents. However, calculating these latter may be required to perform a thermal analysis e.g. Knowing the force F and the torque T, they can be derived as follows. The currents I_2^s and I_N^s can be determined through (3.37), the second identity in (3.40), and (3.42), yielding:

$$\begin{aligned} I_2^s &= I_1^r = Y \exp(jp(\alpha - \delta_0)) \\ I_N^s &= I_2^r = I_2^{s*} \end{aligned} \tag{3.63}$$

Besides, considering (3.51) and (3.52) leads to:

$$Y = \frac{1}{K_\Phi \sqrt{N}} \left(F + j \frac{T}{pz} \right). \tag{3.64}$$

The instantaneous current I_k in the k-th phase is finally obtained through (3.28):

$$I_k = \frac{2}{K_\Phi N} \left(F \cos(p(\alpha - \delta_k)) - \frac{T}{pz} \sin(p(\alpha - \delta_k)) \right). \tag{3.65}$$

3.6.4 Model parameters determination

The model (3.61) comprises eight parameters. Among these, two are the rotor mass M and the damping C, whose determination is not detailed here. The six remaining parameters only depend on the geometry as well as the magnetic and electrical properties of the thrust bearing: the number p of pole pairs, the number N of winding phases, the phase resistance R, the cyclic inductance L_c, the coefficient K_Φ and the detent stiffness K_d.

These parameters can be determined in two different ways. On the one hand, they can be calculated through analytical formulas and models. On the other hand, they can be identified using either experimental data or finite element methods, as explained hereinafter.

Through the expression (3.39), the cyclic inductance is directly linked to the self inductance L_{11} and the mutual inductances L_{1k}. The self inductance can be calculated by injecting a current I in one phase and evaluating the magnetic energy $W_{m,1}$ stored in the system:

$$L_{11} = \frac{2W_{m,1}}{I^2}. \tag{3.66}$$

The mutual inductances can be determined by injecting a current I in both phases 1 and k and evaluating the magnetic energy $W_{m,2}$ stored in the system:

$$L_{1k} = \frac{W_{m,2}}{I^2} - L_{11}. \tag{3.67}$$

In both case, the remanent magnetization of the permanent magnets has to be cancelled.

The detent stiffness K_d corresponds to the stiffness of the EDB in quasi-static conditions at zero spin speed, i.e. $\dot{z} = 0$ and $\omega = 0$. Therefore, based on (3.60) and considering an axial displacement z, the coefficient K_d is given by:

$$K_d = -\frac{F'(z)}{z}. \tag{3.68}$$

The coefficient K_Φ can be identified through the relation (3.17) by evaluating, for an axial displacement z, the flux linked by a phase winding in an angular position maximising this flux linkage and in quasi-static conditions at zero spin speed, i.e. $\dot{z} = 0$ and $\omega = 0$:

$$K_\Phi = \frac{\Phi(z)}{z}. \tag{3.69}$$

3.7 Practical case

Let us consider the EDB shown in Fig. 3.2. It corresponds to the topology with the armature windings as internal subassembly and the distance L reduced to zero. The subassembly constituted of the PMs arrangements is attached to the stator and presents ferromagnetic yokes. The PMs remanent magnetization is 1.42 [T] and the number p of pole pairs is 3. The armature winding is composed of ten phases ($N = 10$) whose geometry is shown in Fig. 3.3. Each phase is constituted of only one loop ($N_l = 1$). The forward and return conductors of the phase windings are shifted vertically by a distance h_t, which allows interlocking the phases and therefore increasing their number. Lastly, the dimensions of the EDB are given in Table 3.1.

Table 3.1: Bearing dimensions [mm].

R_i	R_{ii}	R_{ee}	R_e	h_y	h_{PM}	h_t	e
5	10	40	50	3	6	1	10

3.7.1 Flux linkage validation

The general form of the flux linkage due to the PMs, based on a second order Taylor expansion of the magnetic field, is given in (3.17). As stated in section 3.3.2, it only depends on z and α. Let us consider a single phase whose angular position maximizes the flux linked. The evolution of this flux for axial and radial displacements from -0.5 [mm] to

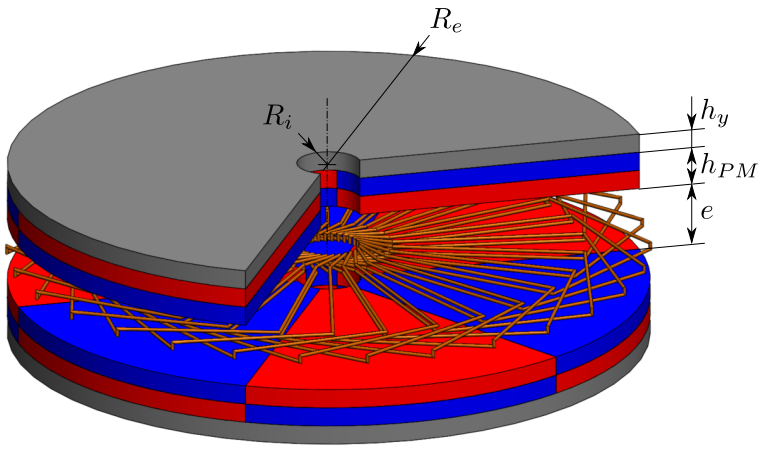

Fig. 3.2: Application: bearing with PMs arrangements attached to the stator and a single layer of phase windings.

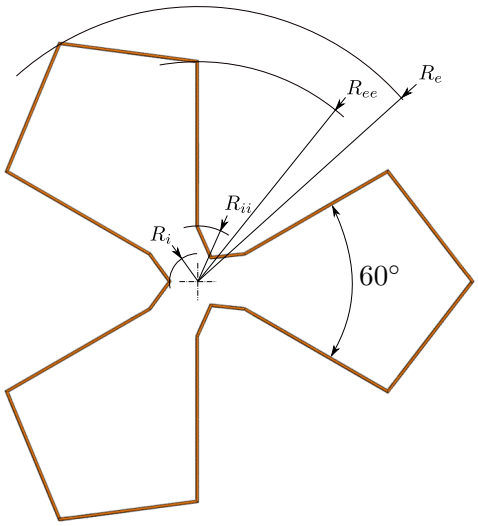

Fig. 3.3: Application: phase winding geometry.

0.5 [mm] is obtained through finite element methods and shown in Fig. 3.4. The surface can be approximated in the least-squares sense by:

$$\Phi(\epsilon, z) = a + bz + c\epsilon, \tag{3.70}$$

where z as well as ϵ are expressed in meters and with:

$$a = 0.0000 \quad b = 0.1810 \quad c = 0.0000 \tag{3.71}$$

The norm of the residuals of this approximation related to the maximal flux yields 1.75%. The coefficient of the term in ϵ as well as the offset are null. Therefore, under small displacements assumption, the flux linkage reduces to:

$$\Phi(z) = bz = K_\Phi z, \tag{3.72}$$

which validates the model and allows determining the coefficient K_Φ.

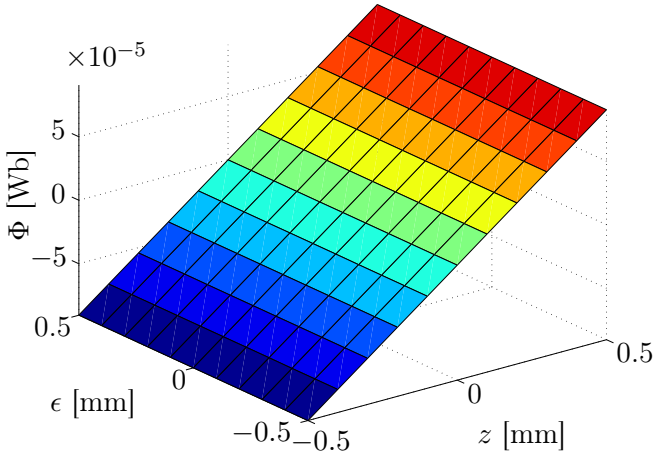

Fig. 3.4: Application: evolution of the flux Φ linked by a single phase with axial and radial displacements.

3.7.2 Parameters identification

Applying the methods described in section 3.6.4, the different parameters of the model are determined for the particular geometry being analysed. The coefficient K_Φ was obtained previously through finite element methods. The winding phase resistance R is calculated using Pouillet's law and the cyclic inductance is determined with the energy-based method. The stiffness K_d is zero as there are no ferromagnetic parts at the armature. The results are listed in Table 3.2. Besides, the rotor mass M is set arbitrarily to 1 [kg] as well as the damping factor C to 0 [Ns/m].

Table 3.2: Model parameters.

R [mΩ]	L_c [μH]	K_Φ [Wb/m]	K_d [N/m]
32.4	0.659	0.181	0

3.7.3 Quasi-static analysis

In quasi-static conditions, i.e. $\dot{z} = 0$, the system (3.54) reduces to:

$$\begin{cases} F = -z \cdot \dfrac{N}{2} \cdot \dfrac{p^2 K_\Phi^2 \omega^2 L_c}{R^2 + (p\omega L_c)^2} \\ T = -z^2 \cdot \dfrac{N}{2} \cdot \dfrac{p^2 K_\Phi^2 \omega R}{R^2 + (p\omega L_c)^2} \end{cases} . \tag{3.73}$$

Therefore, the electrodynamic force F tends to bring the rotor back in its axial nominal position, as expected. By contrast, the electrodynamic torque T contributes to decrease the spin speed and is then a braking torque. The quasi-static efforts offer the advantage that they can be easily measured and thus exploited to validate the model through experimental

results. Besides, for a speed tending to infinity, the efforts become:

$$\begin{cases} F_\infty = -z \cdot \dfrac{N}{2} \cdot \dfrac{K_\Phi^2}{L_c} \\ T_\infty = 0 \end{cases}. \tag{3.74}$$

The maximal axial stiffness K_f is thus given by $NK_\Phi^2/2L_c$ while the torque falls to zero. Furthermore, taking the spin speed equal to the electrical pole R/L_c, through the number p of pole pairs, yields:

$$\begin{cases} F_p = -z \cdot \dfrac{N}{4} \cdot \dfrac{K_\Phi^2}{L_c} \\ T_p = -z^2 \cdot p \cdot \dfrac{N}{4} \cdot \dfrac{K_\Phi^2}{L_c} \end{cases}. \tag{3.75}$$

Hence, for this particular speed, the force exerted by the bearing is half of the maximal one. It allows to determine experimentally the maximal force while driving the rotor at a reasonable spin speed. Furthermore, the braking torque exerted by the EDTB attains its maximal value for this speed. This is consistent with previous results [15]. Taking the ratio of both expressions in (3.73) yields:

$$\frac{F}{T} = \frac{\omega L_c}{R} \cdot \frac{1}{z}. \tag{3.76}$$

Hence, an inductive behaviour of the windings favours the restoring force while a resistive behaviour favours the braking torque, degrading the performance of the EDB.

Let us apply the expressions of the quasi-static force and torque in (3.73) to the bearing being analysed. Fig. 3.5 shows the evolution of the electrodynamic force (solid lines) and torque (dotted lines) with spin speed for several axial displacements. Purely inductive behaviour appears for spin speeds greater than 500 000 [rad/s], yielding a maximal force of 248.5 [N] for an axial displacement $z = 1$ [mm]. For an identical z and a speed equal to 1000 [rad/s], which is a more reasonable speed, the force falls to 0.9 [N]. Nevertheless, it should be recalled that the aim of the thrust bearing studied here is to provide a stabilising effect and not to sustain the complete rotor. Otherwise, the EDTB would remain out of its nominal position and would not take advantage of the losses reduction due to the null-flux principle. Therefore, the EDB can work properly even if the electrodynamic force is small.

Finally, the RMS phase current I_{RMS} in quasi-static conditions is obtained by substituting (3.73) in (3.65), yielding:

$$I_{RMS} = \frac{1}{\sqrt{2}} \frac{zK_\Phi p\omega}{\sqrt{R^2 + (p\omega L_c)^2}}. \tag{3.77}$$

It allows to determine the RMS current density as well as the Joule losses.

3.7.4 Root locus analysis

Fig. 3.6 illustrates the root locus of the state-space model. It is derived by calculating the eigenvalues of the matrix $\mathbf{A}'$ in (3.62) for different spin speeds $\omega \in [0, 10^6]$ [rad/s]. Among the four eigenvalues, two are always in the left half plane, far from the imaginary axis and are then stable. The other two are located near to this axis and are thus more relevant for the stability analysis. A zoom on the root locus for those roots is shown in Fig. 3.7. It can be observed that the thrust bearing is stable up to a spin speed ω_u at which the

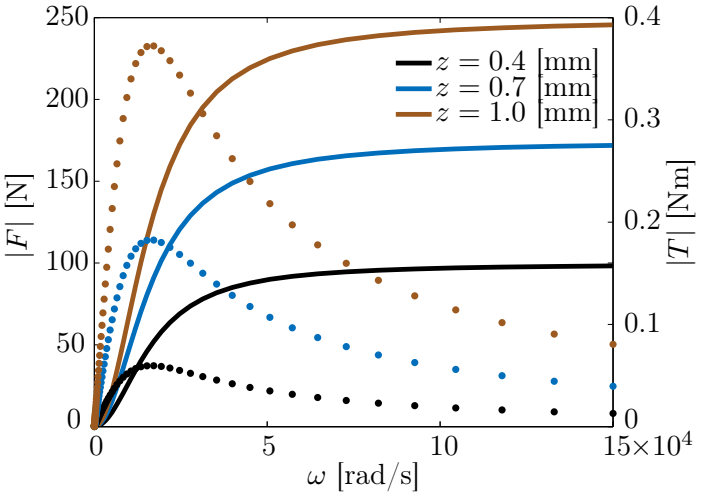

Fig. 3.5: Application: force (solid lines) and torque (dotted lines) evolution with spin speed in quasi-static conditions ($\dot{z} = 0$).

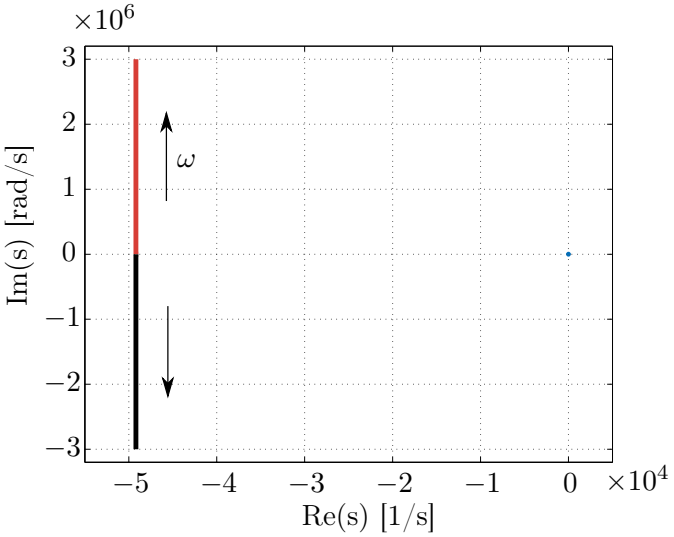

Fig. 3.6: Application: root loci of the EDB.

roots cross the imaginary axis. At higher speeds, the EDB becomes unstable and remains so for speed tending to infinity. This was already noticed in [15]. Provided that both the detent stiffness and the damping factor are zero, the unstability spin speed ω_u can be easily determined analytically, yielding:

$$\omega_u = \frac{1}{p}\sqrt{\frac{K_\Phi^2 N}{2L_c M} + \frac{R^2}{L_c^2}}, \tag{3.78}$$

the details of the calculations being available in appendix B. Considering that the second term of the square root is dominant, this expression can be further simplified, leading to:

$$\omega_u = \frac{1}{p}\frac{R}{L_c}. \tag{3.79}$$

Hence, the unstability spin speed corresponds to the electrical pole R/L_c. Applying the relation (3.79) to the practical case yields 16 395 [rad/s].

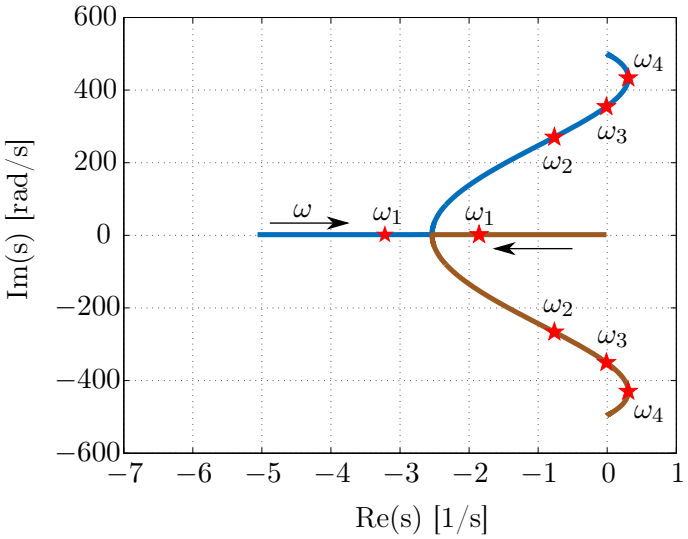

Fig. 3.7: Application: zoom on the interesting root loci of the EDB.

Unlike the radial electrodynamic bearings, the axial EDBs are stable at low speed, even with a damping factor equal to zero [13]. However, adding external damping allows improving dynamic stability. The effect on the relevant poles is illustrated in Fig. 3.8 where $C = 1$ [Ns/m]: the poles move to the left by an amount proportional to C, leading, in this case, to an unconditionally stable EDB. Therefore, the model presented in this chapter allows determining, when it is required, the minimal damping factor ensuring stability for a targeted speed. Finally, this external damping between the stator and the rotor should preferably be contactless to be consistent with the magnetic bearing approach.

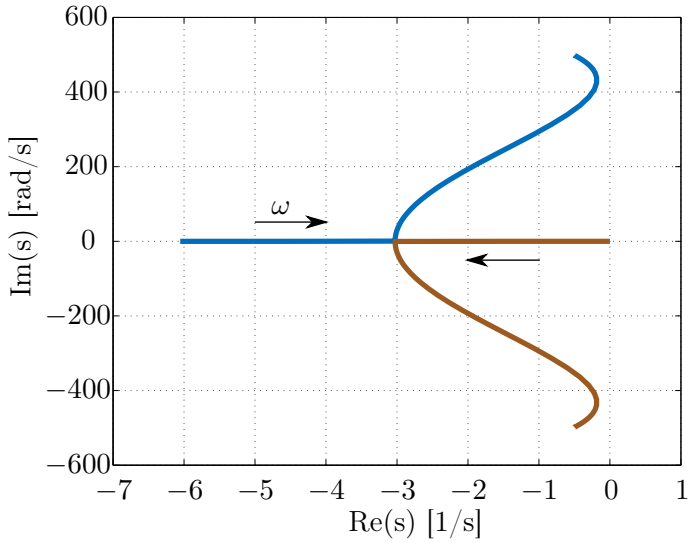

Fig. 3.8: Application: effect of an external damping $C = 1$ [Ns/m] on the relevant poles.

3.7.5 Dynamic analysis

Let us analyse the dynamic behavior of the thrust bearing for an initial axial displacement equal to 1 [mm] and the four speeds corresponding to the stars in Fig. 3.7. As observed in the root loci, when the spin speed is $\omega_1 = 80$ [rad/s], both relevant poles are real and stable, meaning that the system is overdamped. The evolution of the axial displacement with time is illustrated in Fig. 3.9a: as expected, there are no oscillations. For a spin speed $\omega_2 = 10\,500$ [rad/s], the poles are complex conjugates and stable. The system is thus underdamped, as shown in Fig. 3.9b. In the third case, the spin speed is maintained to $\omega_3 = 16\,395$ [rad/s]. It corresponds to the speed leading to a zero real part for both poles: the system is thus marginally stable and oscillates with a constant amplitude, as can be seen in Fig. 3.9c. Lastly, when the speed is $\omega_4 = 28\,400$ [rad/s], corresponding to the maximal positive real part for both poles on the root loci, the system is unstable, as shown in Fig. 3.9d.

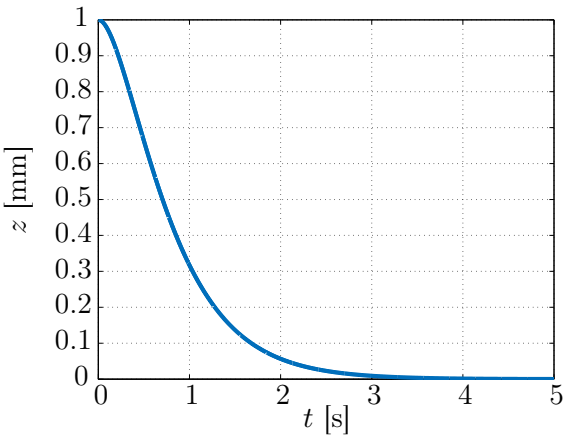

(a) Spin speed maintained at 80 [rad/s].

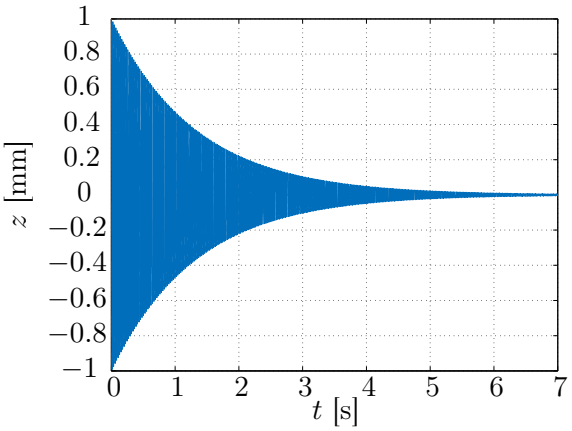

(b) Spin speed maintained at 10 500 [rad/s].

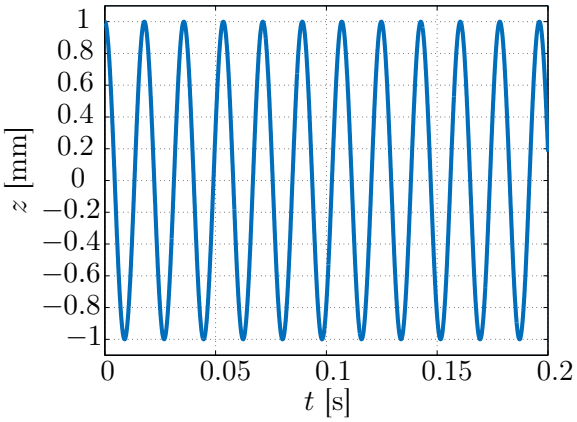

(c) Spin speed maintained at 16 395 [rad/s].

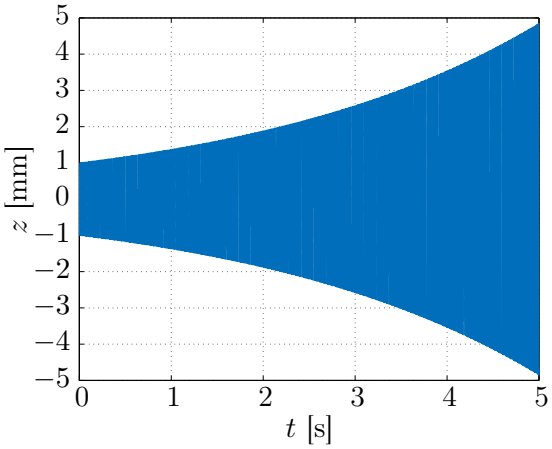

(d) Spin speed maintained at 28 400 [rad/s].

Fig. 3.9: Application: evolution of z with time when the initial axial displacement is 1 [mm] for different spin speeds.

CHAPTER 4

EXPERIMENTAL VALIDATION

This chapter intends to validate and benefit from the model derived hereinabove through the prototyping of an electrodynamic thrust bearing. This prototype is based on one of the new topologies presented in the second chapter. This chapter is structured as follows. First, the topology being analysed is described in details, and, especially, the design of the windings. The test bench allowing to implement the thrust bearing is later presented. Following on from this, taking advantage of the proposed model, the dynamics as well as the quasi-static behaviour of the EDB are analysed after the identification of the parameters. Finally, experimental results are compared to the theory and model predictions.

4.1 Prototype

4.1.1 Topology

The thrust bearing being analysed in this experimental validation corresponds to the topology with the armature windings as external subassembly. For construction reasons, the distance L between both parts of the internal subassembly, namely the PMs arrangements, is small but not reduced to zero. The number p of pole pairs of both subassemblies is six ($p = 6$). It offers the advantage to allow using the same PMs to obtain three pole pairs PMs arrangements by gathering the PMs by pairs polarised in the same direction. The maximal accepted axial displacement of the rotor around its nominal position is 1.5 [mm] in each direction. The angular shift $\Delta\theta_{PM}$ between each part of the PMs arrangements is equal to $\pi/p = 30°$, meaning that they are in attractive mode. Therefore, considering an opposition connection of the coils and following the conditions derived in section 2.2, the angular shift $\Delta\theta_a$ must be equal to zero. The expected behaviour is thus identical to the degenerated topology shown in Fig. 2.3b.

The armature is fixed to the stator, offering two main advantages. On the one hand, it yields a direct access to the armature winding, thereby allowing to measure the voltage induced in the different phases when the rotor is not in its axial nominal position. It enables to validate the working principle and to determine experimentally the coefficient K_Φ. On the other hand, it provides the possibility to easily choose and modify the type of connection between the coils composing the armature winding. Furthermore, the number N of phases is three, leaving the opportunity to connect a three-phase power supply to the armature windings so that the thrust bearing could be used for both guiding and driving the rotor, as will be explained later. The permanent magnets arrangements are therefore located on the rotor.

Finally, two different types of armature windings are considered for this experimental validation. On the one hand, overlapping distributed windings with integral pitch are printed on a PCB. On the other hand, non-overlapping concentrated windings with fractional pitch are wire-wound on a support.

4.1.2 Rotor

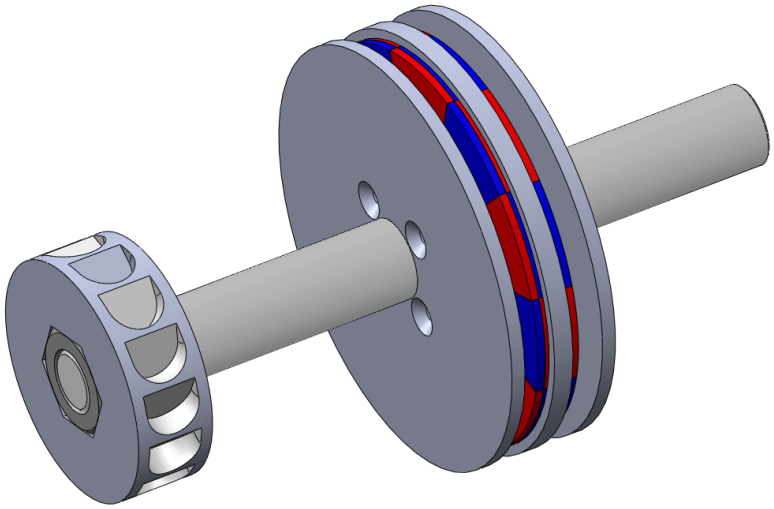

Fig. 4.1: Overview of the complete rotor.

As mentioned above, the rotor comprises the permanent magnets arrangements. Fig. 4.1 provides an overview of the rotor. As shown in the cross-sectional view in Fig. 4.2, it is composed of three elements:

a) a ferromagnetic yoke (1) on which the PMs (2) are attached;

b) two back irons (3) and (4) placed on both sides of the yoke;

c) two shafts (5) and (6) which are screwed together through the ferromagnetic yoke;

These elements are further explained hereinafter, as well as the component having the number (7) and their drawings are available in appendix L.

PMs arrangements

As the number of pole pairs is six, each permanent magnets arrangement consists of 12 segment magnets of 30°, as shown in Fig. 4.3a. For construction reasons, the arrangement is replicated on both side of the ferromagnetic yoke in an attractive mode, leading to a non-zero distance L. Besides, for the sake of simplicity, they are composed of surface-mounted permanent magnets, polarised axially and oriented alternatively instead of respecting an Halbach configuration. This last possibility would produce an axial magnetic flux density closer to a pure sine as well as a stronger fundamental component than the conventional configuration, allowing to stronger verify the assumption 8 of the state-space model. The main dimensions and characteristics of the permanent magnets are listed in Table 4.1. These are chosen so as to obtain a bearing which remains small enough while having the highest remanent magnetisation B_r.

Back irons

As shown in Fig. 4.1, two back irons are attached to the rotor on both sides of the ferromagnetic yoke supporting the PMs. This assembly offers two main advantages. On the one hand, it allows to concentrate the magnetic flux density in the material and thus

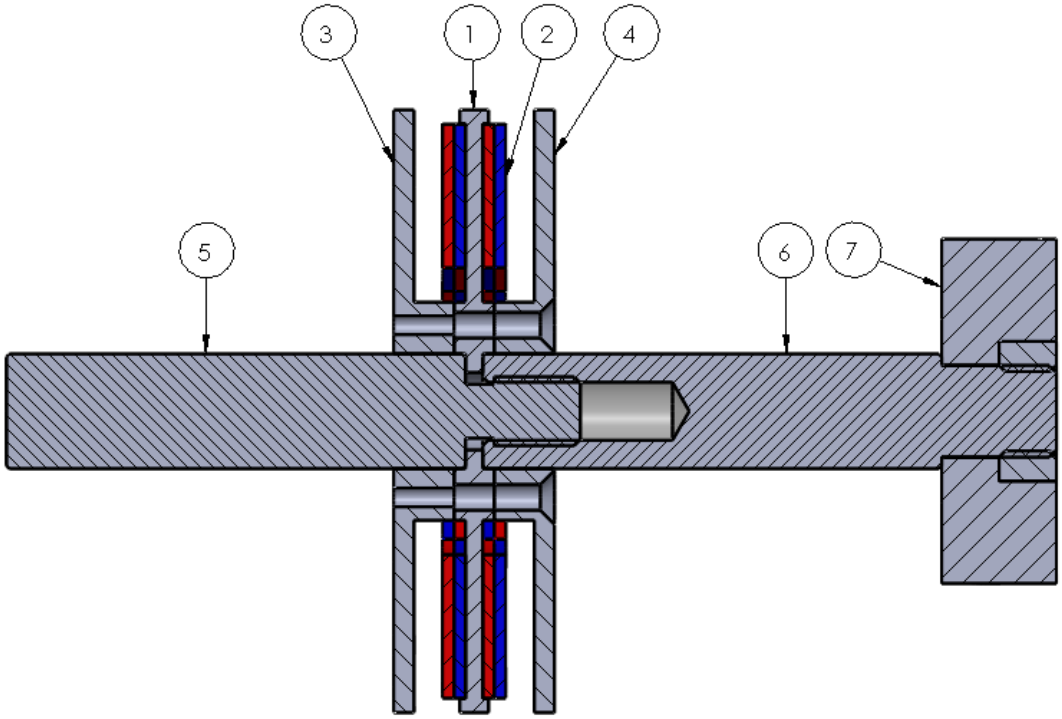

Fig. 4.2: Cross-sectional view of the rotor.

to create a preferential path that goes through the windings. On the other hand, it can be remarked that the permanent magnets arrangements are attached to the rotor and are thus in relative motion with respect to all the conductive parts located at the stator. Hence, the back irons prevent the appearance of Eddy currents in these conductive parts, thus avoiding Joule losses which would lead to an increase of the temperature and an additional braking torque. Finally, the back irons prevent the appearance of detent efforts due to the presence of ferromagnetic parts at the stator. The thickness of each back iron, shown in Fig. 4.3b, has to be determined carefully. Indeed, decreasing their thickness reduces the section crossed by the flux, leading to a higher magnetic flux density. It has thus a considerable impact on the magnetic saturation in the material. The minimal thickness allowing to avoid the saturation is determined through finite elements simulations in appendix C, yielding 3.5 [mm]. Obviously, each of both parts constituting the armature winding is located between the PMs arrangements and one back iron.

4.1.3 Stator

The stator of the thrust bearing only comprises the armature winding, separated into two identical parts that are, for the considered topology, connected in opposition. As mentioned above, two different types of winding have been investigated for the prototype: on the one hand, coils printed on a PCB, detailed hereinafter, and, on the other hand, more classical wire-wound coils. As a result of a lack of time, this second type of winding could not have been tested. The interested reader will find additional information about the development of the wire-wound winding in appendix I.

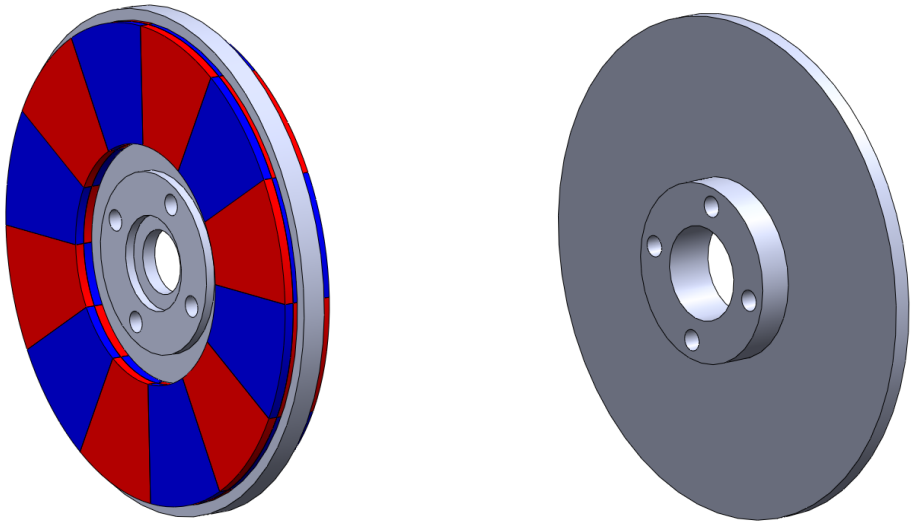

(a) Both permanent magnets arrangements.

(b) One ferromagnetic part.

Fig. 4.3: Rotor ferromagnetics parts with the PMs.

Table 4.1: Main characteristics of the PMs.

Parameter	**Value**
Inner radius R_i [mm]	25
Outer radius R_e [mm]	50
Thickness [mm]	4
Angular opening [rad]	$\pi/6$
Remanent magnetisation B_r [T]	1.28 (N42)
Mass [g]	14.65
Material	NdFeB

Interest

Printed circuit board (PCB) windings have focused much research efforts for the past fifty years [25]. This interest comes from the fact that this technique allows to explore new and more complex shapes for the loops and then new topologies for motors or magnetic bearings, with potentially increased performances. Indeed, PCB windings offer the main advantage of the flexibility. In this way, the tracks can take shapes that are not possible with wire-wound loops. Besides, the width of the tracks and then the section can change all along a loop which allows to better fill the space and then to increase the fill factor $\eta_{f,l}$ in one copper layer. It enables to reduce the resistance as the section increases [27]. The second main advantage is the facility to design PCBs, thanks to the powerful tools that are available, and to manufacture them, as PCB prices have fairly well declined in the last few years for most common board and copper thicknesses. Finally, as will be shown hereinafter, PCB allows to easily interlock the phases or the loops.

However, the PCB windings also present several drawbacks. Although they allow to increase the fill factor $\eta_{f,l}$ in the different copper layers of the PCB compared with wire-wound windings, these copper layers are separated by core and prepregs leading to an interlayer fill factor $\eta_{f,i}$. This factor is better for the wire-wound version as the electrical insulation of the wire is very thin compared with the wire diameter. Nevertheless, as the wire presents circular cross-section, there is also space lost due to the stack.

Technology

As explained in the previous section, the interlayer fill factor should be as large as possible to reach high performance. Besides, it allows to decrease the thickness of the complete winding and thus to have a smaller air gap for the same axial stroke. To this end, the different combinations of number of layers as well as the board and copper layer thicknesses available for manufacturing at *Eurocircuits* are analysed and only these providing the highest fill factor are reported in Table 4.2. Only even number of layers are retained due to construction reasons, as will be explained in section 4.1.3. It can be observed that the two layers board with a 105 [μm] copper layer presents the highest interlayer fill factor. Hence, this particular combination is chosen for the PCBs windings for the experimental EDTB. As there is only two layers, several boards will be stacked one on top of the other so that it increases the total number $N_{l,t}$ of loops per phase.

Table 4.2: PCB dimensions available at *Eurocircuits*.

Number of layers	**Board thickness [μm]**	**Copper thickness [μm]**	$\eta_{f,i}$ [$-$]
2	410	105	0.51
4	492	35	0.28
4	706	70	0.39
6	662	35	0.31
6	1209	70	0.34
8	1084	35	0.26

The maximal thickness of the armature windings is about 2 [mm]. Therefore, it is possible to stack five boards to create each subassembly of the armature. The main properties linked to the chosen PCB technology are reported in Table 4.3. As shown in Fig. 4.4, the minimal drill diameter is the smallest final hole and the minimal via diameter is the sum of PHD and 2×OAR, yielding 550 [μm].

Type of windings

For the PCB version of armature, it is decided to head for a wave winding. Indeed, this type of winding is more convenient given that the topology implemented in the prototype requires to connect the p lobes of a same phase in series. A lobe is defined as a part of the winding which corresponds to a pole pair. Each phase winding is thus composed of p identical lobes. Besides, the difference between the inner and outer radii R_i and R_e of the PMs arrangements being rather large, there is enough space and thus no need to choose spirally shaped windings [26]. Finally, taking advantage of the possibilities offered by the PCBs, overlapping windings are considered in order to have an integral pitch.

Table 4.3: PCB properties for the particular technology.

Property	**Value [μm]**
Minimal track width	250
Minimal insulation distance	300
Minimal annular ring (OAR)	125
Smallest final hole	200
Production hole diameter (PHD)	300

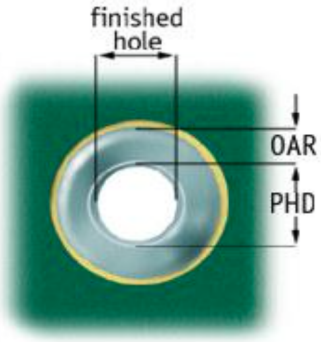

Fig. 4.4: Minimum annular ring and smallest final hole [28].

Wave windings

As stated previously, the thrust bearing conceived as a part of this master's thesis presents six pole pairs and three phases. The phase winding must then be composed of six poles of 30°, each covering completely one PMs pole (integral pitch). The radial dimensions are the same as those of the permanent magnets, namely the inner and outer radii, R_i and R_e, are respectively 25 and 50 [mm]. As stated in section 2.1, the three phases are identical and evenly distributed around the spin axis, following the expression (2.1).

In this section, the figures only represent the neutral axis of the tracks as the purpose is to analyse different shapes and connections. Besides, regardless of the type of wave winding, as all the lobes of a phase are identical, only the first one, which is located in the interval $[-\pi/p\,;\,\pi/p]$, has to be described. Moreover, this lobe being symmetrical with respect to the X axis, only the half of the lobe located in the interval $[0\,;\,\pi/p]$ will actually be defined.

Radial winding

The radial phase winding is shown in Fig. 4.5a, with the forward conductors (solid lines) on the top layer and the return conductors (dashed lines) on the bottom layer. The connection between both layers is ensured through vias (represented by dots). The radial winding can be described through four points in polar coordinates $\{\xi, \psi\}$:

$$\begin{aligned} \{\xi_1, \psi_1\} &= \{R_i\,;\,\pi/p\} \\ \{\xi_2, \psi_2\} &= \{R_i\,;\,\pi/2p\} \\ \{\xi_3, \psi_3\} &= \{R_e\,;\,\pi/2p\} \\ \{\xi_4, \psi_4\} &= \{R_e\,;\,0\} \end{aligned} \tag{4.1}$$

This shape can be considered as the ideal one as each lobe of this winding fully covers the surface of a permanent magnet and the flux linked is then maximised. However, as the inner and outer sides of the winding are located on constant radii, it is not possible to place three phases without conflicts between the tracks.

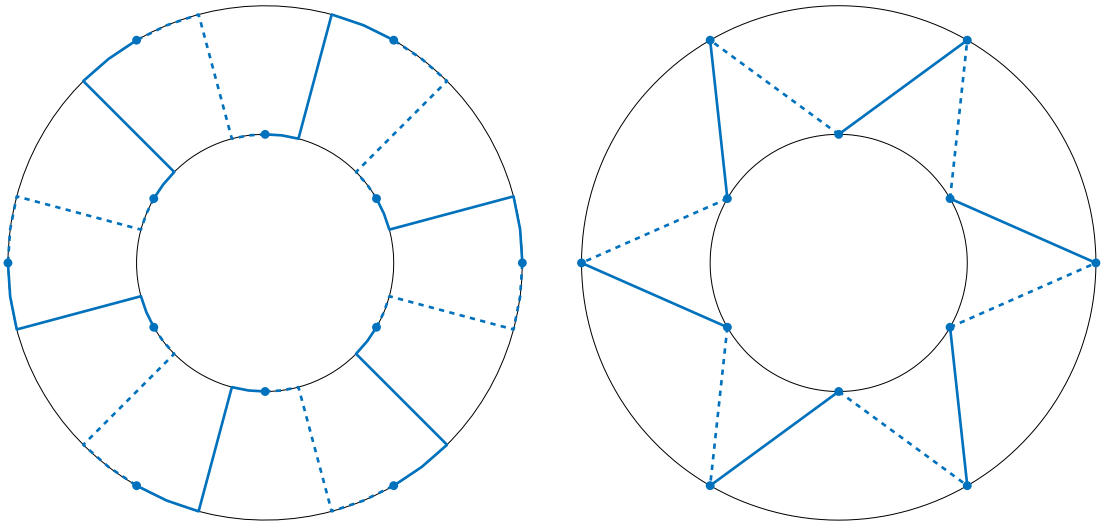

(a) Radial winding. (b) Helical winding.

Fig. 4.5: Two different types of wave windings: one phase of one loop. Forward conductors on top layer (solid lines), return conductors on bottom layer (dashed lines) and vias to connect the layers (dots).

Helical winding

In order to avoid this issue, the helical or one segment winding, as shown in Fig. 4.5b, is the simplest shape that can be considered. This winding can be described through two points in polar coordinates:

$$\begin{aligned} \{\xi_1, \psi_1\} &= \{R_i \,;\, \pi/p\} \\ \{\xi_2, \psi_2\} &= \{R_e \,;\, 0\} \end{aligned} \tag{4.2}$$

Although this shape allows to interlock the different phases without contact between them, it is not highly efficient. Indeed, the magnetic flux density due to the permanent magnets has, in the ideal case, two components. On the one hand, the axial component which has already been discussed and whose expression is given in (3.1). On the other hand, the azimuthal component which interacts with the current flowing in the winding, yielding the restoring axial force. Hence, based on Lorentz force law, only the radial parts of the segments yield a benefical effect: higher performances are reached if the loops present longer radial parts. The radial segments are then also called the active segments of the winding. This argument also supports the fact that the radial winding (Fig. 4.5a) is the ideal one.

Three segments winding

From the previous analyses, it seems interesting to find a shape with radial segments that can be interlocked. To this end, the three segments wave winding can be studied. Fig. 4.6a shows one single phase. It is divided into three segments among which the second one

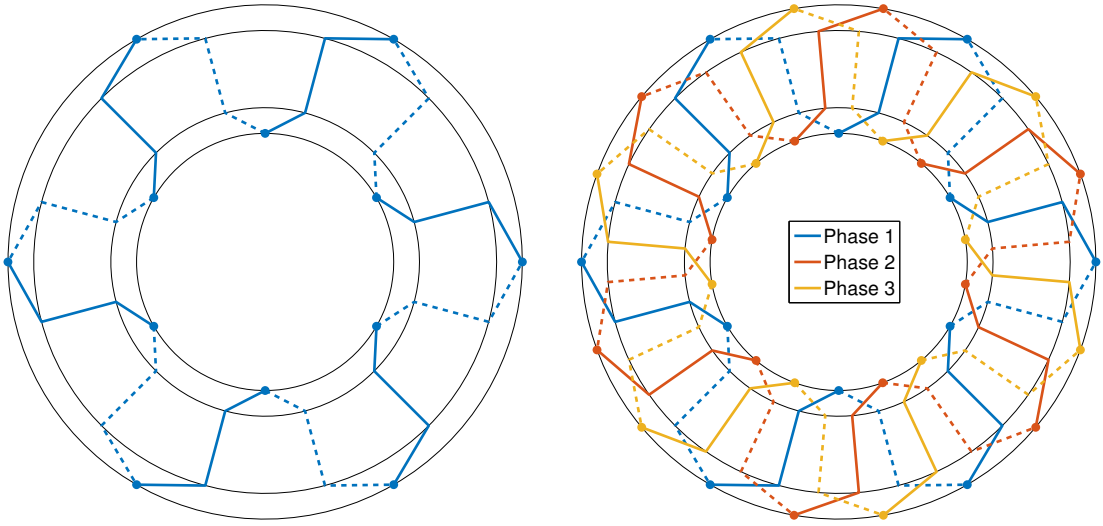

(a) One phase of one loop.

(b) Three phases of one loop.

Fig. 4.6: Three segments wave winding. Forward conductors on top layer (solid lines), return conductors on bottom layer (dashed lines) and vias to connect the layers (dots).

is purely radial and its length should therefore be maximised. Defining the radii R_{ii} and R_{ee} respectively as the inner and outer radius of the second segment, this winding can be described through four points in polar coordinates:

$$\begin{aligned} \{\xi_1, \psi_1\} &= \{R_i \,;\, \pi/p\} \\ \{\xi_2, \psi_2\} &= \{R_{ii} \,;\, \pi/2p\} \\ \{\xi_3, \psi_3\} &= \{R_{ee} \,;\, \pi/2p\} \\ \{\xi_4, \psi_4\} &= \{R_e \,;\, 0\} \end{aligned} \tag{4.3}$$

For the following figures, the value of the radii R_{ii} and R_{ee} are arbitrarily set to 30 and 45 [mm]. This choice will be discussed later. Furthermore, it is decided to keep this shape for the final PCB winding as it seems to represent a fair compromise to obtain rather fine performances while avoiding an optimisation on the shape.

Loops

As shown in Fig. 4.6b, the three phases constituting the armature winding of the EDTB leave much free space around the neutral axis of the track. This space can be filled by enlarging the tracks width which allows to decrease the resistance. However, considering a stack of five boards and a series connection between the same phase of the boards, the total number $N_{l,t}$ of loops per phase is only five. Besides, too large tracks could lead to unwanted Eddy currents. Therefore, the free space between the phases in a copper layer could be used to increase the number of loops. In this way, the phase loops are identical and evenly distributed in the free space, yielding a distributed winding. Considering N_l loops per copper layer, the angular position γ_l of the l-th loop with respect to the first one of one phase is given by:

$$\gamma_l = \frac{2\pi(l-1)}{pNN_l} = \gamma(l-1) \tag{4.4}$$

where $l = \{1, \ldots, N_l\}$. The number of loops is limited by the smaller radius R_i. Hereinafter, it is set to three for clarity purposes. Fig. 4.7a shows three phases, each constituted

of three loops but these loops are not yet connected together. This is thus equivalent to a winding composed of nine phases. A simple way to ensure the series connection of the different loops of one phase is to extend the tracks of the first lobe of the N_l loops of each phase. More precisely, the return conductor of the l-th loop is connected to the forward conductor of the $(l+1)$-th loop through a via located on a radius $R_o > R_e$, as shown in Fig. 4.7b. The detailed calculations of this radius R_o are available in appendix D. Moreover, the forward conductor of the first loop as well as the return conductor of the last loop of each phase are lengthened and represent both terminals of the coils. As there are three phases, each board has six terminals. The corresponding phase terminals of each consecutive board are connected in series to end up with only six final terminals for each part of the armature winding.

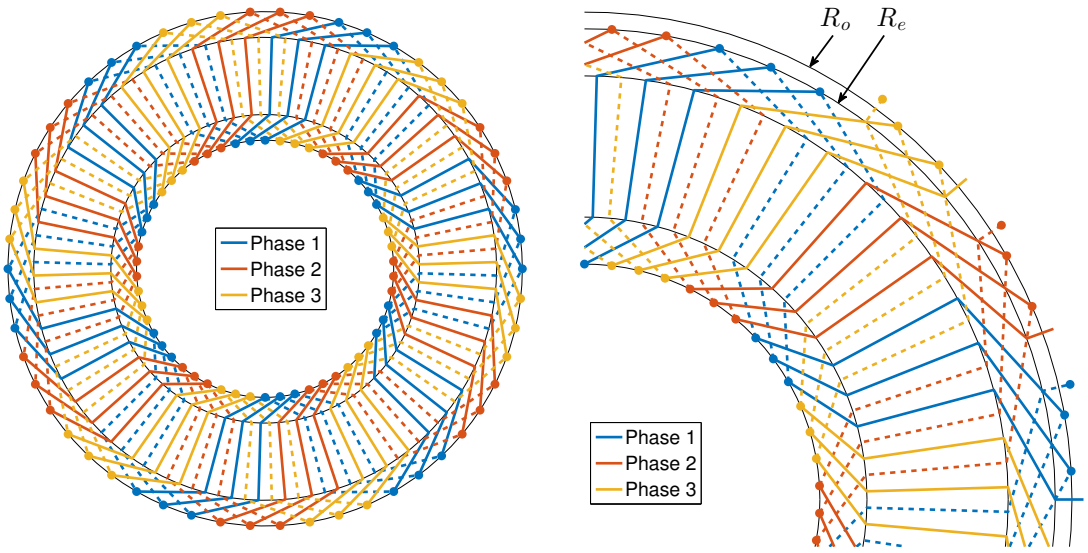

(a) Three phases of three loops.

(b) Three phase of three connected loops.

Fig. 4.7: Three segments wave winding. Forward conductors on top layer (solid lines), return conductors on bottom layer (dashed lines) and vias to connect the layers (dots).

Tracks

Fig. 4.7b shows the neutral axis of the different phases. Based on the PCB characteristics for the particular chosen technology, reported in Table 4.3, the width of the tracks all along the neutral axis of the different phases has to be determined. The neutral axis being constituted of straight lines, the tracks are composed of polygons around these lines. As the vias will be discussed in the next subsection, the only constraints here are the minimal track width and the minimal insulation distance. Taking a constant width for the tracks would lead to large free space between them, leading to a small layer fill factor $\eta_{f,l}$. Therefore, the track width is calculated so that the distance between each consecutive track remains constant and equal to the minimal insulation distance, as can be seen in Fig. 4.8. The detailed calculations are available in appendix E. Fig. 4.9 shows the top and bottom layers of the resulting PCB. In this way, the maximal layer fill factor $\eta_{f,l}$ is reached in each layer taking into account the limit of the PCB technology.

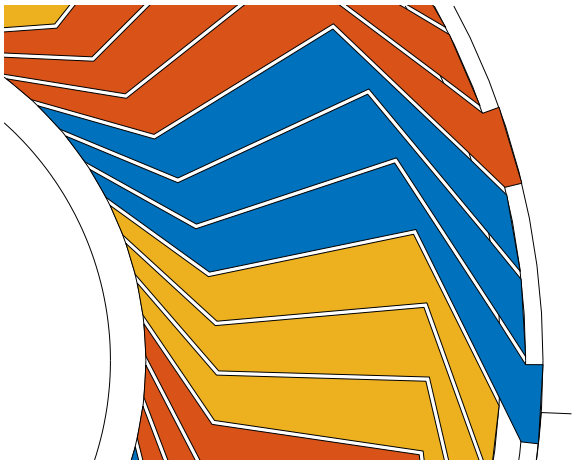

Fig. 4.8: Track width with constant insulation distance, zoom

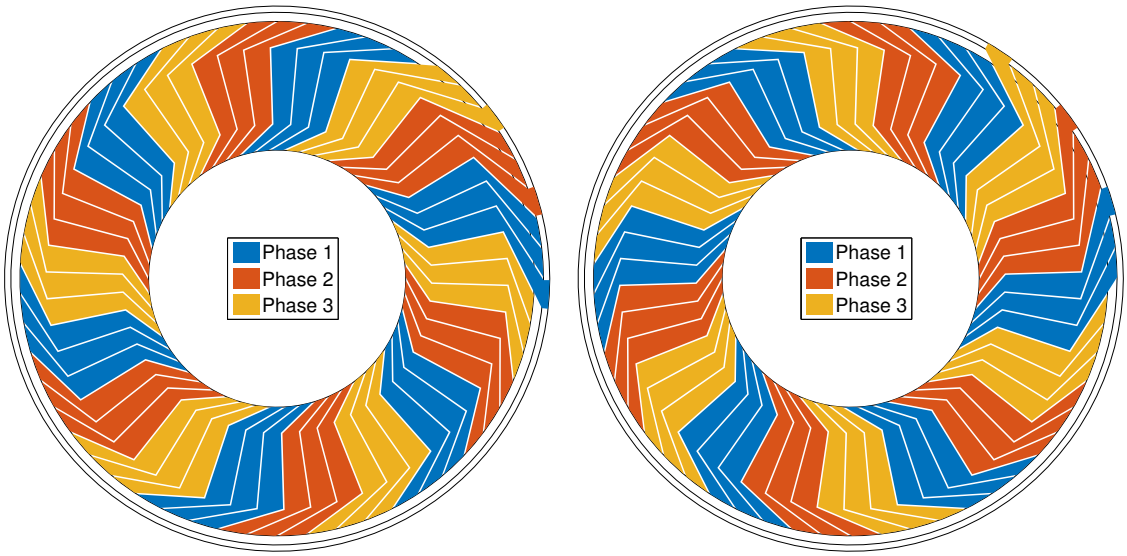

(a) Top layer.

(b) Bottom layer.

Fig. 4.9: Three segments wave winding: track width with constant insulation distance.

Vias

The top and bottom layers tracks being conceived, they have to be connected together so as to form the phases. To this end, vias have to be placed as represented by the dots in Fig. 4.7b. The first method that is considered for the placement of the vias is to put them in the center of the triangle resulting from the intersection between the projections of the tracks of both layers, as shown in Fig. 4.10a. The main drawback of this method is that these triangles are very small. Remembering that the smallest via diameter is 550 [μm], it is very difficult to place more than one via in each triangle. As the issue is the available space to place the vias, the second method that is considered consists in extending the tracks radially inwards and outwards for the inner and outer vias, respectively. Fig. 4.10b shows the resulting tracks and vias: it can be remarked that there are, respectively, two times and

five times more inner and outer vias than with the first method. The distance between the outer diameter of each vias has to be larger than the minimal insulation distance. Based on this, the maximal number of vias is calculated and they are evenly distributed in the provided space.

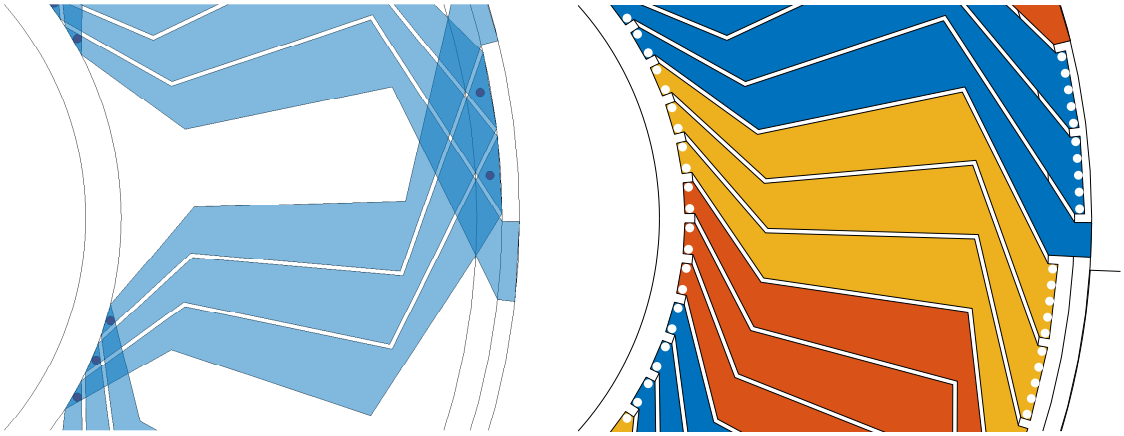

(a) First method (b) Second method

Fig. 4.10: Three segments wave winding: vias locations (white dots).

Board shape

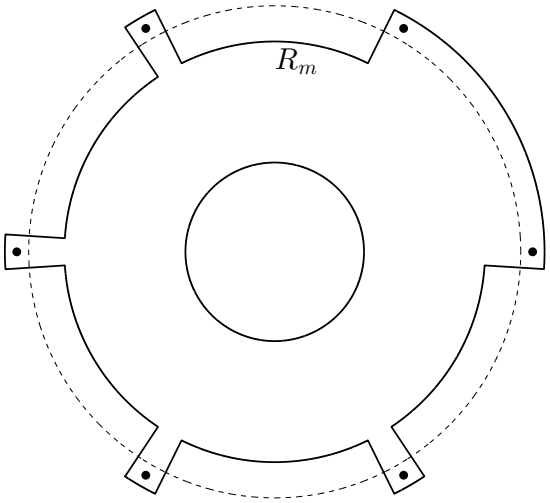

Fig. 4.11: Board shape. External limits (solid lines), clamping diameter (dashed line) and screw holes (dots)

Fig. 4.7b shows that terminals (the output connections) of each phase are located in the first 60° of the PCB. To connect the same phase together between the different boards, the basic way would be to stack the boards with the same orientation so that the output pads

are one on top of each other. However, this solution does not ensure a perfect connection between the consecutive PCBs and requires a specific placement of the pads for a series connexion. Therefore, it is decided to stack each board shifted by a pole pair pitch, i.e. $2\pi/p = 60°$, with respect to the previous one, meaning that the phases are correctly aligned between the boards. Fig. 4.11 shows the external PCB shape. In order to connect the different boards, wires are tied between the pads of the consecutive boards. Moreover, the terminals have to be located between the radius R_m and the clamping diameter (dashed line). Screw holes, represented as dots in the figure, allows to fix the consecutive boards, with an angular shift of 60°, to the stator. Fig. 4.12 shows an exploded view of a stack composed of five PCBs.

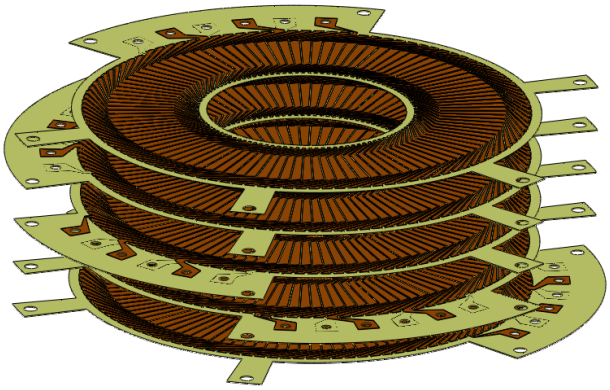

Fig. 4.12: Exploded view of a stack composed of five PCBs shifted by 60° with respect to the previous PCB.

Terminals

The careful reader should have remarked, in Fig. 4.9, that both terminals of each phase are not on the same layer. Besides, both terminals of the second phase (in orange) have the same location as one terminal of the other phases but on a different layer. The final terminals have to be placed between the two first screw holes. It is decided to keep the terminals of each phase together and to distribute them evenly in the allocated space. Besides, a large via is positioned at the end of the tracks so that all the terminals are available on both sides of the board, allowing an easy connection between the different boards. The resulting PCB is shown in Fig. 4.13.

Final version

As mentioned above, the final version of the PCB is constituted of a three segments wave winding. Starting from the version shown in Fig. 4.13, there are three parameters that haven been set arbitrarily, namely the inner and outer radii of the second segment as well as the number N_l of loops. The two first parameters are kept to 30 and 45 [mm] as these values allow to have a long active segment while preventing too thin tracks in the other segments. However, for the final version, each phase is constituted of six loops ($N_l = 6$). Indeed, knowing that the minimal insulation distance is already imposed between the tracks, it represents the largest N_l possible while respecting the minimal track width as well as the minimal via diameter.

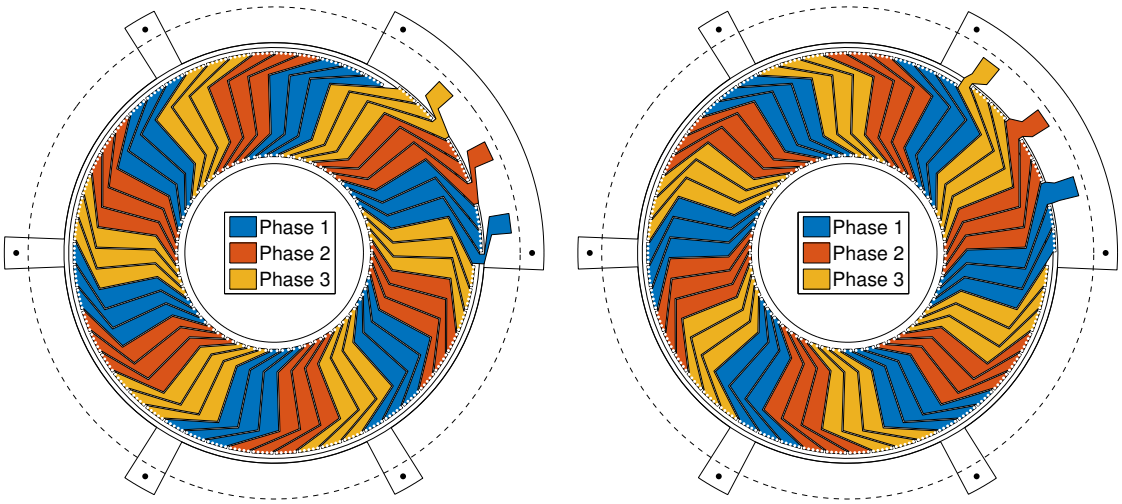

(a) Top layer.

(b) Bottom layer.

Fig. 4.13: Three segments wave winding: tracks, vias and terminals placed.

A MATLAB code was developed to compute all the points constituting the PCB, allowing to test different combinations and to produce the corresponding figures, as those shown hereinabove. This code also creates a script file (`.scr`) which is readable by the software EAGLE, enabling to generate automatically the board file (`.brd`) that is required by the manufacturers as *Eurocircuits*. The interested reader will find additional information about the automatic generation of boards in appendix G. Fig. 4.14 shows one PCB after manufacturing.

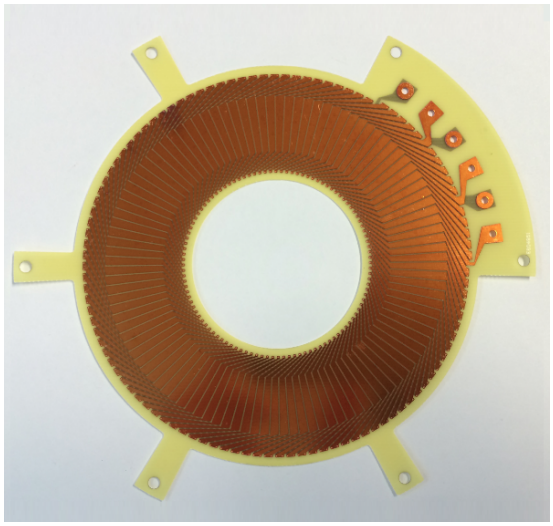

Fig. 4.14: Manufactured PCB.

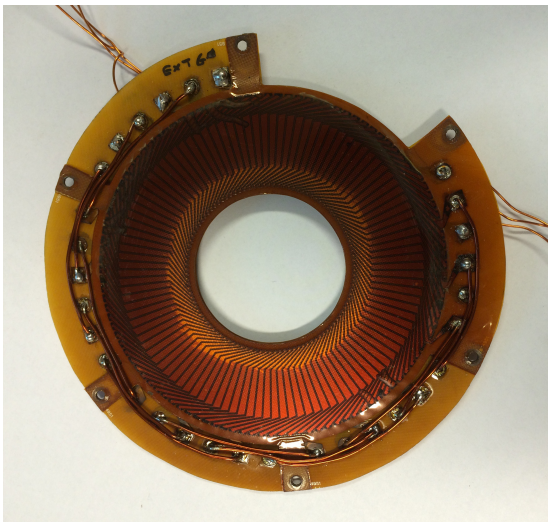

Fig. 4.15: Stack with the five boards connected.

The armature winding is composed of two parts. Each of them has to present a thickness of roughly 2 [mm] to ensure a maximal axial stroke of 1.5 [mm] in each direction. As the tolerances given by *Eurocircuits* are rather large, it is decided to stack five boards for each part of the armature winding. To minimise the axial lost space, the PCB are

manufactured without solder mask whose thickness is rather important. Therefore, in order to avoid unwanted connections between the tracks of the stacked boards, a thin insulation of 50 [μm] is inserted between them. This insulation must be taken into account in the interlayer fill factor, leading to 46% instead of 51%. The procedure followed to assemble each stack constituted of fives boards and six insulations is detailed in appendix F. The resulting stack is shown in Fig 4.15, with the six output wires, three on each side.

Improvements

Further improvements can be provided to the final version of the PCB winding. First, the proposed shape of the wave winding, namely the three segments, is not optimal. On the one hand, the inner and outer radii of the second segment, R_{ii} and R_{ee}, were selected in a more or less arbitrary way. This choice could have been made based on several simulations or even an optimisation. On the other hand, an optimisation algorithm, such as the genetic one, could be used to find another shape with, for example, more segments, or even composed of more complex functions than just linear segments to maximise the performances of the EDTB.

Second, for construction reasons, copper tracks should be added in the parts that serve to screw the stacks to the stator. Indeed, as the interlayer fill factor is near to 50%, the difference in thickness between the center of the PCB, where there are copper tracks, and these parts is important. Hence, it is difficult to maintain all these latter in the same plane when the stack of boards is compressed during the assembly, leading to a misalignment between the revolution axes of the PCB and of the rotor. Some lobes of the winding are thus located on a smaller or larger z. This results respectively in an larger or lower flux linked by each of both parts constituting the armature winding and coul lead to a unbalance between these parts.

Third, as discussed earlier, the PCB technology used plays an important role in the performances of the EDTB. In this way, choosing another manufacturer that offers higher interlayer fill factor would enhance the performance. Besides, reducing the minimal insulation distance between the tracks would also help as it would increase the layer fill factor. Flexible PCB could represent a solution: the insulation distance and the fill factor can reach respectively 100 [μm] and 50% [27]. However, they are still expensive and the flexible characteristic itself is not interesting in axial flux magnetic bearings as the windings stay in one plane. Finally, the global fill factor, which is defined as the product of both layer and interlayer fill factors, will increase over years as the PCB technologies will improve.

4.2 Test bench

This section describes the test bench designed to implement the prototype presented hereinabove. Fig. 4.16 shows a cross-sectional overview of this test bench. The purpose is to analyse the axial levitation provided by the electrodynamic thrust bearing under test. To this end, the rotor must also be guided radially through a system that should have an impact as low as possible on the axial levitation. For the test bench, it is ensured by means of two air bearings, located on both sides of the EDTB. As mentioned above, the armature winding constitutes the stator of the EDTB and is thus fixed to the test bench, both stacks of PCBs being located between the PMs arrangements and the back irons. As

shown in Fig. 4.16, the test bench consists of the eight following components:

a) the thrust bearing itself (1)

b) two air bearings (2);

c) two lids (3) on which the air bearings (2) are fixed;

d) the protective shield (6);

e) the displacement measurement sensor (4);

f) a drive system (7);

g) a loading system (5).

h) the mechanical stops.

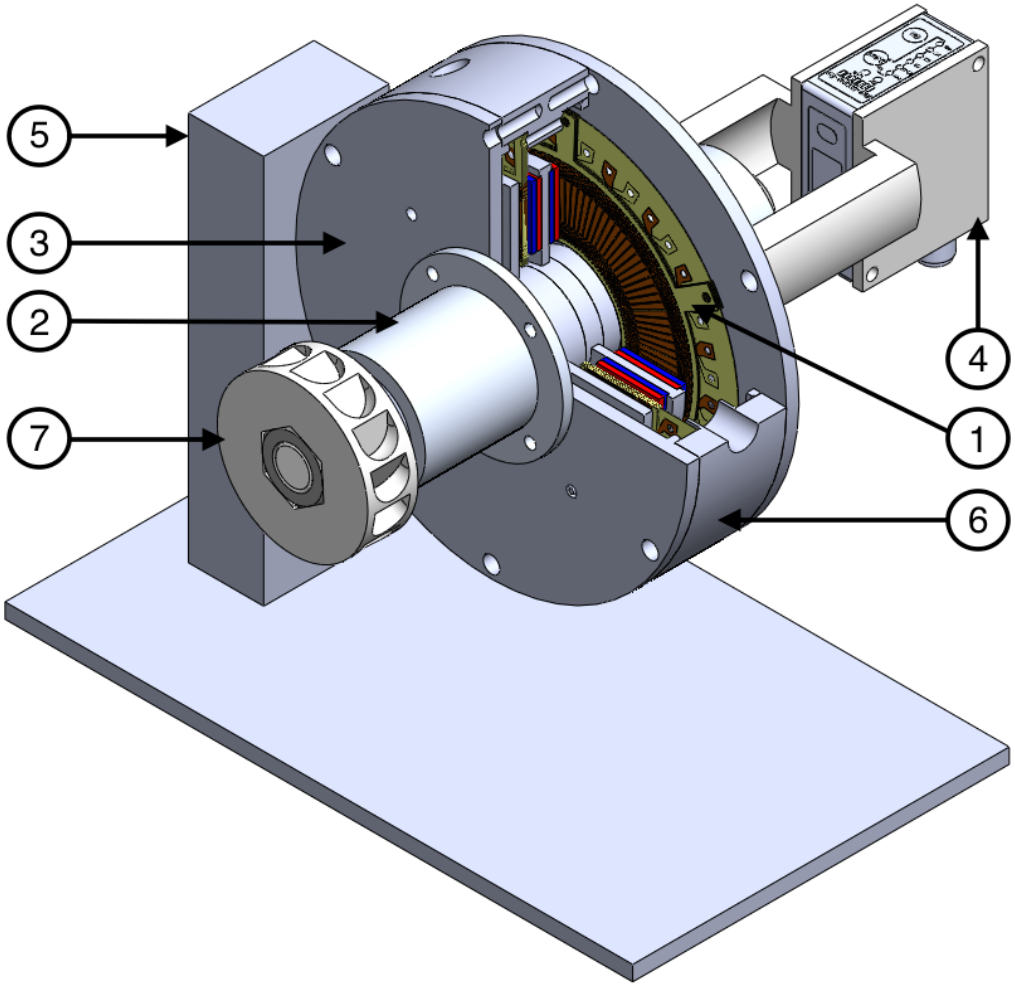

Fig. 4.16: Test bench of the EDTB.

The drive system allows to spin the rotor around its rotation axis. Three different means are investigated: a compressed air turbine, shown in the figure, an electrical motor and a pneumatic motor. The sensor is employed to measure the axial displacement z of the rotor from its nominal position. Lastly, the loading system allows to apply a constant and known axial load to the system to study its quasi-static behaviour. These elements are detailed hereinafter and their drawings are available in appendix L.

4.2.1 Air bearings

As stated above, the radial guiding is ensured by means of two air bearings placed on both sides of the EDTB. They allow to support the radial load due to the weight of the rotor while having an impact as low as possible on the performances of the thrust bearing. Each air bearing is constituted of two parts: the air bushing, produced by *New Way air bearings*, and the sleeve, shown respectively in Figs. 4.17a and 4.17b. The former is inserted into the latter and compressed air is injected through the hole located on the top. The air evenly distributes as a thin film between the shaft and the inner surface of the air bushing, allowing to sustain up to 133 [N] when supplied with 4 bars. The load capability strongly depends on the surface condition as well as the roughness of the shaft.

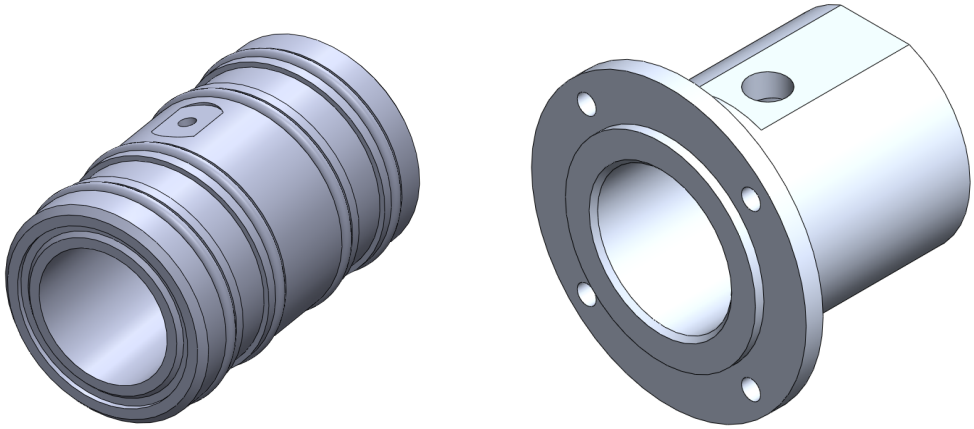

(a) Air bushing. (b) Sleeve.

Fig. 4.17: Air bearings.

4.2.2 Protective shield

The protective shield, shown in Fig. 4.18, achieves four main purposes. First, as its name implies, it serves as a protective shield in case of projection of some parts, such as the permanent magnets, due to a high spin speed. Second, both parts constituting the armature winding are fixed on it. Third, the three holes located on the perimeter and spaced by 120° enable the observation of the permanent magnets arrangements and thus of the rotor during the functioning as well as the passage of the wires of the armature winding. Finally, the protective shield also supports the complete test bench through the fourth hole, as will be explained in section 4.2.5.

4.2.3 Sensors

Two sensors are required to analyse the rotor axial dynamics as well as its quasi-static behaviour. On the one hand, a distance sensor allows to measure the axial displacement z of the rotor from its nominal position. It is thus fixed to the stator and directed towards the end of one shaft. The reference `OD2-P30W04I0` from *Sick* is selected as it is already available and meets the required specifications (see Table 4.4). Fig. 4.19 shows the sensor mounted on its support. On the other hand, an optical tachometer allows to measure the spin speed of the rotor. This sensor simply counts the number of passage of a mark, added on an external surface of the rotor, per unit of time. The rotor spin speed can also be calculated through the frequency of the back EMF.

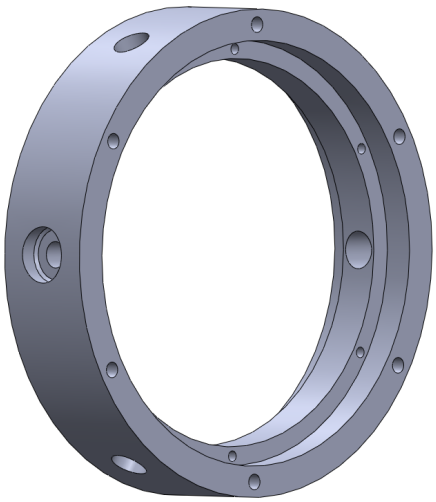

Fig. 4.18: Protective shield.

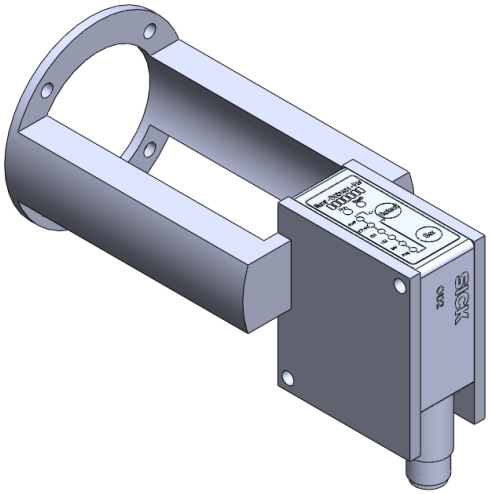

Fig. 4.19: Displacement measurement sensor in its support.

Table 4.4: Characteristics of the sensor `OD2-P30W04I0` from *Sick*.

Parameter	**Value**
Measurement range [mm]	26 to 34
Resolution [μm]	2
Measurement frequency [kHz]	2

4.2.4 Drive system

The axial recentering force exerted by the thrust bearing on the rotor only appears for non-zero spin speed and increases with the speed. Therefore, three different drive systems are investigated to spin the rotor as fast as possible while having an effect as low as possible and known on the axial degree of freedom.

Turbine

The first drive system that is implemented is a compressed air turbine whose main part is shown in Fig. 4.20. The principle is extremely simple: the turbine consists of a solid cylinder with notches acting like blades. In this way, injecting compressed air in these notches allows to spin the rotor. It also exerts radial and axial forces and thus has an impact on the axial movement. Hence, once the targeted speed is reached, compressed air is no more injected and the rotor is expected to go on thanks to its inertia and the low load torque. The displacements and constraints induced by the rotation are analysed through finite element methods in appendix J, allowing to validate that the turbine can withstand a spin speed of 30 000 [rpm]. As will be explained in section 4.4.1, this speed is about 50% larger than the unstability spin peed. In pratice, this methods allows to reach at least 4500 [rpm] when the armature winding is not present.

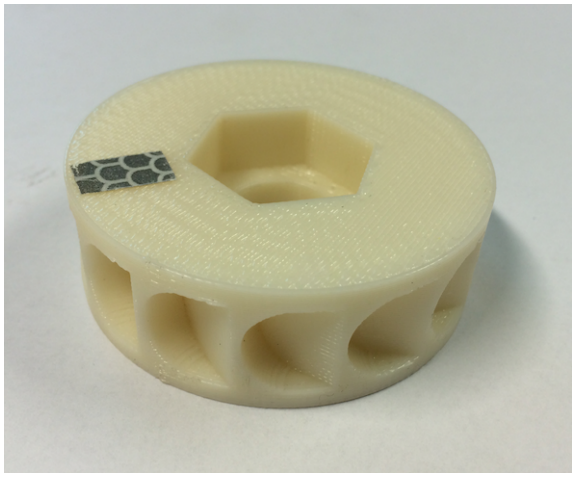

Fig. 4.20: Compressed air turbine.

Electrical motor

The second drive system that is investigated is an electrical motor, namely a *Maxon* RE35. It offers the advantage that the spin speed can be easily maintained to a constant value, which is convenient for the measurements. Without load, this DC motor can reach up to 3140 [rpm]. However, the electrical motor has to be coupled to the rotor. Here, it is decided to use a flexible bellows coupling. In this way, the axial degree of freedom is not totally constrained. Knowing the stiffness of the coupling, the dynamics of the complete system, constituted of two springs in parallel, can be analysed, as explained in appendix K. As shown in Fig. 4.21, the motor is maintained in a chosen position with a stand.

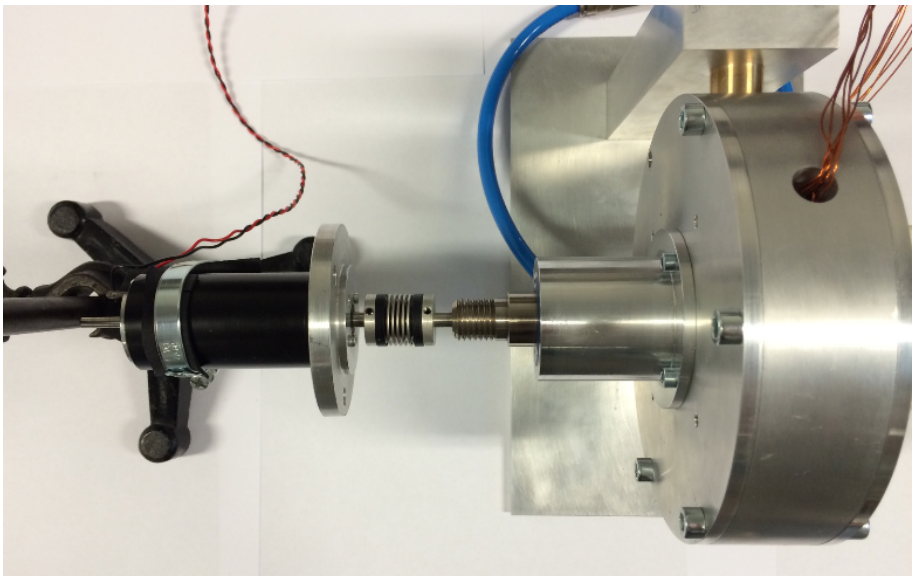

Fig. 4.21: Drive system: electrical motor attached to the shaft through a flexible bellows coupling.

Pneumatic motor

The third drive system is based on the pneumatic motor of a grinder. It is coupled to the rotor through the bellows coupling described above and is attached directly to the test bench with a support, as shown in Fig. 4.22. Without load, this motor can reach up to 20 000 [rpm].

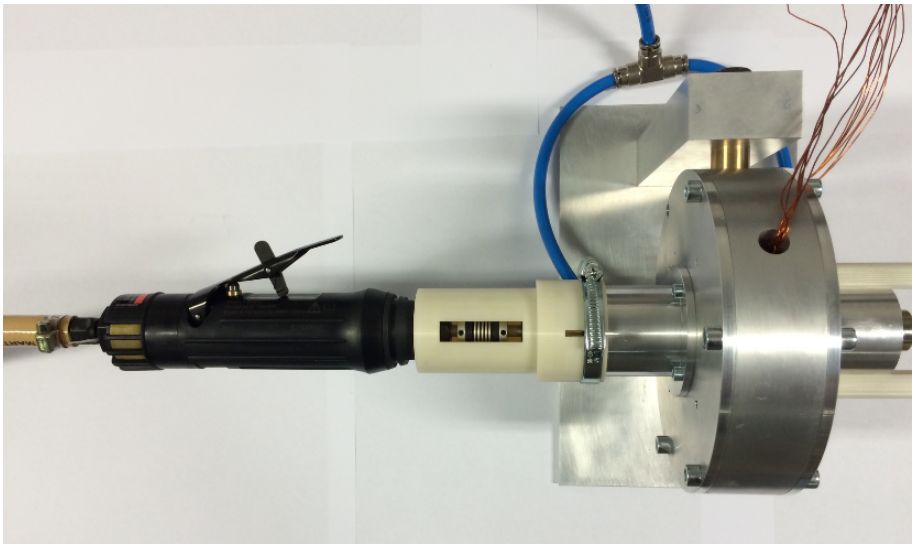

Fig. 4.22: Drive system: pneumatic motor attached to the shaft through a flexible bellows coupling.

4.2.5 Loading system

The loading system allows to exert a constant and known axial force F_e on the rotor. In this way, the behaviour of the EDTB in quasi-static conditions can be studied. For the test bench, the implementation is extremely simple. As can be seen in Fig. 4.16, the stator is attached to a mounting bracket which is itself fixed to a horizontal support. Fig. 4.23a shows a cross-sectional view of the fixation between the mounting bracket (1) and the protective shield (3), through a tube (2). The assembly formed by these three parts is fastened by means of a screw as the protective shield comprises a tap hole. Hence, to apply an axial load, the stator must simply be fixed in an angular position so that the rotor spin axis is no more parallel to the horizontal support. Defining Λ as the angle between the rotor spin axis and the horizontal support, the axial load F_e is yielded by:

$$F_e = Mg\sin(\Lambda), \tag{4.5}$$

where g is the gravitational acceleration and M the rotor mass. Hence, there is no axial load when the angle Λ is zero, as shown in Fig. 4.23b. By contrast, the axial load is maximal and equal to the rotor weight Mg when the angle Λ is 90°, as shown in Fig. 4.23d. Fig. 4.23c shows the test bench when the angle Λ is roughly equal to 45°.

4.2.6 Mechanical stops

Four mechanical stops are placed on each lid of the test bench. They are essential as the thrust bearing cannot bring the rotor back in its nominal position without the latter rotating. Besides, in case of unstability of the bearing, the back irons strike the stops which allows to prevent the rotor from damaging the windings.

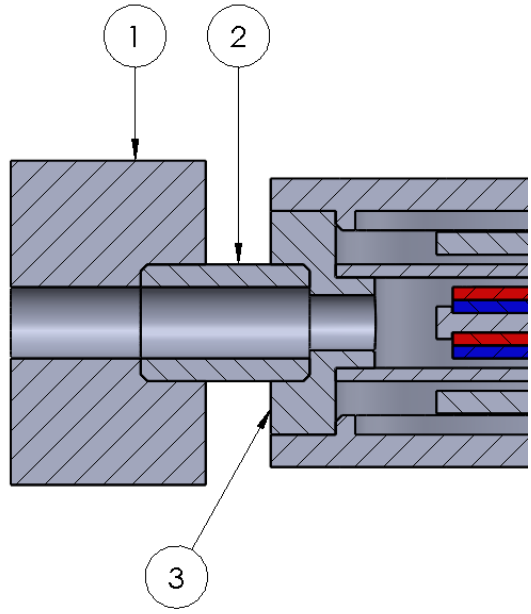

(a) Principle.

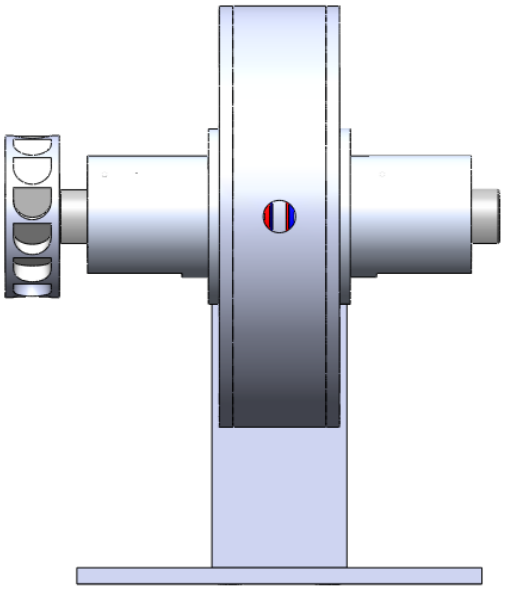

(b) Example 1: $\Lambda = 0°$.

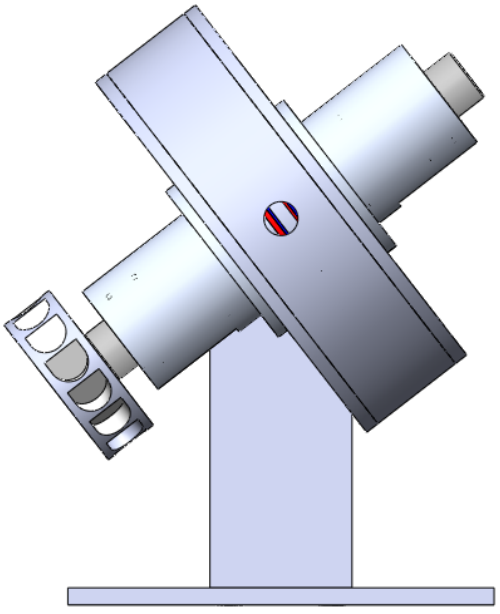

(c) Example 2: $\Lambda = 45°$.

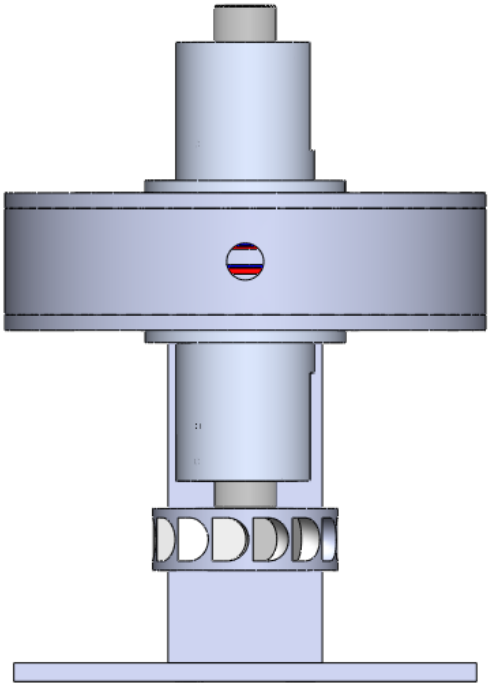

(d) Example 3: $\Lambda = 90°$.

Fig. 4.23: Loading system: principle and examples.

4.3 Model parameters identification

As stated in section 3.6.4, the state-space model allows to describe the complete axial dynamics of the electrodynamic thrust bearing coupled with an one degree of freedom rotor through eight parameters. Among these, the number p of pole pairs and the number N of phases are already known as being six and three respectively. Furthermore, the back irons located on the rotor prevent the interactions between the PMs arrangements and ferromagnetic parts that would be attached to the stator, meaning that the detent stiffness K_d is equal to zero. The rotor mass M is 1.55 [kg] and the damping factor C is null. The determination of the three remaining parameters, namely the phase resistance R, the cyclic indutance L_c and the coefficient K_Φ is detailed hereinafter.

4.3.1 Coefficient K_Φ

Simulation

As explained in section 3.6.4, the coefficient K_Φ can be determined through finite element methods by evaluating, for an axial displacement z, the flux linked by a phase winding in an angular position maximising this flux linkage and in quasi-static conditions at zero spin speed, i.e. $\dot{z} = 0$ and $\omega = 0$. Fig. 4.24 shows the evolution of this flux for axial displacements ranging from 0 to 0.5 [mm]. As expected, the flux is null when the axial displacement is zero. The coefficient K_Φ is identified by calculating the slope of the linear regression passing through these points, yielding 3.385 [Wb/m].

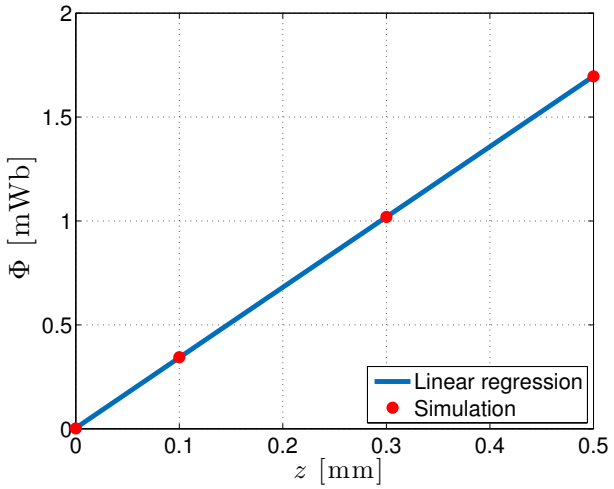

Fig. 4.24: COMSOL simulation: evolution of the flux Φ linked by a single phase with the axial displacement z.

Experimental

The coefficient K_Φ can also be identified experimentally on the test bench by measuring, with an oscilloscope, the voltage u_{emf} induced in one open circuit phase winding. Indeed, differentiating the expression (3.17) of the flux linked by the k-th phase winding with respect to the time yields:

$$u_{emf,k}(t) = -\frac{d\Phi_k}{dt} = zK_\Phi p\omega \sin(p(\omega t + \alpha_k)) - \dot{z}K_\phi \cos(p(\omega t + \alpha_k)) \tag{4.6}$$

where α_k takes into account the phase shift due to the initial position of rotor with respect to the k-th phase winding and the spin speed is assumed to be constant. Hence, considering quasi-static conditions, i.e. $\dot{z} = 0$, and thus a fixed axial displacement z, the measurements of the induced voltage at constant spin speed can be fitted with the following relation:

$$u_{emf,k}(t) = zK_\Phi p\omega \sin(p(\omega t + \alpha_k)). \tag{4.7}$$

The rotor is driven by means of the electrical motor to maintain a fixed spin speed which can be determined accurately through the pulsation of the induced voltage and the number p of pole pairs. The amplitude of the flux can be retrieved from the amplitude of the induced voltage by dividing by $p\omega$, allowing to compare the measurements performed at different spin speeds.

Fig. 4.25 shows the evolution of the flux amplitude in the first phase winding with the axial displacement for four spin speeds: 380, 480, 1000 and 1430 [rpm]. The stars represent the measurements while the solid lines are linear regressions. The root of these straight lines allows to determine experimentally the equilibrium position. It can be remarked that these regressions are very close to each other. Besides, the linearity of the flux in z is fairly well respected. The coefficient K_Φ is again identified through the slope of these regressions, yielding respectively 3.170, 3.268, 3.297 and 3.242 [Wb/m]. Compared with the value determined through simulations, the maximal error is about 7%, allowing to validate them. Hereinafter, the coefficient K_Φ is taken as being equal to the mean of the four previous values, yielding 3.244 [Wb/m].

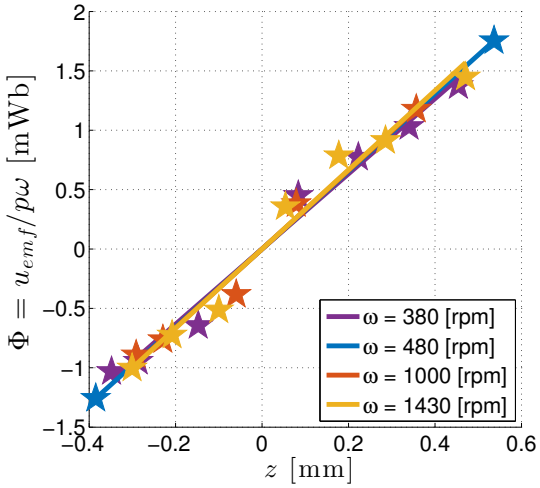

Fig. 4.25: Experimental identification of the coefficient K_Φ: evolution of the flux Φ linked by a single phase with the axial displacement z.

Fig. 4.26 shows the voltage u_{emf} induced for an axial displacement $z = 0.2$ [mm] and a spin speed $\omega = 1333$ [rpm]. Circles represent the measurements and the solid line is the theoritical curve (4.7), based on the coefficient K_Φ identified above. As expected, both curves are close, validating the coefficient K_Φ and the expression of the flux (3.17).

4.3.2 Cyclic inductance L_c

The experimental identification of the cyclic inductance L_c is performed through the relation (3.39). In the particular case of the prototype, namely three phases ($N = 3$), this

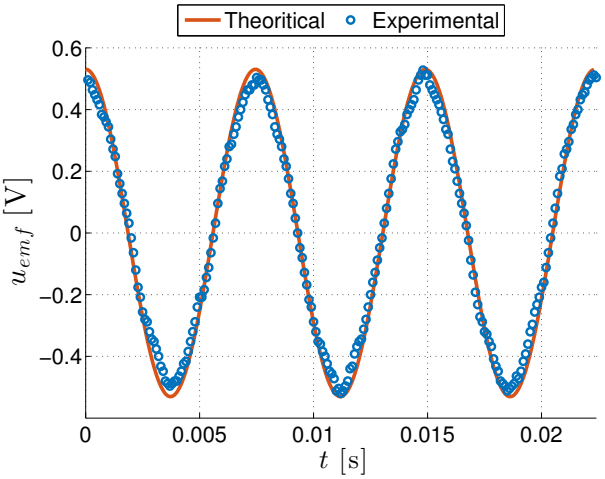

Fig. 4.26: Experimental identification of the coefficient K_Φ: induced voltage $u_{emf}(t)$ for an axial displacement $z = 0.2$ [mm] and a spin speed $\omega = 1333$ [rpm].

expression becomes:

$$L_c = L_{11} - \frac{L_{12}}{2} - \frac{L_{13}}{2} \tag{4.8}$$

The self inductance L_{11} can be measured directly on the test bench with an RLC-meter. By contrast, the mutual inductance L_{1k} is identified by measuring the inductance of both phases 1 and k connected in series. In this way, keeping in mind that the three phases are expected to present identical electrical properties, the measured inductance $L_{s,1k}$ is:

$$L_{s,1k} = 2(L_{11} + L_{1k}) \tag{4.9}$$

As the self inductance is already known, the mutual inductance L_{1k} can be easily calculated. The self inductance of the three phases and the mutual inductances between them are all measured in order to verify whether the system is well-balanced. The results are reported in Table 4.5. The decrease in the inductances with the increasing frequency is due to Eddy currents induced in the ferromagnetic parts. As expected, for each frequency, the three self inductances are close as well as the three mutual ones. The cyclic inductance is calculated using the mean of the three self and mutual inductances. It yields respectively 979 and 536 [μH] for 120 [Hz] and 1 [kHz]. These frequencies correspond to spin speeds equal to 1200 and 10 000 [rpm].

4.3.3 Phase resistance R

Theoritical

The winding phase resistance R is calculated using Pouillet's law:

$$R = \rho_c \int_0^L \frac{dx}{S(x)}, \tag{4.10}$$

where ρ_c is the copper electrical resistivity, equal to 1.68×10^{-8} [Ωm] at 25°. The detailed calculations are available in appendix H. Taking into account the tracks, the wires between the boards and the wires between both parts of the armature winding leads to a 5.32 [Ω].

Table 4.5: Inductance measurements [μH].

$\mathbf{L_{11}}$	**Phase 1**	**Phase 2**	**Phase 3**
120 [Hz]	648	650	650
1 [kHz]	419.5	417.4	422
$\mathbf{L_{s,1k}}$	**Phase 1-2**	**Phase 1-3**	**Phase 2-3**
120 [Hz]	1954	1960	1961
1 [kHz]	1070	1069	1073
$\mathbf{L_{1k}}$	**Phase 1-2**	**Phase 1-3**	**Phase 2-3**
120 [Hz]	329	330	330.5
1 [kHz]	115.5	117.1	114.5

Experimental

The phase resistance R is determined experimentally with an RLC-meter. As for the cyclic inductance, the resistance is measured on the three phases to verify whether the system is well-balanced. The results for three frequencies (DC, 120 [Hz] and 1 [kHz]) are reported in Table 4.6. It can be remarked that the resistances of the three phases are close for each frequency. Furthermore, as expected, the resistance increases with the frequency due to the skin and proximity effects. Finally, the theoritical resistance is close to the DC measurement, thus validating the method of calculation.

Table 4.6: Resistance measurements [Ω].

R	**Phase 1**	**Phase 2**	**Phase 3**
DC	5.28	5.28	5.29
120 [Hz]	5.52	5.54	5.48
1 [kHz]	7.34	7.38	7.34

4.4 Model predictions

The eight parameters being identified, the model derived in the third chapter can be exploited to predict the axial dynamics as well as the quasi-static behaviour of the system constituted of the prototype and its test bench. Given that the parameters evolve with the frequency, the model predictions have to be determined at a frequency near to that of the targeted spin speed.

4.4.1 Root locus

As for the practical case, the root locus is derived by calculating the eigenvalues of the matrix $\mathbf{A}'$ in (3.62) for spin speeds ranging from 0 to 10^6 [rpm]. Considering first the parameters identified at 120 [Hz], Fig. 4.27 shows the root locus of the two relevant poles, the two other being again located in the left half plane, far from the imaginary axis. As expected, the system is stable up to the unstability spin speed ω_u. Given that there is

neither damping C nor detent stiffness K_d and that the first term of the expression (3.78) is negligible, this speed corresponds to the electrical pole R/L_c through the number of pole pairs, i.e. $\omega_u = R/pL_c = 8962$ [rpm].

As a reminder, the time evolution of the state-space variables is a linear combination of the four modes described by the eigenvalues and eigenvectors. Among these, two are almost imperciptible as they are really fast as a result of their eigenvalues. By contrast, the two relevant poles clearly impact the dynamics of the system. Hence, in the underdamped part of the curve, i.e. when the speed varies from $\omega_d = 81$ [rpm] to ω_u, the pulsation of the state-space variables, as the axial displacement z, evolves from zero to 72 [rad/s]. Besides, the time constant τ of the intrinsic damping, i.e. the decreasing exponential that is multiplied with the oscillatory part, ranges from 1.11 [s] to the infinity. This means that the larger the spin speed is, the slower the axial displacement converges and the higher is the pulsation. Considering that the rotor has a non-zero initial axial displacement, the convergence at 98% is reached after 4τ, yielding a minimal time equal to 4.44 [s].

Let us now consider the parameters identified at 1 [kHz]. Fig. 4.28 shows the root locus of the two relevant poles. The two characteristic speeds ω_d and ω_u are respectively equal to 110 and 21 860 [rpm]. As expected, the unstability speed increases with the electrical frequency as the resistance increases contrary to the cyclic inductance which diminishes. Futhermore, at 1 [kHz], the maximal pulsation is 100 [rad/s] while the smallest time constant is 1.45 [s], yielding a minimal convergence of about 5.8 [s]. Measurements of the electrical parameters at higher frequencies should allow to determine the accurate unstability spin speed, taking into account the variations of the parameters with the frequency.

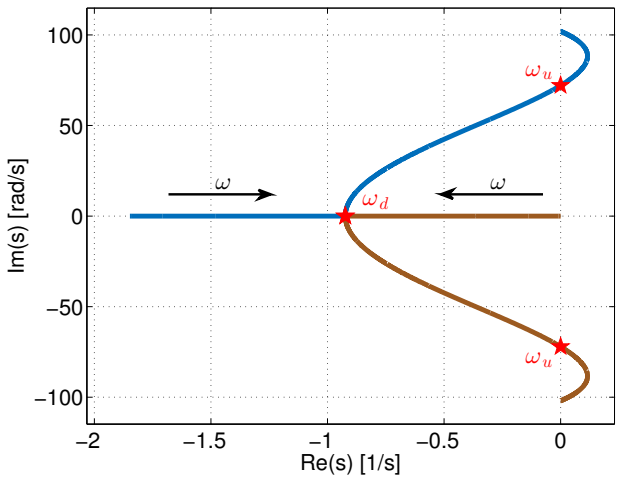

Fig. 4.27: Root locus of the two relevant poles at 120 [Hz].

4.4.2 Quasi-static analysis

The expression (3.75) yields the force exerted by the bearing for a spin speed corresponding, in this case, to the unstability speed. Therefore, the maximal axial stiffness K_f reachable by the prototype, while avoiding the unstability, can be calculated and yields 8.06 [N/mm] for the parameters at 120 [Hz] and 14.7 [N/mm] for the parameters at 1 [kHz]. Hence, although these stiffnesses are slight, the thrust bearing should be able to sustain the complete rotor

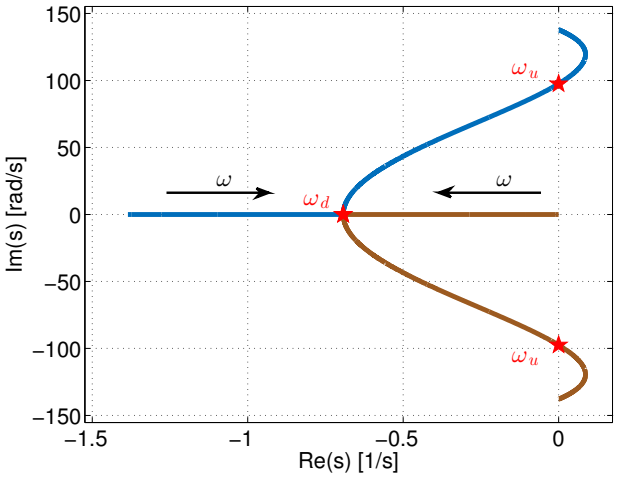

Fig. 4.28: Root locus of the two relevant poles at 1 [kHz].

(meaning that $\Lambda = 90°$) at an axial position near to 1 [mm] for a speed close to the real unstability spin speed. Fig. 4.29 shows the evolution of the axial stiffness K_f and the torque coefficient $K_t = |T|/z^2$ with the spin speed in quasi static conditions for the parameters at 120 [Hz]. The dotted line represents the unstability spin speed. Unfortunately, the induced stiffness appears to be clearly too small for more reasonable speeds. For instance, at 1000 and 2000 [rpm], it only attains 200 and 769 [mN/mm], which is slight, even for a stabilising effect. Fig. 4.29 shows the evolution of the axial stiffness K_f and the torque coefficient K_t with the spin speed in quasi static conditions for the parameters at 1 [kHz]. For spin speeds equal to 6500 and 10 000 [rpm], the axial stiffness reaches respectively 2.32 and 5.10 [N/mm], which should become sufficient to bring the rotor back in its nominal position when the axial load is close to zero.

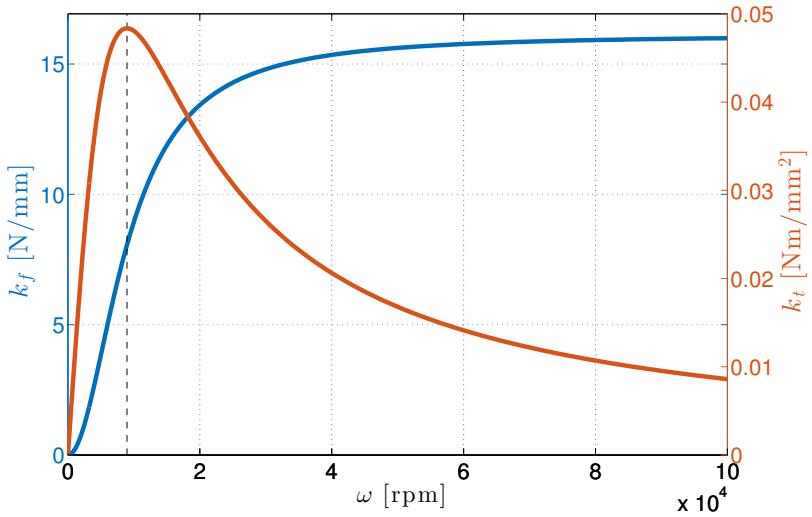

Fig. 4.29: Axial stiffness K_f and torque coefficient K_t with the spin speed in quasi-static conditions for the parameters measured at 120 [Hz]. The dotted line represents the unstability spin speed.

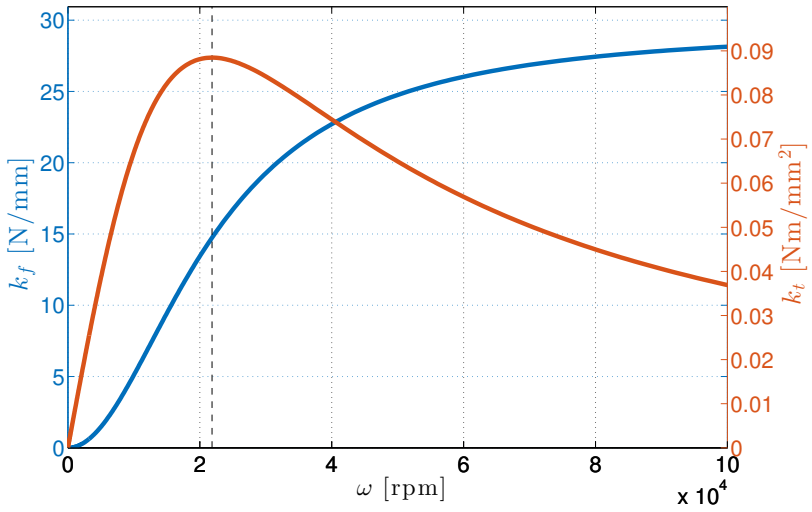

Fig. 4.30: Axial stiffness K_f and torque coefficient K_t with the spin speed in quasi-static conditions for the parameters measured at 1 [kHz]. The dotted line represents the unstability spin speed.

4.5 Experimental results

This section presents the results of the experimental measurements performed on the prototype. First, the different assumptions made to derive the model are verified. Following on from this, the voltages induced by the relative motion of the PMs arrangements with respect to the armature winding are compared to the theory. A dynamic analysis is later performed. Finally, several ways to improve the behaviour of the bearing are proposed.

4.5.1 Assumptions validation

In order to establish the state-space model of the EDTB, nine assumptions have been made in section 3.2. The two first ones are verified thanks to both air bearings ensuring the radial levitation. As regards the third, the absence of saturation has been confirmed in appendix C. Besides, hysteresis due to the PMs cannot appear as there is no relative motion between their magnetic field and the ferromagnetic parts. The fourth and fifth assumptions, about the inductance variations, are discussed hereinafter. The sixth hypothesis is not verified and has a large impact on the results, as shown in the model predictions in section 4.4. The seventh, concerning the eddy currents, is discussed further down. The validity of the eighth has been verified in section 4.3.1, e.g. in Fig. 4.26. The last one only depends on the drive system and not on the thrust bearing itself.

Inductance variations

According to the fourth assumption, the inductance variations due to rotor axial and radial displacements are negligible. The latter displacements are not allowed due to the air bearings. By contrast, as explained in section 3.2, the presence of ferromagnetic parts linked to the PMs can lead to inductance variations with the axial displacement. The armature winding of the prototype is constituted of three phases, themselves composed of two coils, namely the left and right ones (corresponding to the upper and lower in the model).

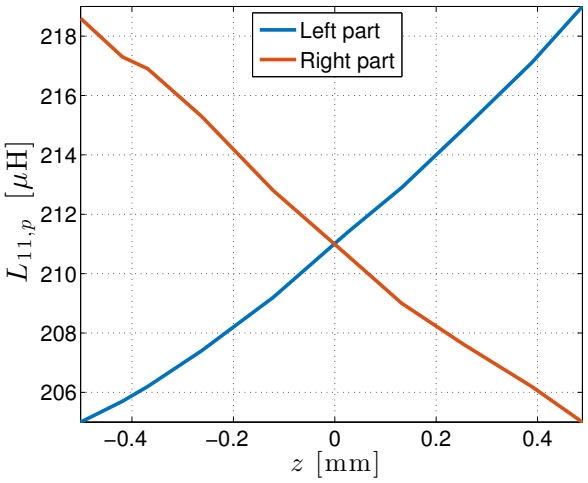

Fig. 4.31: Variation of the self inductance $L_{11,p}$ of both parts of one phase with the axial displacement z at 1 [kHz].

Fig. 4.31 shows the evolution of the self inductance $L_{11,p}$ of both coils, left and right, constituting the third phase with the axial displacement z at 1 [kHz]. It can be remarked that there is a small and nearly linear variation with the axial position of the rotor for both parts. Besides, these variations intersect when the displacement is zero and present the same slope with an opposed sign. They are due to the fact that the windings are closer or further of the ferromagnetic parts. Fig. 4.32 shows the position of the left (L) and right (R) coils (in green) with respect to the ferromagnetic parts (in grey) and the PMs (in white) for three axial displacements. In the first case, the right coil is closer to a back iron and thus presents a higher self inductance. In the second case, both inductances are identical as the rotor is exactly in the center of the system. In the last case, the left inductance is larger as the corresponding coil is closer to a back iron. By constrast, the sum of these two inductances, yielding the complete self inductance of the third phase as the mutual inductance is negligible, is constant with the rotor axial position and equal to 422 [μH], as reported in section 4.3.2. The fourth assumption is thus verified. As regards the fifth, the thrust bearing showing a rotational symmetry, there is no inductance variation with the angular position.

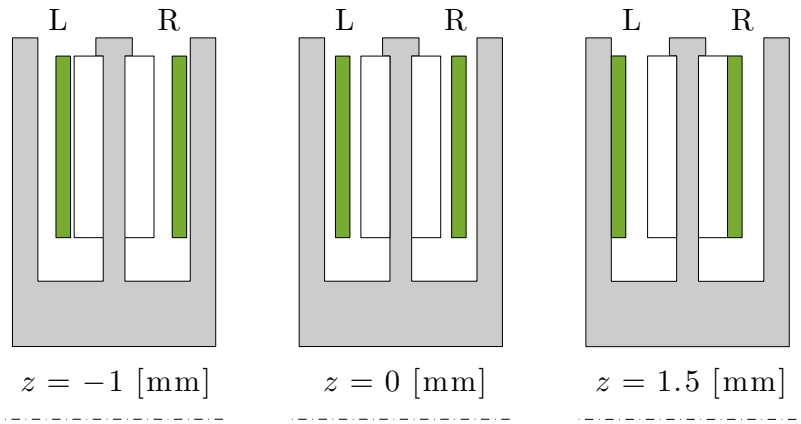

Fig. 4.32: Location of the windings (in green) with respect to the ferromagnetic parts (in grey) and the PMs (in white) for three axial displacements.

Eddy currents

As mentioned above, being drived by the compressed air turbine, the rotor can reach at least 4500 [rpm] when the armature winding is not present. By contrast, contrary to what was foreseen, it does not allow to exceed 1100 [rpm] when the armature winding is present but in open circuit, meaning that the thrust bearing should have no impact on the rotation. In the same way, the electrical and pneumatic motors enable to reach respectively at most 2000 and 6500 [rpm]. Therefore, there exists a unintended counteracting torque that can have two sources. On the one hand, an aerodynamic torque can arise given that the test bench is composed of six air gaps where large surfaces are in relative motion, as shown by the red lines in Fig. 4.33. On the other hand, an electrodynamic braking torque can appear due to Eddy currents inside the tracks, even when the armature winding is in open circuit.

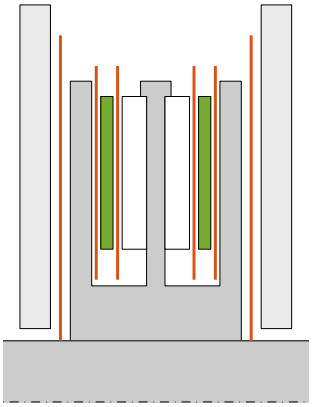

Fig. 4.33: Schematic representation of the EDTB and its test bench with the windings (in green), the ferromagnetic parts (in dark grey), the PMs (in white) and the lids (in light grey). The red lines show the surfaces in relative motion where an aerodynamic torque can appear.

In order to determine the relative importance of both of these phenomena, two tests have been performed. On the one hand, the evolution of one phase resistance is measured repeatedly after a certain time of operation. Indeed, the resistivity of the copper is linked to the temperature through a fairly linear relation, allowing to determine the resistance as a function of the temperature:

$$R(T) = R_0[1 + \alpha(T - T_0)], \tag{4.11}$$

where T_0 corresponds to a reference temperature, R_0 is the resistance at this temperature and α is a temperature coefficient, equal to 0.00393 $[1/K]$ for the copper at 20 [°C]. In this way, starting with the whole prototype at room temperature, i.e. $T_0 = 20$ [°C], the measurements of the resistance allow to determine the evolution of the temperature in the windings by inverting the relation (4.11). This experiment is performed with the phase windings in open circuit and then short-circuited. In both cases, the axial position is fixed to 0.4 [mm]. The prototype is drived by the pneumatic motor, allowing to reach a high spin speed, namely 6000 [rpm], such that the impact of the potential Eddy currents is non-negligigle. Indeed, the amplitude of the Eddy currents increasing with the frequency of the magnetic field that induces them, this torque should increase with the rotor spin speed and thus the Joule losses. Fig. 4.34 shows the evolution of the temperature in the

windings during these experiments. Both curves are really close, meaning that the effect in open circuit is rather important. The temperature attains up to 105 [°C] after 200 [s], favouring the hypothesis of the Eddy currents. This is all the more true knowing that the temperature of the lids does not follow such an increase.

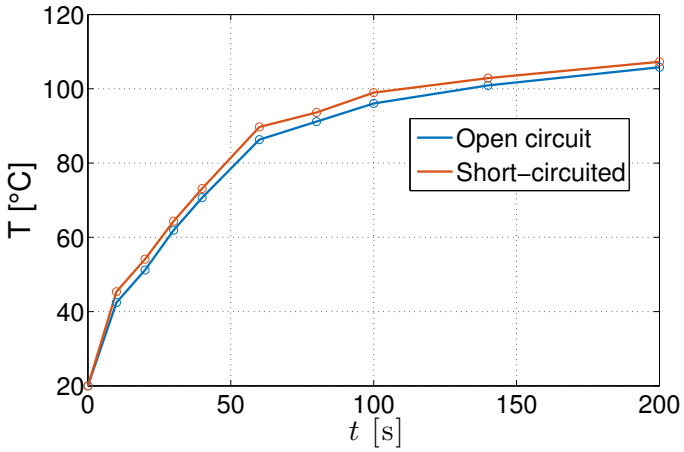

Fig. 4.34: Temperature evolution of the windings when the rotor spin speed is 6000 [rpm].

On the other hand, the maximal rotor spin speed has been measured in three specific cases. First, the armature winding is short-circuited, thus corresponding to the normal functioning of the bearing. Second, the armature winding is left in open circuit, meaning that the bearing should have no impact on the rotation. Finally, each part of the armature winding is replaced by a Plexiglass plate which presents exactly the same shape and dimensions. Hence, the aerodynamic efforts induced by the rotation of the rotor remain identical but there are no more Eddy currents induced in the statoric parts. During these tests, the rotor is again driven by the pneumatic motor. In both first cases, the maximal spin speeds are very close to 6500 [rpm]. By contrast, in the third case, the rotor spin speed has easily reached 8500 [rpm] and was still increasing. This second experiment allows to eliminate the assumption about the aerodynamic torque, and, coupled with the first experiment, to clearly highlight the source of the braking torque as being the Eddy currents induced inside the tracks.

Hence, the seventh assumption, stating that the Eddy currents are neglected, is clearly not verified, meaning that the model cannot be applied to study the dynamic and quasi-static behaviours of the prototype.

4.5.2 Voltages induced in the coils

Although the experimental results cannot be compared with the model predictions, the voltages induced in the different coils can be studied. As mentioned above, for lower speeds, the effect of the Eddy currents is smaller. The voltages induced by the relative motion of the PMs arrangements with respect to the armature winding in both coils constituting each phase lie at the basis of the functionning of the thrust bearing. Therefore, they are compared to the theory in order to validate the working principle of the tested topology.

Relative amplitude

Figs. 4.35a and 4.35b show the voltages induced in both left and right coils constituting the third phase at 1350 [rpm] for an axial displacement equal to -0.25 and 0.25 [mm] respectively. As expected, when the axial displacement is negative, the PMs arrangements are closer to the left coil than to the right coil, leading to a higher amplitude of the magnetic flux density and thus amplitude of the induced voltage. Conversely, when the axial displacement is positive, the flux linked by the right coil is larger and so is the induced voltage. Therefore, theoritically, there should exist a rotor position, namely the equilibrium or nominal position, in which both coils link exactly the same flux, yielding an identical amplitude of the induced voltage and thus a voltage induced in the complete phase equal to zero.

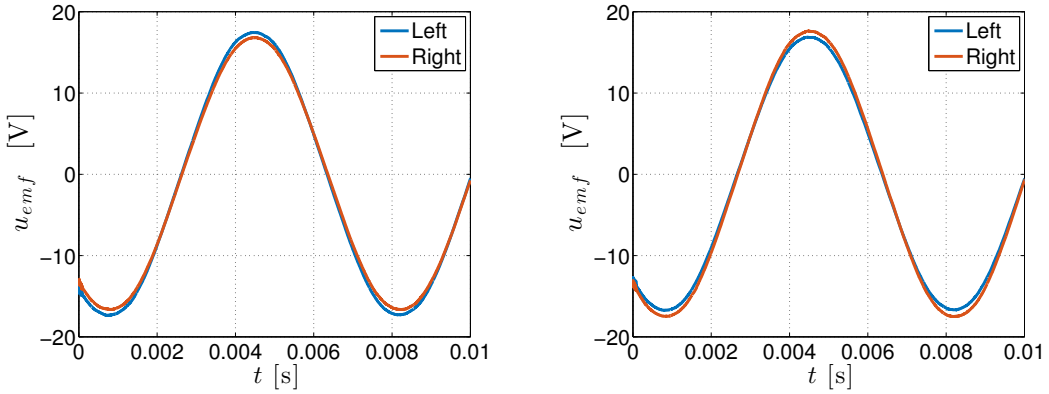

(a) $z = -0.25$ [mm]. (b) $z = 0.25$ [mm].

Fig. 4.35: Induced voltages in both left and right coils constituting the third phase for a spin speed $\omega = 1350$ [rpm].

Phase shift

Theoritically, the voltages induced in both left and right coils constituting each phase have to be exactly in phase, given that the mechanical angular shift $\Delta\theta_a$ between them is equal to zero and the PMs are in attractive mode. However, in practice, measurements show that a small phase shift between both induced voltages exists. For instance, in Figs. 4.35a and 4.35b, the phase shift between the voltages is about 0.9°. In addition, as illustrated in Fig. 4.36 where the phase shift is equal to 7.9°, this phase shift is not constant. More generally, it varies with the axial position and decreases when the spin speed increases.

This phase shift can have two sources. On the one hand, it can be due to a wrong relative positioning of both parts constituting the armature winding and/or both PMs arrangements, meaning that the angular shifts $\Delta\theta_a$ and $\Delta\theta_{PM}$ are not exactly equal to 0 and π/p respectively. Indeed, although a chock has been used to ensure a proper alignment between both PMs arrangements, a small angular shift is still possible. As regards the armature winding, the same phenomenon can appear as they are just screwed, leaving the opportunity for a small angular excursion. The impact of these shifts is intensified in electrical angle, due to the factor p. However, as these are mechanical angular shifts, they vary neither with the spin speed nor the axial position.

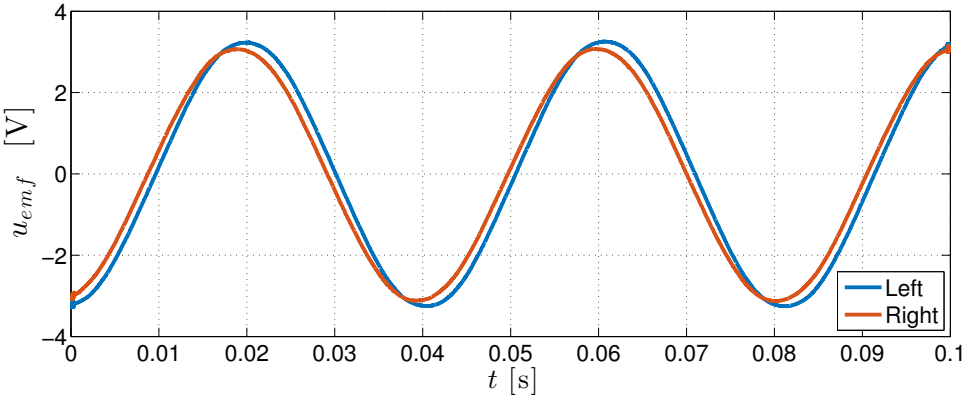

Fig. 4.36: Voltage induced both right and left coils constituting one phase at 243 [rpm] and $z = -0.1$ [mm]

On the other hand, this phase shift can be due to the Eddy currents that are locally induced in the tracks. These create are a varying magnetic field which is in turn linked by the winding. Assuming that the Eddy currents can be represented by a separate short-circuited winding, this latter is magnetically linked to the phase winding through a mutual inductance. Besides, the effect of these currents is higher as the spin speed increases and is different in each coil when they are not located at an identical distance from the PMs arrangements, i.e. in the nominal position. Finally, Eddy currents can also be induced in the back irons by the Eddy currents induced in the tracks and would represent a new separate short-circuited winding linked to the two others through mutual inductances. This could explain the variations in the phase shift with the spin speed and the axial position.

4.5.3 Voltages induced in the phases

The behaviour of the voltages induced in both coils constituting each phase being analysed, the resulting voltage induced in the latter can be studied. To this end, let us examine the impact of the small phase shift between the voltages in each coil. Defining respectively u_R and u_L as the voltages in the right and left coils, these are given, in phasor notation, by:

$$\begin{aligned} u_R &= U_R \angle 0 \\ u_L &= U_L \angle \chi, \end{aligned} \tag{4.12}$$

where u_R is taken as a reference as regards the phases, U_R and U_L are the amplitude of the corresponding voltages and χ is the phase shift between them. Hence, the resulting voltage u_T in the phase constituted of these coils connected in opposition is:

$$u_T = u_R - u_L. \tag{4.13}$$

Let us represent this situation in a phasor diagram. The blue, red and yellow curves are respectively u_R, u_L and u_T and $U_R = 1$. In the ideal case, χ being equal to zero, the amplitude of u_T is simply the difference between U_R and U_L in absolute value and the phase is either equal to zero or to 180°, depending whether U_R is larger or lower than U_L. This situation is represented in Fig. 4.37a where $U_L = 0.8U_R$.

By contrast, when the phase shift χ is non-zero, the amplitude of the resulting voltage increases. As regards the phase of u_T, it can reach up to ±90°, depending on the sign of χ. Fig. 4.37b shows a first situation in which U_L is still equal to $0.8U_R$ but χ is now equal

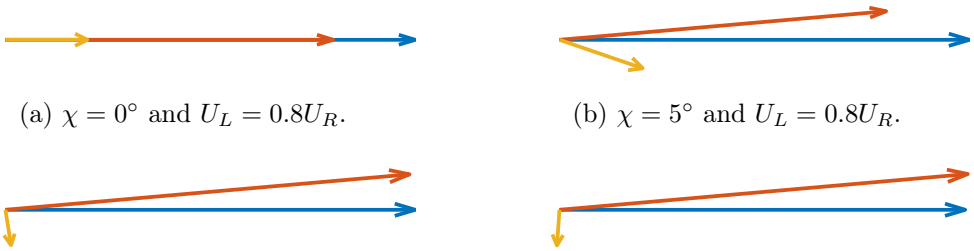

(a) $\chi = 0°$ and $U_L = 0.8U_R$.

(b) $\chi = 5°$ and $U_L = 0.8U_R$.

(c) $\chi = 5°$ and $U_L = 0.99U_R$.

(d) $\chi = 5°$ and $U_L = 1.01U_R$.

Fig. 4.37: Phasor diagrams of the voltage induced in the coils for different phase shifts and amplitude ratios. The blue, red and yellow curves are respectively u_R, u_L and u_T.

to 5°. The phase of u_T reaches $-19°$ and the amplitude is 0.215 (instead of 0.2 in the ideal case). In a second situation, shown in Fig. 4.37c, the phase shift χ is kept to 5° while the amplitude U_L become equal to $0.99U_R$. In this case, the phase of u_T is equal to -80° and its amplitude to 0.09 instead of 0.01. Fig. 4.37d shows a situation where U_L is larger than U_R, leading to an amplitude and a phase of u_T respectively equal to 0.09 and 94°.

Hence, from these phasor diagrams, it can be concluded that the closer the phase shift χ is to zero, the smaller the amplitude error is. Besides, when the difference between U_R and U_L decreases, the amplitude of u_T also decreases up to reach a non-zero limit value while its phase approaches $\pm 90°$. Unfortunately, the working principle of the thrust bearing topology of the prototype is based on the fact that the voltages induced in both left and right coils become closer as the rotor approaches its equilibrium position, up to being equal in this position. Due to the phase shift, the voltage induced in a complete phase cannot reach zero, leading to a current flowing in the conductors even in the nominal position, meaning that there are Joule losses in this position. The prototype thus does not respect the null-flux principle.

Amplitude in one phase

As mentioned in section 4.3.1, in the ideal case, the voltage induced in one phase winding in quasi-static conditions at constant spin speed is given by the expression (4.7). Hence, its amplitude is proportional to the axial displacement and to the spin speed. This expression remains valid until the rotor axial position becomes too close to the equilibrium. It is consistent with the measurements performed to identify the coefficient K_Φ, in Fig. 4.25. Indeed, it should not have escaped the attentive reader that the amplitude of the induced voltage deviates from the straight lines and decreases less and less (in absolute value) when the axial position gets closer to zero. This behaviour, which starts near to $z = \pm 0.2$ [mm], is due to the phase shift, as explained above.

Let us verify that the voltage in one phase follows the expression (4.7) when the axial position is not too close to the equilibrium. Fig. 4.38 shows the voltage induced in one phase winding for three different cases. Let us take the first one, corresponding to $z = 0.2$ [mm] and $\omega = 1000$ [rpm] as starting point. In the second case, the axial displacement is multiplied by two ($z = 0.4$ [mm]) leading to an amplitude of the induced voltage which is also doubled. The third case corresponds to $\omega = 2000$ [rpm] and $z = 0.2$ [mm]. As expected, the amplitude and the frequency of the induced voltage are also doubled.

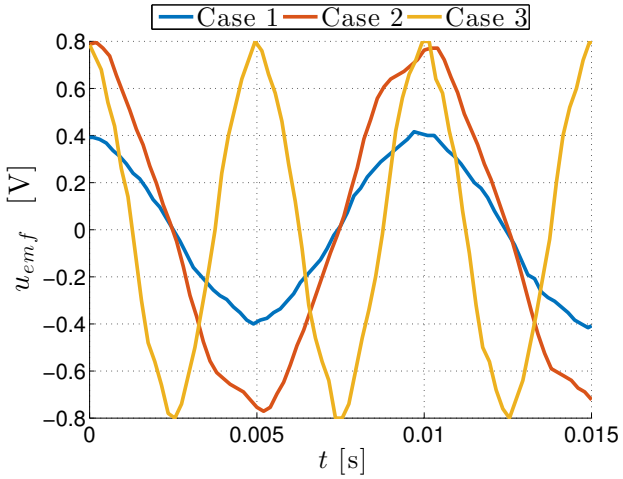

Fig. 4.38: Voltage induced in one phase winding. Case 1 corresponds to $z = 0.2$ [mm] and $\omega = 1000$ [rpm]. Case 2 corresponds to $z = 0.4$ [mm] and $\omega = 1000$ [rpm]. Case 3 corresponds to $z = 0.2$ [mm] and $\omega = 2000$ [rpm].

Phase shift

Theoritically, the voltage induced in one phase should be either in phase or in opposition with respect to that of both coils constituting this phase. However, as explained above, the phase shift between both coils leads to a phase shift between each of them and the complete phase. Figs. 4.39a to 4.39f show the voltage induced in the right coil and in the complete phase ($\times 10$ for clarity purposes) for several axial positions along the whole stroke and $\omega = 1000$ [rpm]. As expected, both measured voltages are not in phase and the phase shift between them evolves with the axial position, going from 20° to 157°. This behaviour corresponds to what has been predicted with the phasor analysis. Indeed, for positive axial displacements, the phase shift is equal to zero in the ideal case and increases up to reach 90° when the displacement decreases. Conversely, for negative axial displacements, the phase shift is equal to 180° in the ideal case and decreases up to reach 90° when the axial displacement increases. For a position close to the equilibrium, as shown in Fig. 4.39c, the amplitude of the voltage induced in the complete phase is still non-negligible and the phase shift is close to 90°, as stated above. Hence, compared with the ideal case, the current induced in the phases is shifted by 90°. This means that when the rotor is close to its nominal position, an inductive behaviour favours the braking torque and a resistive behaviour favours the axial force, representing a trend reversal with respect to the ideal case. Fig. 4.40 shows the evolution of the phase shift between the right coil and the complete phase for several axial displacements and spin speeds. The differences between the curves come from the variations in the phase shift between the left and right coils, as mentioned above.

Three-phased system

Fig. 4.41 shows the voltage induced in the three phases for an axial displacement $z = 0.2$ [mm] and a spin speed $\omega = 1290$ [rpm], which corresponds to an electrical period equal to 7.75 [ms]. As expected, there is an angular shift of $2\pi/3$ between the consecutive phases and they all have the same amplitude.

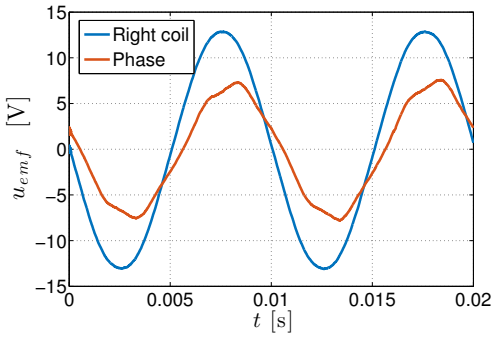

(a) $z = 0.42$ [mm].

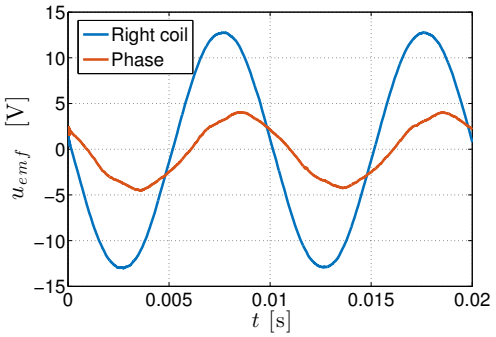

(b) $z = 0.25$ [mm].

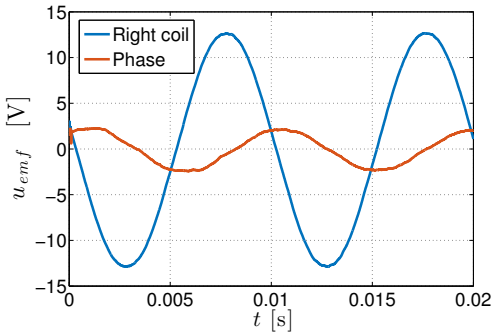

(c) $z = -0.01$ [mm].

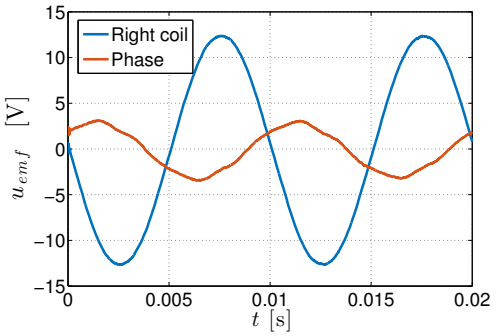

(d) $z = -0.1$ [mm].

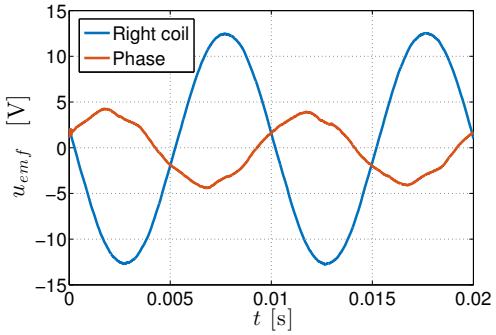

(e) $z = -0.2$ [mm].

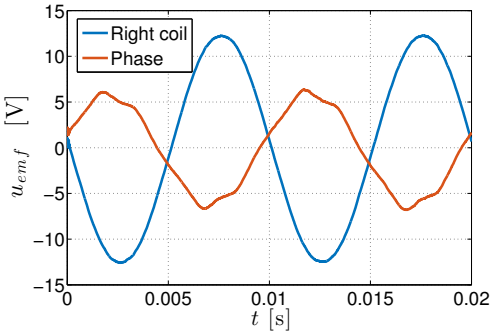

(f) $z = -0.3$ [mm].

Fig. 4.39: Voltage induced in the right coil and in the complete phase ($\times 10$) for several axial positions and $\omega = 1000$ [rpm].

4.5.4 Dynamic analysis

As stated in section 4.4.2, the axial stiffness of the prototype becomes non-negligible for a spin speed close to 5000 [rpm]. Unfortunately, at this speed, the prototype does not follow the model due to the large Eddy currents induced inside the tracks of the windings. However, although these currents create a large braking torque, they also generate an axial restoring force, following an identical working principle to that of the second topology explained in section 1.2.1.

Fig. 4.42a shows the time evolution of the axial displacement when the axial load F_e is zero ($\Lambda = 0$), the windings are in open circuit and the rotor starts from $z = 0.45$ [mm] at 6000 [rpm]. As expected, after about 20 [s], the rotor reaches an equilibrium position $z_{0,t}$, different from that of the bearing, i.e. $z = 0$. Let us consider that the force due to the

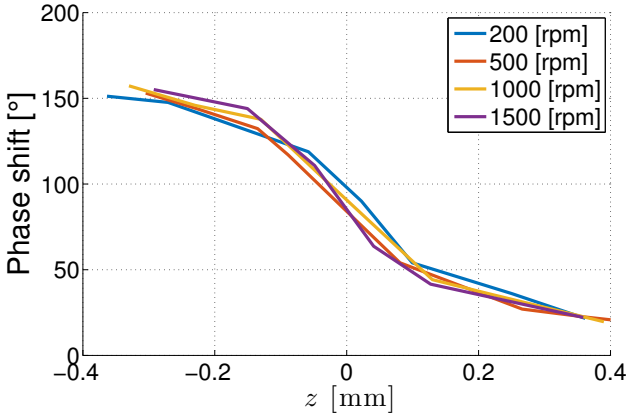

Fig. 4.40: Phase shift between the right coil and in the complete phase for several axial displacements and spin speeds.

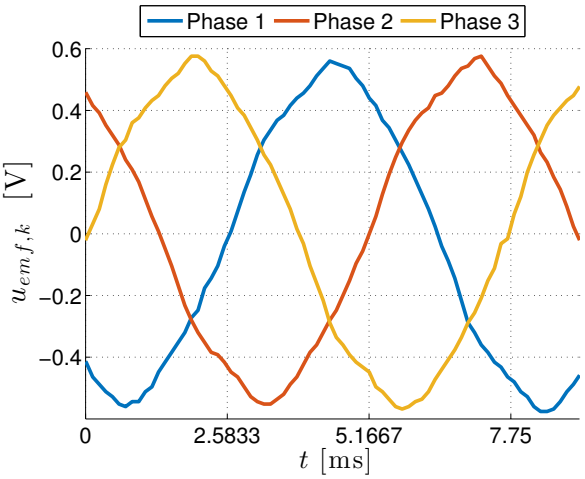

Fig. 4.41: Induced voltages in the three phases for an axial displacement $z = 0.2$ [mm] and a spin speed $\omega = 1290$ [rpm].

Eddy currents can be represented by a spring equivalent force in quasi-static. Therefore, as detailed in appendix K, assuming that the mechanical characteristics of the bellows coupling, namely its equilibrium point $z_{0,s}$ and its stiffness K_s, are known, the stiffness K_c induced by the Eddy currents can be determined experimentally as:

$$K_c(\omega) = K_s \left(\frac{z_{0,s}}{z_{0,t}(\omega)} - 1 \right) \tag{4.14}$$

Fig. 4.42b shows the time evolution of the axial displacement for identical conditions except that the windings are short-circuited. The time required to converge is roughly equivalent. By contrast, the amplitude of the oscillations is smaller and the equilibrium position is closer to that of the thrust bearing. The latter can be explained by the fact that, in addition to the stiffness K_c induced by the Eddy currents, there is also the stiffness K_f induced by the proper functioning of the EDTB. Therefore, considering that $K_c(\omega)$ is known, the stiffness $K_f(\omega)$ can be determined as:

$$K_f(\omega) = K_s \left(\frac{z_{0,s}}{z_{0,t}(\omega)} - 1 \right) - K_c(\omega) \tag{4.15}$$

Hence, as shown in appendix K, benefiting also from the loading system, it is possible to determine experimentally the evolution of K_f with the spin speed.

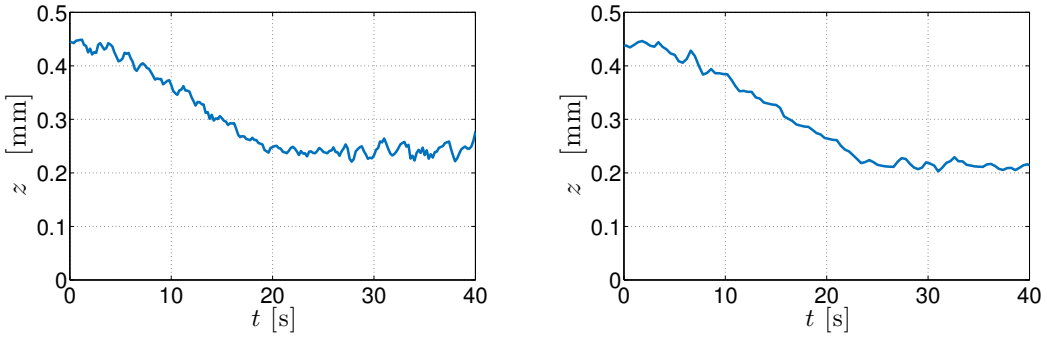

(a) Windings in open circuit.

(b) Windings short-circuited.

Fig. 4.42: Time evolution of the axial displacement z when the rotor starts from $z = 0.45$ [mm] and $\omega = 6000$ [rpm].

4.5.5 Further improvements

As things stand, the prototype of the thrust bearing is not really functional and its performances do not correspond to the model predictions. The previous subsections have allowed to identify four critical issues. Therefore, this subsection aims at providing various ways to tackle these issues and thus to improve the behaviour of the prototype.

Eddy currents

The major problem preventing the proper functioning of the prototype resides in the local appearance of unwanted Eddy currents in the tracks, mainly due to the too wide section of the second segment of the PCB tracks. This phenomenon can be avoided through several means.

As regards the PCB winding, considering that the shape of the tracks remains identical, the second segments can be stripped along the radial direction. As a result, the layer fill factor will diminish while the resistance will increase. The radius R_{ee} could also be reduced in order to decrease the largest width of the tracks. Besides, as mentioned in section 4.1.3, an optimisation algorithm can be used to determine a finer shape, which would allow to have a smaller maximal width for the tracks while keeping a large fill factor.

Otherwise, the PCB winding can be replaced by a wire-wound winding, as it has been planed initially. A non-overlapping concentrated winding with fractional pitch is investigated in appendix I. Obviously, the diameter of the wire has to be chosen in an intelligent way in order to avoid unwanted Eddy currents. To this end, the more classical wires can also be replaced by Litz wires. Indeed, the latter are constituted of several very thin wire strands that are insulated independently and then woven.

Phase shift

The second issue encountered with the prototype concerns the phase shift that exists between the induced voltages in both left and right coils constituting each phase, preventing

to respect the null-flux principle. As mentioned in section 4.5.2, it has two sources: the unwanted Eddy currents and the mechanical angular shifts between both PMs arrangements and/or both parts of the armature winding. Several tracks have already been given hereinabove to tackle the former. Regarding the latter, the mechanical angular shifts shall be minimised and even cancelled in the ideal case. To this end, the number of pole pairs can be decreased so as to reduce the impact of a mechanical shift on the electrical angles. Moreover, the mechanical conception of the prototype and its test bench deserve a particular attention. The alignment of the PMs arrangements can be ensured through several means. For instance, small holes can be drilled in the yoke to serve as a reference position. Otherwise, a U-shaped chock, as used for the prototype, can be fixed to the yoke until both last PMs, one on each side, are placed. It is also possible to add a non-magnetic part on each side of the yoke and in which the PMs are burried.

The angular shift between both parts of the armature winding can be avoided by minimising the diameter of the screw clearances in the protective shield or replacing them by tap drills. It is also possible to substitute the screw clearances in the PCBs by elongated holes. It would allow to fix each PCB in a position such that the voltage induced in both parts are in phase. Besides, this solution enables to remove the effect of an angular shift between the PMs arrangements.

EDTB performances

Even assuming that both first issues have been tackled, the theoritical stiffness developed by the thrust bearing is rather small, as mentioned in section 4.4.2. A simple way to improve the stiffness whilst increasing the unstability spin speed is to remove the back irons. The coefficient K_Φ can be determined through finite element methods, as explained in section 4.3.1, yielding 5.35 [Wb/m], i.e. an improvement of 125%. Obviously, the phase resistance does not change. By contrast, the cyclic inductance diminishes to reach 415 [μH] and does not vary anymore between 120 [Hz] and 1 [kHz] as there are no more induced currents in the back irons. With these parameters and the resistance at 1 [kHz], the model predicts an axial stiffness equal to 51.67 [N/mm] at the unstability speed $\omega_u = 29490$ [rpm], namely almost 3.5 times more than with the back irons. This allows to slightly improve the stiffness for the speeds that are reachable with the test bench. For instance, the stiffness is equal to 4.48 [N/mm], namely an increase of 118%, at 6000 [rpm]. Obviously, without the back irons, all the ferromagnetic parts located at the stator have to be removed to maintain a zero detent stiffness K_d. Besides, the lids being in aluminium, they have to be manufactured in a non-conductive material, so as to avoid Eddy currents.

Although it is not required to ensure the stability in the usual spin speeds range, additional damping can be provided to improve the dynamic behaviour of the system. As mentioned in section 3.7.4, this damping allows to move the poles to the left by an amount proportional to C. Considering the parameters at 1 [kHz], the prototype becomes unconditionally stable for a damping factor equal to 0.09 [Ns/m]. This is all the more true given that this value decreases when the frequency used to identify the parameters increases. Hence, the maximal axial stiffness that is reachable is increased as there is no more unstability speed. Besides, the damping being non-zero, it also allows to decrease the time required to converge. This damping can be implemented in the prototype through several means. A conductive disc, which is attached to the stator (rotor), can be placed between two ring-shaped permanent magnets polarised axially, which are fixed to the rotor (stator). When the rotor is in quasi-static conditions, i.e. $\dot{z} = 0$, the conductive disc experiences a

constant magnetic flux density. By contrast, when the rotor moves axially, the flux linked varies over time and an electrodynamic damping appears. The same working principle can be applied by fixing a ring-shaped permanent magnet polarised radially to the stator, a ferromagnetic part of the rotor being located inside this magnet. Obviously, these means have an impact on the other degrees of freedom.

Finally, the performances of the bearing can be significantly improved through an optimisation process on the overall system.

Drive system

Three drive systems have been investigated in this experimental validation. Due to the unwanted Eddy currents, and the braking torque that ensues from these, the rotor was not able to reach high spin speeds. However, as mentioned in section 4.4.2, the higher the speed, the larger the axial recentering force. Assuming that there is no Eddy currents, the compressed air turbine seems to be the most appropriate drive system as it has no impact on the axial displacement as soon as the spin speed has reached the hoped value. Nevertheless, it is still difficult to evaluate the maximal spin speed that can be attained through this drive without simulations. As regards both other drive systems, they suffer from the major drawback that they have to be coupled to the rotor. Mechanical couplings, such as the flexible bellows one used, have an impact on the axial displacement through their stiffness. A magnetic coupling could replace the mechanical one and would allow to be removed when the wanted spin speed is reached and thus to reduce its impact on the axial dynamics.

Otherwise, recent researches have revealed that radial heteropolar electrodynamic bearings can gather, within the same structure, both guiding and driving functions [29] [30]. Hence, by connecting in an intelligent way a power supply to the windings of the bearing, the latter becomes able to exert a drive torque to the rotor. Compared with existing self-supporting electrical machines, they offer the major advantage that the bearing function is ensured through a passive mean, allowing to increase the reliability and the compacity of the system [31]. This technological advance could be transposed to the electrodynamic thrust bearings. Obviously, the topology proposed in [17] is not adapted as there is no flux linked by the windings in the nominal position, preventing the appearance of a driving torque. By contrast, the set of new topologies presented in the second chapter respect the null-flux principle but both parts constituting the armature winding link a non-zero flux, even in the nominal position. Therefore, they should potentially allow to drive the rotor.

PMs fixation

Particular attention has to be devoted to the fixation of the PMs. For the prototype, the permanent magnets are only set down on the ferromagnetic yoke against an edge of 1 [mm] height, as shown in Fig. 4.2. During the experiment in which the armature winding has been replaced by Plexiglass plates, the centrifugal efforts have exceeded the friction efforts exerted on the permanent magnets for a spin speed close to 8500 [rpm] and the latter have come away of the yoke and crushed against the protective shield. To avoid this issue, the height of the edge of the yoke could be increased. In a safer way, the PMs can be burried in non-magnetic parts which would be placed on both side of the yoke. It might also be possible to replace both PMs arrangements by only one non-magnetic disc in which the PMs are burried.

CONCLUSION

The aim of this master's thesis was first to design a new thrust bearing topology, then to derive a global dynamic model and finally to develop a prototype and its test bench so as to validate both the working principle of the new topology and the model.

In the first chapter, a review of the current state of the art of the thrust bearing topologies has been depicted. It has allowed to show that most of them respect the null-flux principle, thus enabling to reduce the Joule losses in the bearing. On the basis of the state of the art, the second chapter has exposed a set of new topologies that had not been explored yet as well as the conditions that they have to satisfy to respect the null-flux principle. From this, degenerated topologies have been described, leading, for instance, to the topology proposed in [23].

The third chapter has been dedicated to the derivation of a global dynamic model. Considering small axial and radial displacements, the general form of the PM flux linked by each winding phase has been obtained and then validated through a practical case. Based on the PM flux linkage, a state-space representation describing the axial dynamics of a thrust bearing has been derived. Compared to existing models, it requires neither assumptions on the rotor axial kinematics nor solving for the currents. It can be applied to study a wider range of bearings, including those with an arbitrary number of phases and ferromagnetic yokes. As a result, electrodynamic thrust bearings with potentially increased performance are now within the scope of a linear model.

The model depends on eight parameters whose identification is detailed in the third chapter. This reduced set of parameters and equations fully describes the dynamics as well as the quasi-static behaviour of EDTBs and therefore enables to analyse their performances, including their stiffness and stability properties. Besides, being linear, the stability analyses are straightforward. Various bearings can thus be objectively compared and it becomes easier to determine the most suitable solution for an application. In particular, this model could be exploited in a process of optimal design of an electrodynamic thrust bearing. The originality of the designing and modelling work has actively encouraged writing an article published in the journal *Transactions on Magnetics* of the IEEE.

The fourth chapter has been devoted to the experimental validation through the prototyping of a new topology of EDTB. First, the topology and especially the PCB winding have been introduced. Following on from this, the test bench has been described. Then, the model parameters have been identified through experimental measurements on the one hand and through finite element methods or analytical formula on the other hand. The results were compared, allowing to validate the simulation and analytical formula. Hence, they could be used in an optimisation process. The model has then be exploited to predict the dynamic and quasi-static behaviours of the prototype. Unfortunately, the axial stiffness induced by the bearing is rather small and this is all the more true in the range of spin speeds that are reachable through the test bench.

Thereafter, the chapter has presented the experimental measurements performed on the prototype and has pointed out two major issues. First, two experiments have allowed to highlight the presence of unwanted Eddy currents inside the tracks of the armature winding. These create a large braking torque, inducing unintended Joule losses and preventing the bearing from operating properly. Second, despite these currents, the voltages induced in both coils constituting each phase have been analysed, allowing to validate the working principle of the topology. However, a phase shift due to the unwanted Eddy currents and to a mechanical angular shift between the parts constituting both subassemblies of the bearing has been underlined. It results in an amplitude and a phase errors in the voltage induced in the complete phases when the rotor is close to its nominal position. In this particular position, the amplitude is non-zero, leading to the failure to respect the null-flux principle and thus to Joule losses. By contrast, when the rotor is outside the region close to the nominal position, the voltage induced in the phases corresponds to the theory, allowing to validate the topology and the expression of the flux yielded by the model.

As a result, all the objectives of this master's thesis could not have been achieved. However, the critical issues have been highlighted and several ways to address them as well as to improve the test bench and the prototype performances are provided. They could therefore constitute the starting point for the continuation of the work undertaken, allowing to develop a functional prototype and then to validate the dynamic model. Subsequently, the model that has been derived as a part of this master's thesis only takes into account the axial degree of freedom. Hence, the four other degrees of freedom should be included in the model in order to describe the complete dynamics of EDTBs. This complete model could be exploited, for instance, to determine whether adding a magnetic circuit to the armature winding can have a stabilising effect as regards the radial and tilt degrees of freedom or in a process of optimal design. A particular attention could also be focused to the thermal effects induced by the heating of the coils due to Joule losses and their impact on the functioning of the bearing.

A further step towards self-supporting electrical machines in which the guiding is ensured through passive means could be passed by gathering, within the same windings, both guiding and driving functions. This unexpected original field of investigation has been opened through the set of new bearing topologies developed in the second chapter.

Finally, these prospects should allow to reach the ultimate goal, namely to design, model and implement a fully passive magnetic suspension including an electrodynamic bearing, thus benefiting from all the advantages that magnetic bearings offer.

BIBLIOGRAPHY

[1] G. Schweitzer and E. H. Maslen, *Magnetic bearings: theory, design, and application to rotating machinery*. New York, NY, USA: Springer-Verlag, 2009.

[2] R. Moser, J. Sandtner, and H. Bleuler, "Optimization of repulsive passive magnetic bearings," *IEEE Trans. Magn.*, vol.42, no.8, pp.2038-2042, Aug. 2006.

[3] J.-P. Yonnet, "Passive magnetic bearings with permanent magnets," *IEEE Trans. Magn.*, vol.14, no.5, pp.803-805, Sep 1978.

[4] K. D. Bachovchin, J. F. Hoburg, and R. F. Post, "Magnetic fields and forces in permanent magnet levitated bearings," *IEEE Trans. Magn.*, vol.48, no.7, pp.2112-2120, Jul. 2012.

[5] S. Earnshaw, "On the nature of the molecular forces which regulate the constitution of the luminiferous ether," *Trans. Camb. Phil. Soc.*, vol.7, pp.97-112, 1842.

[6] R. F. Post and D. D. Ryutov, "Ambient-temperature passive magnetic bearings: theory and design equations," *Proc. 6th Int. Symp. Magn. Bearings*, Cambridge, Massachusetts, USA, Aug. 5-7, 1998.

[7] T. A. Lembke, *Design and analysis of a novel low loss homopolar electrodynamic bearing*, Ph.D. dissertation, Royal Inst. Tech., Sweden, 2005.

[8] C. Murakami and I. Satoh, "Experiments of a very simple radial-passive magnetic bearing based on eddy currents," *Proc. 7th Int. Symp. Magn. Bearings*, ETH, Zurich, Switzerland, Aug. 23-25, 2000.

[9] A. Filatov, *Null-E Magnetic Bearings*, Ph.D. dissertation, University of Virginia, Blacksburg, VA, 2002.

[10] V. Kluyskens and B. Dehez, "Dynamical electromechanical model for magnetic bearings subject to eddy currents," *IEEE Trans. Magn.*, vol. 49(4), pp. 1444-1452, 2013.

[11] N. Amati, X. D. Lepine, and A. Tonoli, "Modeling of electrodynamic bearings," *J. Vib. Acoust.*, vol. 130(6), 2008.

[12] J. G. Detoni, F. Impinna, A. Tonoli, and N. Amati, "Unified modelling of passive homopolar and heteropolar electrodynamic bearings," *J. Sound and Vibrations*, vol. 331(19), pp. 4219-4232, 2012.

[13] C. Dumont, V. Kluyskens, and B. Dehez, "Linear state-space representation of heteropolar electrodynamic bearings with radial magnetic field," *IEEE Trans. Magn.*, vol. 52, no. 1, 2016.

[14] A. Filatov, E. Maslen, "Passive magnetic bearing for flywheel energy storage systems," *IEEE Trans. Magn.*, vol. 37 (6), pp. 3913-3924, 2001.

[15] F. Impinna, J. D. Detoni, N. Amati, and A. Tonoli, "Passive magnetic levitation of rotors on axial electrodynamic bearings," *IEEE Trans. Magn.*, vol.49, no.1, pp.599-608, Jan. 2013.

[16] J. Sandtner and H. Bleuler, "Electrodynamic passive magnetic bearing with planar halbach arrays," *Proc. 9th Int. Symp. Magn. Bearings*, Lexington, Kentucky, USA, Aug. 2004.

[17] R. F. Post, "Passive magnetic bearings for vehicular applications," *LLNL Technical Report UCRL-ID-123451*, 1996.

[18] J. Powell, D. Ganby, "Electromagnetic inductive suspension and stabilization system for a ground vehicle," US patent 3470828 A, Nov. 21, 1967.

[19] J. G. Detoni, "Progress on electrodynamic passive magnetic bearings for rotor levitation," *Proc. Inst. Mech. Eng., Part C: J. Mech Eng. Sci.*, vol. 228, pp. 1829-1844, 2014.

[20] G. Sacerdoti, A. Catitti, and L. L. Soglia, "Self-centering rotary magnetic suspension device," Italian patent 49943/71, Apr. 24, 1971.

[21] H. K. Asper, "Passive dynamically stabilizing magnetic bearing and drive unit," World patent 2003/098064, Nov. 27, 2003.

[22] J. Sandtner and H. Bleuler, "Compact Passive Electrodynamic Thrust Bearing," *Proc. 11th Int. Symp. Magn. Bearings*, Nara, Japan, Aug. 2008.

[23] K. D. Bachovchin, J. F. Hoburg, and R. F. Post, "Stable levitation of a passive magnetic bearing," *IEEE Trans. Magn.*, vol.49, no.1, pp.609-617, Jan. 2013.

[24] D. C. White and H. H. Woodson, *Electromechanical energy conversion.* Wiley, New York, 1959.

[25] J. Henry-Baudot, "Rotating electric machines with printed circuit windings", US Patent, 1964, US3144574 A.

[26] D. M. Gambetta, "New Design Methodologies for Printed Circuit Axial Field Brushless DC Motors", PhD dissertation, Dec. 2009.

[27] B. Dehez, F. Baudart, M. Markovic and Y. Perriard, "Theoretical and Experimental Investigation of Flex-PCB Air-Gap Windings in Slotless BLDC Machines," *IEEE Trans. on Industry Applications*, vol. 50, no. 5, pp. 3153-3160, Sept.-Oct. 2014.

[28] Eurocircuits, "PCB design guidelines", `http://www.eurocircuits.com/PCB-design-guidelines`, last access: 15/03/2016.

[29] C. Dumont, A. Gislon, V. Kluyskens, Ch. Espanet, B. Dehez, "Evaluation of the electrodynamic forces in a high-speed permanent magnet machine with rotor eccentricity", submitted to *15th Int. Symp. Magn. Bear.*, 2016.

[30] C. Dumont, V. Kluyskens, B. Dehez, "Electric Machine having a Radial Electrodynamic Bearing", EU Patent, 2015, EP15177331.

[31] A. Chiba, T. Fukao, O. Ichikawa, M. Oshima, M. Takemoto, D. G. Dorrell, *Magnetic bearings and bearingless drives*, Elsevier, 2005.